ABSTRACT

Title of Dissertation: DEVELOPMENT AND APPLICATIONS OF MULTIFREQUENCY IMAGING AND SPECTROSCOPY METHODS IN DYNAMIC ATOMIC FORCE MICROSCOPY

Gaurav Chawla,
Doctor of Philosophy, 2011

Dissertation directed by: Assistant Professor Santiago D. Solares,
Department of Mechanical Engineering

Force spectroscopy and surface dissipation mapping are two of the most important applications of dynamic atomic force microscopy (AFM), in addition to topographical imaging. These measurements are commonly performed using the conventional amplitude-modulation and frequency-modulation dynamic imaging modes. However, the acquisition of the tip-sample interaction force curves using these methods can generally be performed only at selected horizontal positions on the sample, which means that a 3-dimensional representation of the tip-sample forces requires fine-grid scanning of a *volume* above the surface, making the process lengthy and prone to instrument drift. This dissertation contains the development of two novel atomic force spectroscopy methods that could enable acquisition of 3-dimensional tip-sample force representations through a single 2-dimensional scan of the surface. The force curve reconstruction approach in the first method is based on

3-pass scanning of the surface using the recently proposed single-frequency imaging mode called frequency and force modulation AFM. A second, more versatile method based on bimodal AFM operation is introduced, wherein the fundamental eigenmode of the cantilever is excited to perform the topographical scan and a simultaneously excited higher eigenmode is used to perform force spectroscopy. The dissertation further presents the development of a trimodal AFM characterization method for ambient air operation, wherein three eigenmodes of the cantilever are simultaneously excited with the objective of rapidly and quantitatively mapping the variations in conservative and dissipative surface properties. The new methods have been evaluated within numerical simulations using a multiscale simulation methodology, and experimental implementation has been accomplished for two multifrequency variants that can provide 2-dimensional surface property contrast.

DEVELOPMENT AND APPLICATIONS OF MULTIFREQUENCY IMAGING AND SPECTROSCOPY METHODS IN DYNAMIC ATOMIC FORCE MICROSCOPY

by

Gaurav Chawla

Dissertation submitted to the Faculty of the Graduate School of the
University of Maryland, College Park in partial fulfillment
of the requirements for the degree of
Doctor of Philosophy
2011

Advisory Committee:
Assistant Professor Santiago Solares, Chair/Advisor
Professor Balakumar Balachandran
Professor Amr Baz
Professor Abhijit Dasgupta
Associate Professor Benjamin Shapiro

ACKNOWLEDGMENTS

First and foremost, I would like to thank my parents and sister for their constant support and inspiration. Their love and affection has been a source of energy through every step of my life. I thank God for His blessings and giving me a wonderful family.

I thank the rest of our family, who have continuously contributed in various ways to all the endeavors and happiness in life.

Professor Santiago Solares, my advisor, has been a constant source of inspiration during my stay in graduate school. Thanks is an understatement for so many opportunities he has provided me with, for his patient mentoring, for the life lessons I have learned from him and more importantly, for his friendship and trust.

I thank Professor Balakumar Balachandran for his guidance in the early stages of graduate school, and for providing motivation and research inputs throughout. I earnestly thank my committee members, Professor Amr Baz, Professor Abhijit Dasgupta, Professor Benjamin Shapiro and Professor Helim Aranda-Espinoza for their valuable time and inputs. Thanks to the faculty members who shared their knowledge in various courses that helped in my research.

I thank all my past and present group members – Adam, Alan, Dave, Hussein, Jeff, Josh and Lynn for creating a motivating work environment, for their constant

inputs on research and above all, for their friendship. I also extend gratitude to all of my teachers and mentors at previous institutions for their contributions to my life.

I thank Aftab, Arvind, Chaty, Danielle, Debo, Michelle, Rishi, Ritaja, Rupal, Sauleh and Supratik, whose friendship and presence in life during graduate school provided me with a familiar environment away from home and helped me grow personally and professionally. Special thanks to old friends, Jitu, Ritwik and Sourabh for their support at every step. I also thank all the other friends I have made over the years for the important role they have played in my life in so many ways.

This work was supported by the U.S. National Science Foundation [awards CMMI-0800471 and CMMI-0854735], by a Nanobiotechnology seed grant from the State of Maryland's Department of Business Economics and by a start-up grant from the Minta Martin Foundation at the University of Maryland.

Last but not least, I thank all the members of the Mechanical Engineering department and the University of Maryland who create a wonderful environment to be a part of. There is not enough space to express my appreciation for so many persons here that I have enjoyed the company and friendship of in these years.

Table of contents

Index of figures

1. Introduction

1.1 Background

In the late 1980s, the atomic force microscope (AFM) invented by Binnig *et al.* [1] experienced a significant transformation when a vibrating probe was used to explore the surface topography. Since then, the dynamic AFM methods have been emerging as powerful and versatile techniques for atomic and nanometer-scale characterization and manipulation of a wide variety of surfaces. Broadly, all of the dynamic AFM techniques can be categorized as either intermittent-contact mode or non-contact mode depending on the type of operation. The most frequently used dynamic modes of operation are intermittent-contact amplitude modulation (AM) and non-contact frequency modulation (FM) [2]. Also, there is a commonly used static

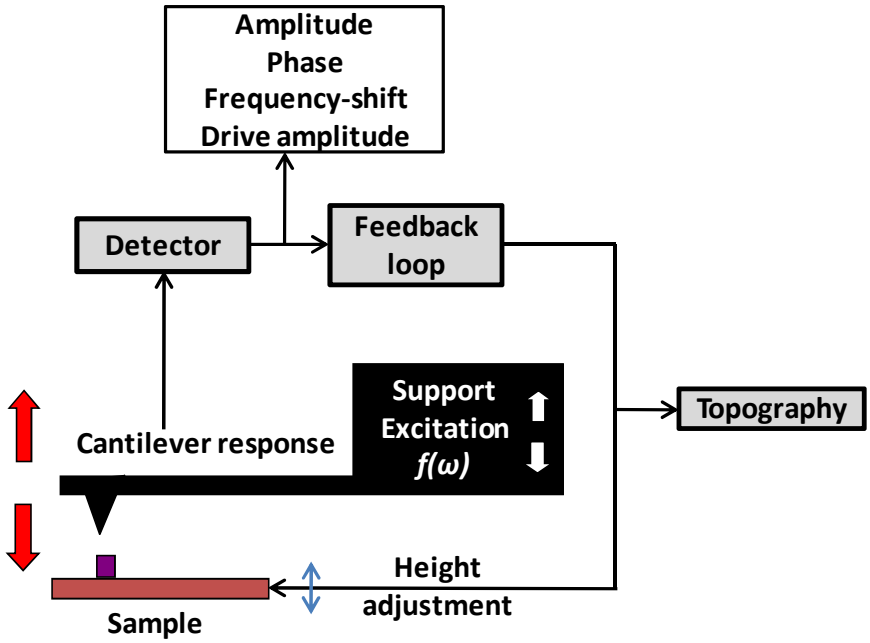

Figure 1-1 *General principle of AFM operation in dynamic mode. The excitation f(ω) can be a function of one or multiple frequencies.*

mode of operation known as the contact-mode (CM), in which the tip is in contact with the sample throughout the scan. Due to the oscillation of the cantilever in dynamic modes, the time of contact between the tip and the sample decreases, and consequently, operation in these modes causes less sample damage, allowing imaging of soft samples. FM-AFM attracted vast attention by demonstrating the capability to achieve atomic-resolution in non-contact mode under ultra-high vacuum [3]. The most recent developments in dynamic AFM have been in the multifrequency operation, where multiple cantilever eigenmodes are simultaneously excited with an objective to achieve extra output channels for surface characterization [4]. Figure 1-1 shows a general schematic of any dynamic AFM mode.

Down at the scale of the size of an AFM probe, different intermolecular, surface and macroscopic effects give rise to atomic-scale interactions with distinctive distance dependencies (Figure 1-2). In the absence of external fields and under ideal surface conditions, the dominant forces are long-range van der Waals attractive interactions and short-range repulsive interactions (explained by Pauli's exclusion

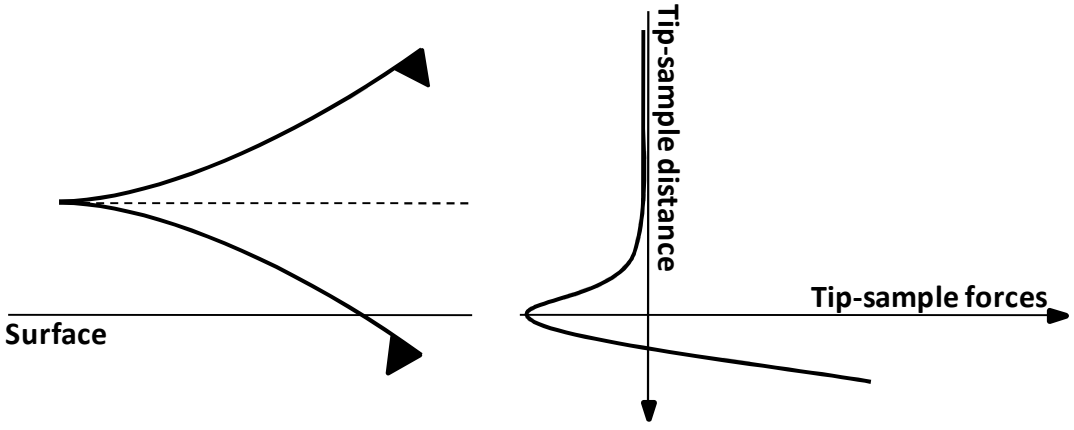

Figure 1-2 *Dependence of tip-sample interaction forces on the distance between the tip and the sample.*

principle). The AFM tip dynamics during its operation is very sensitive to these interactions and their effect is reflected through the amplitude, the resonance frequency and the phase shift of the cantilever response. Various methodologies to operate an AFM in dynamic mode have been developed that rely on one of the above signals as the feedback parameter for the operation. Since these forces depend on the chemical and mechanical properties of the surface, their knowledge is imperative to gain insight into surface properties at the nanoscale.

Invention of the AFM made the measurement of these ultrasmall forces possible through the so called *atomic force spectroscopy* method. CM-AFM is the most commonly used operational mode to measure the tip-sample interaction forces, whereby the cantilever approaches and retracts from the sample at a fixed horizontal position while recording the cantilever deflection [5-8]. The tip-sample force is calculated from the deflection through the force constant. There are also FM-AFM based methodologies that enable the construction of force curves by monitoring the instantaneous cantilever frequency as a function of either the cantilever base position given a fixed excitation or amplitude, or the instantaneous oscillation amplitude given a fixed cantilever base position [9-13]. Since the relationship between the frequency shift and the tip-sample force gradient is known within reasonably good approximations, it is possible to calculate the force curves from the frequency response.

AM-AFM, also known as the tapping mode, is the most widely used intermittent-contact imaging method in air because the tip's interaction with the sample is relatively gentle, substantially eliminating plastic deformation and reducing

the sample volume involved in the tip-sample interaction, and also due to its relatively simple implementation [2]. However, extracting tip-sample interactions in AM-AFM mode has been difficult, mainly due to the complex tip dynamics resulting from jumps between attractive and repulsive force regimes, known as bistability. Sahin *et al*. have recently developed an experimental method to simultaneously acquire the topography and tip-sample force curves throughout the surface [14]. Their approach is based on the use of a torsional harmonic cantilever (THC) tip that combines active flexural and passive torsional vibrations. The flexural vibration is operated in standard AM-AFM mode while passive torsional vibrations are excited by the torque generated through impact between the laterally asymmetric cantilever and the sample. The use of the harmonic oscillator approximation to describe the torsional vibrations allows the extraction of the tip-sample force curves through spectral inversion in Fourier space.

In spite of the capability to measure tip-sample forces, all of the force spectroscopy methods except the one developed by Sahin *et al.*, have a fundamental shortcoming that they are not real-time procedures and require a surface map by performing imaging first in order to acquire force curves at chosen horizontal positions on the surface, making it a slow and selective process. Even though simultaneous acquisition of topography and tip-sample forces has been made possible with the use of the THC, there exist challenges in the characterization of hard samples with this approach. Addressing the lack of a robust force spectroscopy approach that can construct force curves in the 3-dimensional space above the sample in real-time

has been a long-time objective of the AFM research community and is one of the goals of this dissertation.

Complementary to its applications in high-resolution imaging and measurement of conservative tip-sample forces, AFM is also widely used for measuring dissipation on the surfaces (by measuring the loss of energy by the oscillating cantilever due to tip interactions with the surface and the damping of the medium) [15-18]. Dissipative interactions between tip and sample can arise from various sources, such as viscoelasticity, surface adhesion, tip-sample hysteretic losses and electrostatic forces [19-22]. Typically, when the operation is in ambient air, there is always some surface contamination that causes dissipative interactions. Different surface parameters are responsible for the interactions of conservative or dissipative nature, thus it becomes important to interpret the images obtained in dynamic AFM in terms of these interactions in order to gain insights into the surface composition.

In the AM-AFM imaging, where the observables are amplitude error and phase shift between the response and the drive, it has been discussed numerically and with analytical approaches that the phase shifts are directly related to the energy dissipation on the surface [15, 16, 23]. Mathematical formulations show that in the absence of dissipation, the phase shift and oscillation amplitude are not independent and since the amplitude is fixed at a setpoint value during imaging, the phase image will exhibit no contrast, that is, the phase shift is independent of variations in surface elastic properties. Sometimes, an exception to this results due to the bistable behavior of the tip in AM-AFM, which causes it to jump between attractive and repulsive

interaction regions, that is, between two sides of resonance phase shift of 90^{o}, giving a non-dissipative phase variation.

FM-AFM images, on the other hand, are relatively straightforward to interpret in terms of conservative and dissipative interactions, when the operation is in constant-amplitude mode (CA-FM). This imaging method was originally developed for non-contact operation in ultrahigh vacuum with two controls, first to maintain the excitation frequency at the effective resonance, and second, to simultaneously maintain a constant oscillation amplitude by adjusting the drive [3]. Its applications have since been extended to air and liquid environments as well and it has been extensively studied computationally and analytically that the observables, frequency shift and drive amplitude, can directly map conservative and dissipative interactions on the surface, respectively [11, 24]. However, due to the constant oscillation amplitude, the imaging in this mode was characterized by strong mechanical contacts with the sample. To overcome this issue, its operation in constant-excitation mode (CE-FM) was also incorporated, which differs from CA-FM in that the excitation amplitude is kept fixed and the response amplitude changes as a result of tip-sample interactions [25, 26]. However, for CE-FM operation, the effects of conservative and dissipative interactions are coupled in the output variables.

Multifrequency AFM operation has emerged as a promising technique due to its capability to achieve enhanced surface compositional sensitivity through the higher eigenmode response. This is because in contrast to the fundamental cantilever eigenmode in the conventional imaging, which scans the topography by controlling a response variable through setpoint feedback, the higher eigenmodes freely respond to

the variations in surface properties over a larger range of tip-sample interactions. Also, the complex nature of the tip-sample interactions requires a number of parameters to define it even with the simplest models, which means that the extra characterization channels obtained from higher eigenmodes can be significant in fully describing the surface properties. The improved sensitivity of higher modes was first demonstrated with the excitation of two eigenmodes, namely bimodal AFM operation, where the first mode was controlled in non-contact AM-AFM to perform topographical scan and the second mode was excited in open-loop, that is, with a fixed drive at its free resonance frequency without any feedback control [4]. Higher contrast in the phase image of second mode was seen in the operation in ambient air for conservative interactions [27]. This technique has since been extended to intermittent-contact operation in air and liquid [28, 29]. Furthermore, bimodal operation has also been implemented with simultaneous CA-FM control of the first and second eigenmodes in ultrahigh vacuum non-contact mode operation, where the first mode is used to scan the topography and the frequency shift associated with the higher mode maps the elasticity of the surface with atomic resolution [30, 31]. However, the applications of multifrequency operation in measuring surface dissipation are still in the development stage and not completely explained.

1.2 Motivation and challenges

It is clear that the force spectroscopy is an important application of AFM as the knowledge of the interaction forces is necessary to gain insights into a surface at nanoscale and atomic level. Even though the measurement of tip-sample forces has

been successfully achieved by using both the static and dynamic modes of AFM and is routinely performed for determining mechanical, electrical and magnetic properties of the samples, there are challenges that most of the existing techniques are presented with, which include the following:

1. Static mode spectroscopy techniques are limited by the large loading friction forces that occur during the operation,
2. The force curve measurements are not performed simultaneously with imaging, i.e., all the static and dynamic spectroscopy methods can only provide the force curve at a selected fixed horizontal position on the sample at a time, which makes the acquisition a slow process, and
3. With the exception of the THC method, which works well for soft samples, developing a 3-dimensional representation of the tip-sample forces requires fine-grid scanning of a *volume* above the surface, which can take hours to days. Also, doing so requires a highly controlled environment in order to avoid any drift of the tip above the surface, which can result in misinterpretation of the surface properties.

The primary motivation was to address the above challenges with the development of versatile dynamic force spectroscopy methods that can simultaneously perform topographical imaging and measure tip-sample forces. The emergence of experimental bimodal imaging operation provided further directions to achieve this objective by developing a method that can utilize the information contained in the output channels of the higher eigenmode.

Furthermore, the work in this dissertation derives motivation from the fact that the multifrequency AFM approach is still in the early stages of its development and holds potential to be explored further for its applications in compositional mapping of the surfaces. An extensive literature survey is conducted to understand the current state of the art and to lay out the directions for further study. One of the interesting findings is that the multifrequency methods have thus far been limited to the excitation of two cantilever eigenmodes (bimodal operation). Also, within the bimodal operation, for the applications in ambient air, the control of the higher eigenmode has been performed in the open-loop combined with AM-AFM control of the fundamental eigenmode, whereas the frequency-modulated control of the higher mode has been incorporated only in the ultrahigh vacuum conditions in non-contact mode, simultaneously with FM-AFM control of the fundamental eigenmode. Due to the individual applications of each excitation scheme, as briefly discussed in the previous section, combining the two approaches in a single imaging operation by simultaneous excitation of three eigenmodes may be useful in the separation of conservative and dissipative processes on the surfaces. Additionally, a comparative study of the higher eigenmode operation in FM and open-loop controls is important to obtain guidelines for the multifrequency imaging in air.

1.3 Dissertation objectives

The challenges discussed in the previous section elucidate the importance of a robust force spectroscopy method. Also, bimodal imaging developments have highlighted the usefulness of exciting higher eigenmodes to obtain information about

surface properties. This dissertation is aimed at developing applications of the multifrequency excitation approach for the acquisition of tip-sample force curves and for obtaining quantitative information about the surface properties during imaging. The computational and experimental results for the proposed methods are discussed within their respective applications. The main objectives can be summarized as:

1. Development of a detailed multiscale simulation methodology combining atomistic and continuum simulations in order to develop models for tip-sample interaction forces and study their influence on the response of the oscillating cantilever for the proposed methods.
2. Formulation of novel force spectroscopy methods that enable acquisition of high-resolution representations of the tip-sample forces in the 3-dimensional space located above the sample, simultaneously with topographical imaging.
3. Development of analytical models in order to validate the proposed force spectroscopy methods through numerical simulations.
4. Assembling of an experimental AFM system that is capable of operating the cantilever using amplitude-modulation, frequency-modulation and multifrequency excitation controls.
5. Commissioning of trimodal characterization procedure to simultaneously measure topography, phase and frequency shift contrasts through the excitation of three cantilever eigenmodes.
6. Experimental analysis and comparison of the ability of open-loop and frequency-modulated control methods for driving higher eigenmodes and mapping conservative and dissipative sample properties in multifrequency AFM.

2. Literature review

As the scale of scientific research and technology continues to decrease in size, the demand for improved tools to accurately obtain information about the surfaces at the nanoscale continues to increase. The introduction of the scanning tunneling microscope (STM) in 1981 by Binnig, Rohrer, Gerber, and Weibel made it possible, for the first time, to visualize in real space, the individual surface atoms of flat samples [32, 33]. Within one year of its invention, Binning *et al.* imaged the adatom layer of Si(111)-(7x7) with an STM. Since STM works on the principle of tunneling current that flows between a biased tip close to a sample, despite its phenomenal success, it was limited in its use to conducting samples. Also, during early STM

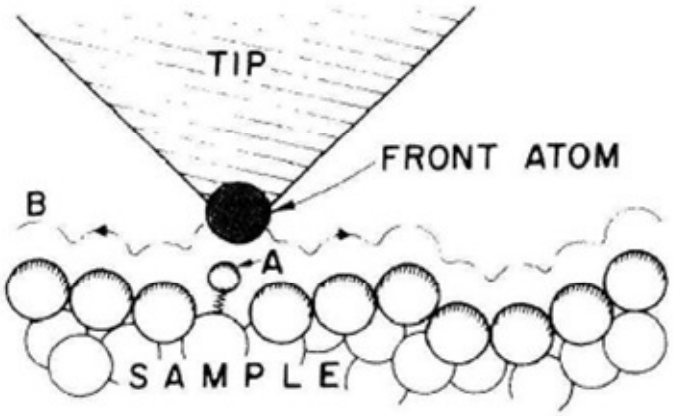

Figure 2-1 *STM or AFM tip close to a sample [1].*

experiments, it was observed that whenever the tip-sample distance is small enough that a current can flow, significant forces will act collaterally with the tunneling current (Figure 2-1). It was speculated soon that these forces could be put to a good use. Motivated by the inability to image insulated surfaces and information that can be harnessed from the atomic-level forces, the atomic force microscope (AFM) was

invented by Binnig, Quate and Gerber in 1986 [1]. It is difficult in an STM to isolate all force effects, therefore, the need for a dedicated sensor arose in order to detect the normal tip-sample forces. This property was fulfilled with a cantilever beam because it is rigid in two axes and relatively soft in the third. Since then, AFM has evolved into a powerful tool for the imaging, characterization and manipulation of materials at the nanoscale. Developments have occurred on all fronts of AFM, ranging from tips, materials and equipment to the modes of operation.

The basic layout of a typical AFM is shown in Figure 2-2. The AFM is centered around a microscale cantilever with a sharp tip at the free end, which serves the purpose of a force detector and a scanning probe. The tip can have a radius of

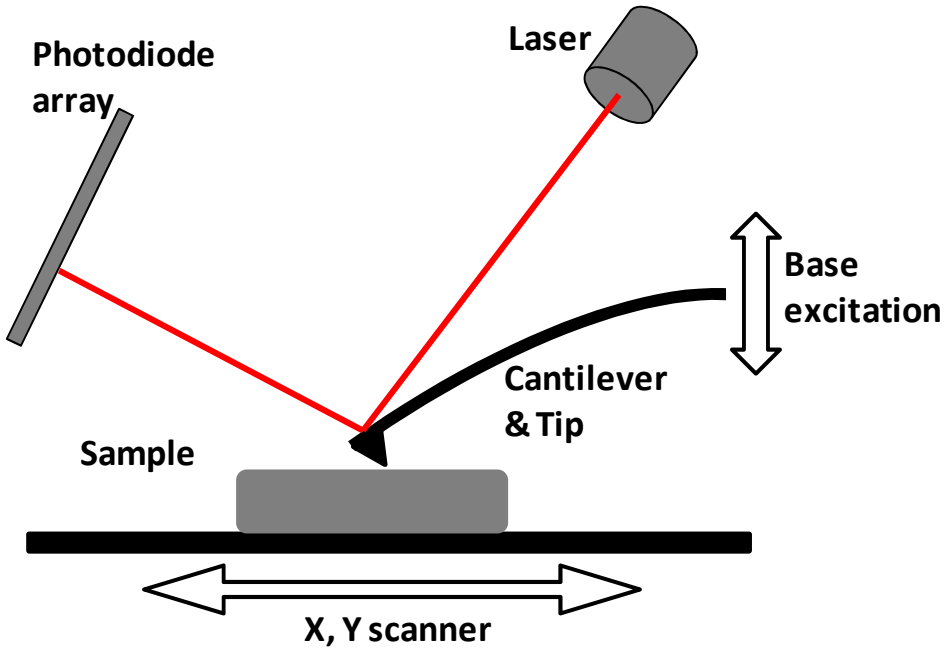

Figure 2-2 *Basic components of an AFM.*

curvature ranging from a few nanometers to many microns and is available in a wide variety of geometric shapes. The motion of the cantilever base and sample scanner are most commonly controlled by using piezo tubes. In dynamic modes of AFM

(discussed later), the AFM tip is excited through various means including magnetic excitation, acoustic excitation, or base excitation via piezo tubes. The motion of the tip is generally measured by using an optical lever system, in which a laser reflects off the exposed side of the cantilever onto an array of photodiodes, and the voltage difference provides the deflection signal of the cantilever. Various applications of the AFM are explained further in this chapter to understand the current state of the art.

2.1 AFM modes of operation

2.1.1 Static mode

Initially, when the AFM was invented, it was operated only in what is referred to as contact mode (CM) or static mode. In an AFM, the force F_{ts} that acts between the tip and the sample is used as the feedback signal for imaging. In the static mode of operation, the probe is always in contact with the sample and the force translates into deflection ($=F_{ts}/k$) of the cantilever, where k is the cantilever stiffness. Since the deflection of the cantilever should be significantly larger than the deformation of the tip and sample, restrictions on the useful range of k apply. In this mode, the cantilever should be much softer than the bonds between the bulk atoms in the tip and sample in order to sense the small forces. The operation principle is based on maintaining a set-point tip deflection during imaging, which essentially means maintaining a constant tip-sample interaction force. The set-point value is prescribed by the user and its value determines the force exerted on the sample by the tip.

Despite being the simplest mode of operation, CM-AFM mode suffers from some intrinsic disadvantages. Atomic resolution images have been demonstrated with

the static mode [34, 35], yet the method can only be applied in certain cases. Since the quality of image depends on the applied force (deflection) for different surface features, sometimes the required repulsive forces can be so high that they can irreversibly damage the sample. Also, since the tip is dragged along the sample, lateral friction forces are also present, which in turn, are dependent on the normal tip-sample interaction force and an increase in their value could damage the sample through tearing. Nonetheless, while there are difficulties associated with the static mode operation, the physical interpretation of the image is simple: the image is a map $z(x, y, F_{ts} = constant)$.

2.1.2 Dynamic mode

A significant transformation in the operation of the AFM occurred with the use of a vibrating tip to explore the surface topography. It has become possible to obtain high resolution images of DNA, proteins and polymers in air and liquids with the dynamic modes of AFM [36-39]. True atomic resolution images of several semiconductor and insulator surfaces have also been reported for the vacuum operation [40-42]. Furthermore, dynamic AFM modes are being applied to develop methods for nanometer-scale modification and patterning of surfaces. Also, the potential to develop quantitative methods to characterize material properties at the nanometer scale, in addition to the capability of achieving high resolution, makes dynamic AFM modes more attractive to researchers.

In the dynamic modes, the underlying principle is vibrating the cantilever above the sample at or near a resonance frequency such that the tip is not always in contact

with the surface as in CM-AFM. The excitation can be provided at the base of the cantilever or at the tip through the use of magnetized tips (Figure 2-3) [2]. There exist several parameters such as amplitude, frequency and phase shift that are sensitive to the tip-sample interactions, and hence, link the dynamics of a vibrating cantilever to the forces. Typically, in dynamic modes of AFM, any one of these parameters is used as feedback to obtain the topography of a surface or the compositional contrast. The two most frequently used dynamic modes of AFM are amplitude modulation mode

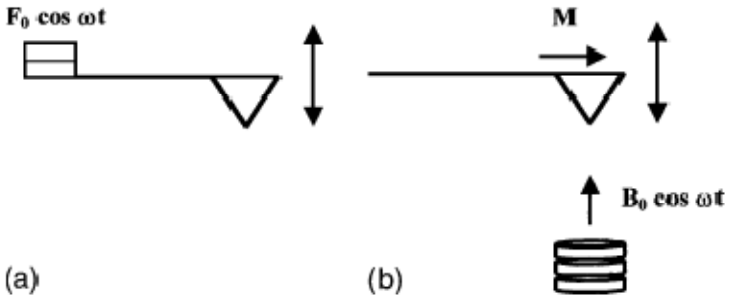

Figure 2-3 *Schematic depiction of acoustic (a) and magnetic (b) excitation methods in dynamic AFM [2].*

(AM-AFM) and frequency modulation mode (FM-AFM), in which, as the names suggest, amplitude and frequency, respectively, are used as the feedback parameters. In recent years, there has been further development in dynamic AFM operation with the excitation and control of multiple eigenmodes of a cantilever. In this case, the excitation signal is composed of the fundamental resonance frequency and higher eigenmode frequencies of the cantilever, making available additional characterization channels through the higher eigenmode responses. The most significant advantage of these approaches is that unlike the fundamental eigenmode, the higher eigenmode is usually not controlled by the setpoint feedback loop and is free to explore a fuller

range of tip-sample interactions. AM-AFM, FM-AFM and multifrequency AFM operations are discussed below in detail.

2.1.2.1 Amplitude-Modulation (AM) AFM

AM-AFM is a dynamic AFM mode in which the cantilever is excited at or around its fundamental resonance frequency in the absence of tip-sample interaction forces, with a free oscillation amplitude (free oscillation amplitude refers to the amplitude of a driven cantilever in the absence of any tip-sample interactions) that depends on the user-input drive amplitude [43]. A setpoint amplitude that is less than the free amplitude is also defined before the operation. As the cantilever is lowered toward the sample to attain the setpoint value, it begins to experience the interaction forces, which result in a change in the effective cantilever stiffness. Depending on the nature of the dominant forces, attractive or repulsive, the cantilever becomes softer or stiffer. This change in the stiffness causes the effective resonance frequency of the cantilever to change and the offset between the drive frequency and the new resonance frequency results in a change in the amplitude. The operation requires the amplitude to be maintained at the setpoint value, therefore, any variation from the setpoint value during surface scan causes the cantilever base to move up or down, which gives a map of the topography. It is also possible to map the variation in material properties by recording the phase shift between the driving force and the tip response [15, 16].

Despite being the most common application of dynamic AFM, AM-AFM has two major challenges, which can at times prevent it from producing useful images:

the mechanical bistability [2, 44] of the oscillating cantilever, which prevents stable imaging, and the relatively high tip-sample repulsive forces, which can damage biological and other soft samples. Bistability originates from the influence of the interaction potential, which is attractive at long ranges and repulsive at short ranges, on the near harmonic motion of the cantilever. As mentioned before, the cantilever stiffness changes with respect to its intrinsic force constant based on the regime it is operating in; this results in a phase difference between the drive signal and the

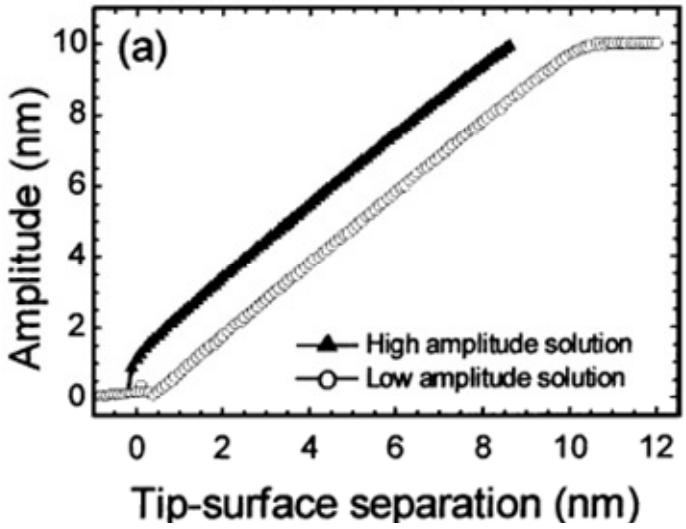

Figure 2-4 *Coexistence of two solutions for different tip-surface separations gives rise to bistability [2].*

cantilever response. Depending on the imaging parameters and physical properties of the system, discontinuous transitions can occur between the attractive and repulsive regimes, leading to distorted images that do not contain useful information. This coexistence of two solutions is shown in the Figure 2-4 [2]. If the cantilever oscillation takes place under the repulsive imaging regime, the tip-sample interaction forces can be quite significant, and since the transition between regimes is not always easy to avoid, sample damage remains a possibility when imaging delicate samples in AM-AFM mode.

2.1.2.2 Frequency-Modulation (FM) AFM

Atomic resolution was achieved in dynamic AFM with the introduction of a new mode of operation called FM-AFM by Albrecht *et al.* in 1991 [3]. This mode was developed with the objective of achieving high sensitivity measurements through increased quality factor (Q) of the oscillating cantilever. Increasing sensitivity by changing Q was not a possibility in AM-AFM operation due to linear increase in response time (the time required for the oscillations to reach the steady state τ) with increasing Q,

$$\tau = \frac{2Q}{\omega_o} \tag{2.1}$$

In FM-AFM imaging, the frequency shift is used as the feedback control parameter. As discussed before, changes in the force gradient result in changes in the effective frequency of the oscillation. The control scheme is designed such that the amplitude remains constant while the phase and frequency of excitation are adjusted. Consequently, the frequency shift between the response and the drive remains at a prescribed setpoint value, which is not necessarily equal to zero, and the phase difference between excitation and response is 90 degrees, ensuring maximum positive feedback. An image is formed by profiling the surface topography with a constant frequency shift. FM-AFM is most commonly performed in the non-contact mode (NC-AFM) because atomic resolution images were obtained without tip-surface mechanical contact. However, since the probe in that case does not really touch the sample, the true sample skin cannot be determined. This can lead to a tip broadening effect where the features of a sample appear wider than their actual size. An illustration of the effect of tip broadening is shown in Figure 2-5. It should, however,

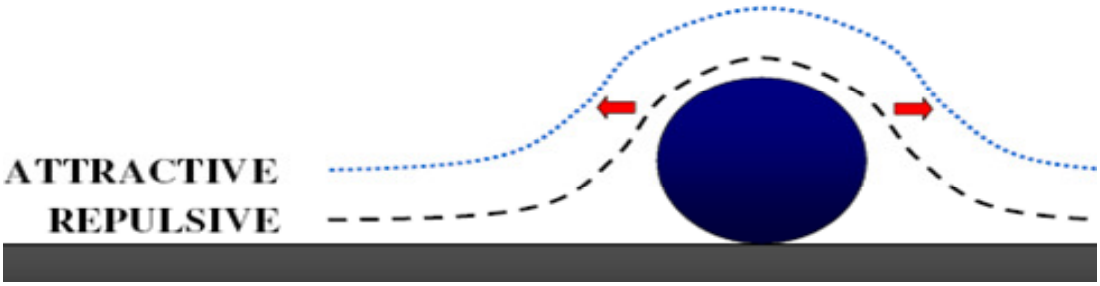

Figure 2-5 *Tip broadening effect during non-contact imaging.*

be noted that both modes (AM-AFM and FM-AFM) can be used in either intermittent-contact mode or non-contact operation.

Furthermore, initially the FM-AFM mode was incorporated in non-contact mode with a constant-amplitude operation (CA-FM), that is, the response amplitude of the cantilever is maintained constant by adjusting the drive when the tip is interacting with the sample. However, in intermittent-contact operation, especially for soft samples, this approach results in stronger mechanical contact between the tip and the sample, thereby increasing probability of damage. To address this, constant-excitation operation (CE-FM) was introduced in which the operation is maintained at resonance similar to CA-FM, but the drive amplitude is fixed and the response amplitude freely changes due to the tip-sample interactions [25, 26, 45].

With the knowledge of the modes of operation discussed above and their limitations, Solares has recently proposed two new dynamic modes of operation referred to as frequency and amplitude modulation (FAM-AFM) and frequency and force modulation (FFM-AFM) [46-48]. These modes combine the knowledge of AM- and FM-AFM and have been numerically shown to eliminate or reduce the existing problems of bistability, tip broadening and sample damage. The details of the method with the control schemes can be found in previous publications.

2.1.2.3 Multifrequency AFM

In multifrequency AFM operation, in addition to the fundamental eigenmode, one or more higher eigenmodes are also driven and controlled. Typically, the fundamental mode is used for the topographical scan while higher eigenmodes can be used to enhance the image contrast due to their high sensitivity to compositional variations. Figure 2-6 shows the basic experimental schematic of bimodal imaging operation that has an excitation function with two resonance frequencies [49]. The cantilever is driven with a linear combination of sinusoidal signals at or near two resonance frequencies. The resulting motion of the cantilever is measured and is used as the input for two lock-in amplifiers that use the two drive frequencies as reference.

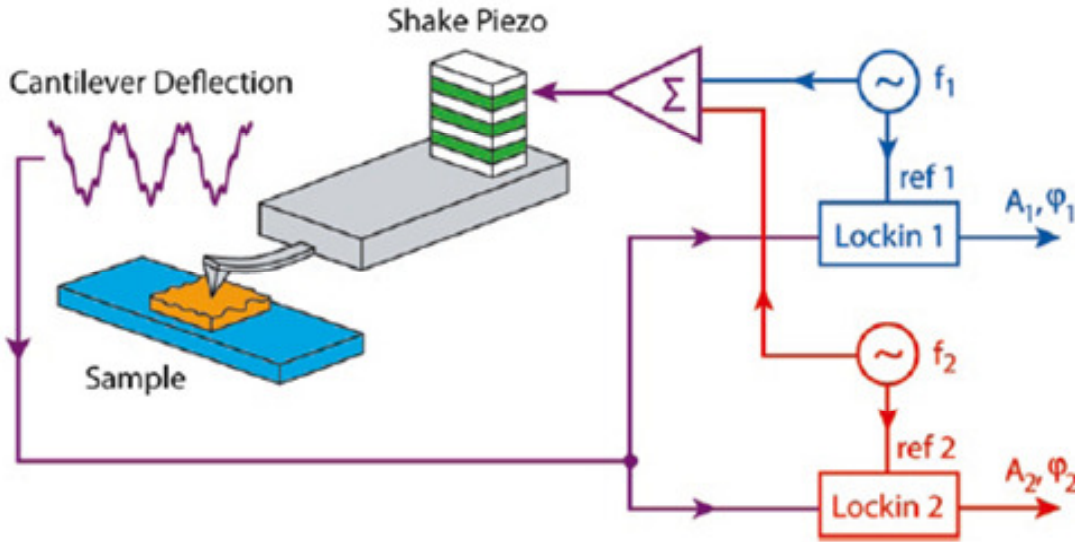

Figure 2-6 *In bimodal operation, the cantilever is both driven and detected at two frequencies. The sinusoidal drive signal is the sum of signals at frequencies f_1 and f_2. The cantilever deflection then contains information at both of those frequencies, as shown in the curve. The amplitude and phase at the two frequencies are then separated again by the two lock-in amplifiers. One or both of the resonance frequencies can be used to operate a feedback loop [49].*

The output of lock-in amplifiers, amplitudes and phases of the two eigenmodes, can then be processed to display the images or be used for the feedback loop.

The motivation for multifrequency operation was pioneering early work in non-contact bimodal AFM by Rodriguez and Garcia [4], where they pointed out that the second eigenmode response is sensitive to weak, long-range van der Waals interactions due to the non-linear coupling of the two oscillating modes (coupled through the tip-sample interactions) combined with the second mode's high quality

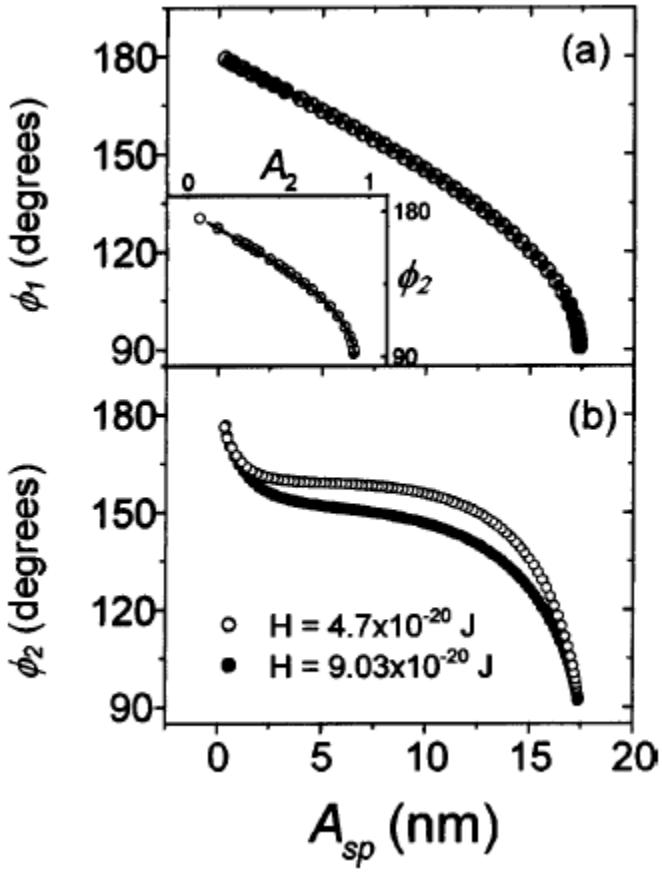

Figure 2-7 *Phase shift dependence on the first mode setpoint amplitude (A_{sp}) for two different Hamaker (H) values. (a) First eigenmode phase shift φ_1. The inset shows the dependence of φ_2 on its own amplitude. (b) φ_2 as a function of A_{sp} and H values [4].*

factor (Q). To demonstrate this through simulations, they used a continuous beam model and used a drive signal with fixed drive amplitudes, where the drive frequencies were chosen to be the free resonance frequencies of the first and second eigenmodes. Attractive van der Waals forces were modeled by the expression $F_{vdw} = -(HR/6d^2)$, where H, R and d are the Hamaker constant, tip's radius and tip-sample distance, respectively. In Figure 2-7, the dependence of phase shift of the first and second eigenmodes (φ_1 and φ_2) is shown with respect to the setpoint amplitude of the first eigenmode (A_{sp}). The Hamaker constant values were selected to describe two different interfaces. It can clearly be seen that φ_2 exhibits sensitivity to changes in H value when plotted against the first eigenmode setpoint amplitude, whereas both phases show no variation to H when plotted against their own amplitudes.

Furthermore, their research group verified experimentally the above observations by performing bimodal imaging in attractive and non-dissipative interaction regime and showed that the higher eigenmode phase exhibits about an order of magnitude higher sensitivity than the first eigenmode phase [27]. Here, the first eigenmode was controlled in AM-AFM and the second eigenmode was excited with a constant drive at its free resonance frequency. They observed that during imaging, where the variations in first mode phase were barely above the noise level, phase variations for the second mode showed enhancement of the material contrast by nearly a factor of 10.

In 2006, Proksch extended the bimodal operation to more common intermittent-contact imaging mode in air and liquid conditions [28], and illustrated the difference observed in the amplitude and phase contrasts of first and second eigenmodes. The

first eigenmode is operated in conventional AM-AFM mode and the second eigenmode response is used as the *carry-along* signal. He used a graphite sample for air operation and a DNA sample for imaging in water. Figure 2-8 shows a 30 μm image of a highly oriented pyrolitic graphite (HOPG) surface. The probe was a silicon AC240 cantilever from Olympus. The operation parameters were, A_1 ~ 8 nm, f_1 ~

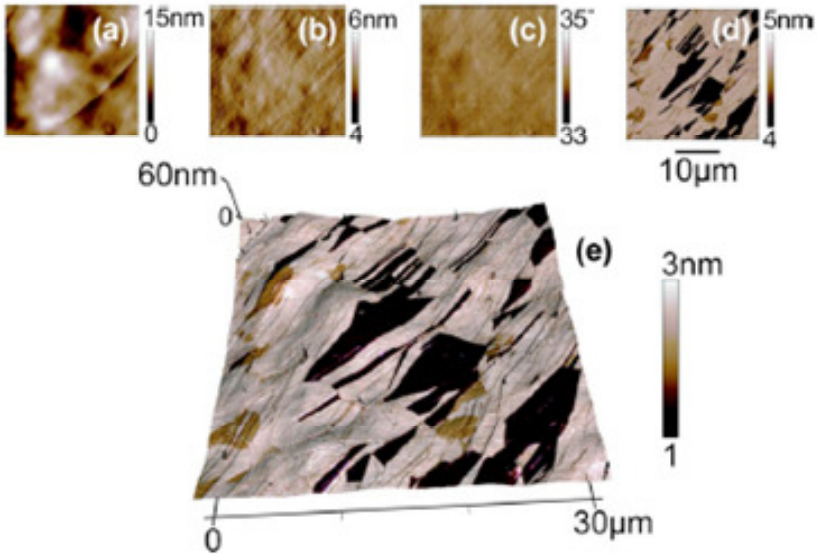

Figure 2-8 *HOPG surface, 30 µm scan. The cantilever was driven at its fundamental (~69.5 kHz) and second eigenfrequency (~405 kHz). (a) shows the topography and (b) is the fundamental amplitude channel, used for the feedback error signal. The fundamental phase image (c) shows an average phase lag of ~34° indicating that the cantilever was in repulsive mode for the entire image. The second mode amplitude is shown in (d). The three dimensional rendered topography colored with the second mode amplitude is shown in (e). This method of display allows easy spatial correlation of the two channels [28].*

69.5 kHz, A_2 ~ 8 nm, f_2 ~ 405 kHz. The fundamental phase (c) shows very little variation ($\leq 1^o$ standard deviation), exhibiting almost no contrast. The second mode amplitude image (d) however, has significant contrast, with broad patches where A_2 was reduced by the tip-sample interactions. The second mode amplitude rendered on

the topography obtained using the first mode is shown in (e), and some boundaries can be seen in the image that have no correlation with the topographical features. He observed that contrast could be seen in the first mode phase images as well upon fine tuning its parameters after having prior knowledge from the second mode phase images. Similar observations were made for imaging in liquid as well on a high density λ-digest DNA sample that was prepared in a dense mat on freshly cleaved mica. The cantilever used for imaging in liquid was a 60μm long Olympus Bio-Lever, with operating parameters, A_1 ~ 8 nm, f_1 ~ 8.5 kHz, A_2 ~ 5 nm and f_2 ~ 55 kHz.

The applications of bimodal AFM have been further extended to operation in ultra-high vacuum with its recent implementation by Meyer and coworkers, and Sugawara and coworkers [30, 31]. As discussed before, FM-AFM is the more suitable operation mode in vacuum, their method consists of simultaneously driving the fundamental eigenmode plus the second or third eigenmode in non-contact FM-AFM, each through a separate phase-locked-loop (PLL) circuit [50]. The first eigenmode frequency shift Δf_1 has been used as the feedback parameter to control the tip-sample distance for imaging. As has been discussed earlier that if $A_2 << A_1$, Δf_2 is proportional to the tip-sample force gradient averaged over the large oscillation at f_1 and hence, can be used to measure the elasticity variations on the surface [51, 52]. Figure 2-9 shows images obtained by Meyer *et al.* [31] on a KBr sample using a Nanosensors PPP-NCL cantilever with operation parameters, A_1 ~ 10 nm, f_1 ~ 154.021 kHz, A_2 ~ 50 pm and f_2 ~ 960.874 kHz. The images shown are for decreasing tip-sample distance controlled by varying Δf_1 in steps of -2.0 Hz from -14.0 Hz to -20.0 Hz. It can clearly be seen that the modulation of Δf_2 is about 10 times stronger

than the modulation of Δf_1. The distortions observed in the Δf_2 images in going to more negative Δf_1 (figure d) are attributed to reversible tip deformations.

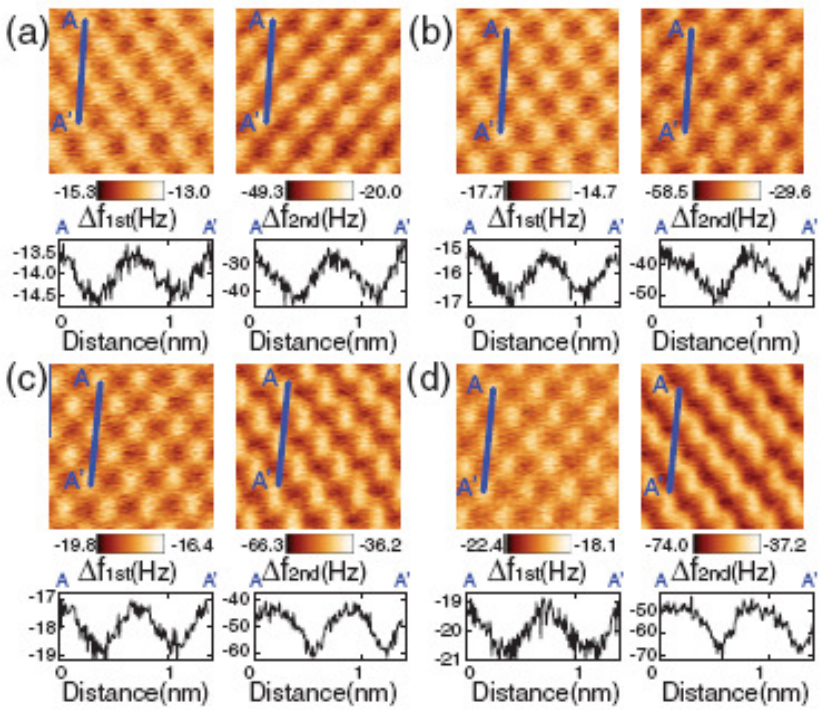

Figure 2-9 *Atomically resolved bimodal AFM images of a KBr(001) sample obtained at a series of quasiconstant heights and corresponding line profiles along A-A'. The left and right maps show Δf_1 and Δf_2, respectively. Imaging parameters; (a) Δf_1 = -14.0 Hz, (b) Δf_1 = -16.0 Hz, (c) Δf_1 = -18.0 Hz, and (d) Δf_1 = -20.0 Hz.; f_1 = 154.021 kHz, A_1 = 10 nm, Q_1 = 31059, f_2 = 960.874 kHz, A_2 = 50 pm, Q_2 = 6246 [31].*

Related to the above discussed multifrequency operations is also the use of higher harmonics of the fundamental eigenmode to extract information about material properties or to improve the instrument sensitivity. Stark *et al.* have demonstrated higher order harmonic imaging of heterogeneous samples [53, 54]. Sahin *et al.* have developed specialized cantilevers such that the higher eigenmodes coincide with fundamental mode harmonics to exploit the sensitivity of higher harmonics to measure material properties [55 ,56]. Balantekin *et al.* have imaged surfaces by using the third-harmonic amplitude [57, 58], and Crittenden *et al.* have demonstrated that

the higher harmonic responses are sharper than the fundamental mode [59]. Furthermore, other multi-frequency AFM characterization approaches exist with direct and indirect excitation of the higher eigenmodes of the cantilever, such as dual-frequency resonance tracking [60], intermodulation AFM [61], band excitation [62], variations of the method introduced by Garcia and coworkers, in which the second excitation is not operated close to an eigenfrequency [63, 64], and constant-amplitude phase-modulation with the acquisition of phase contrast through the second eigenmode [65]. However, all these approaches are not directly relevant to the goals of this dissertation and will not be discussed in detail.

2.2 Atomic force spectroscopy

Force spectroscopy is an AFM technique used to measure a local force acting on the tip exerted by a sample with spatial resolution on the nanometer scale. Since these ultrasmall forces depend on the mechanical, magnetic, electrical and chemical tip and sample properties, their knowledge is vital in order to obtain the information about the surface processes. For this reason the measurement of tip-sample force curves has become essential in different fields of research such as surface science, materials engineering, and biology. In this section, various existing force spectroscopy methods using static and dynamic modes of AFM have been discussed.

2.2.1 Force spectroscopy using static AFM

Contact mode (CM-AFM) [6-8] is the most commonly used operational mode to acquire the force curves. While AFM imaging is performed by scanning the sample

(or tip) horizontally in two dimensions, force spectroscopy is done by approaching and retracting the tip (or sample) in the vertical direction. The force-distance curve refers to a plot of the tip-sample interaction force versus the tip-sample distance. In order to obtain these plots, the cantilever deflection δ_c is measured while the tip (or the sample) is translated along the vertical axis. The cantilever bending force is given

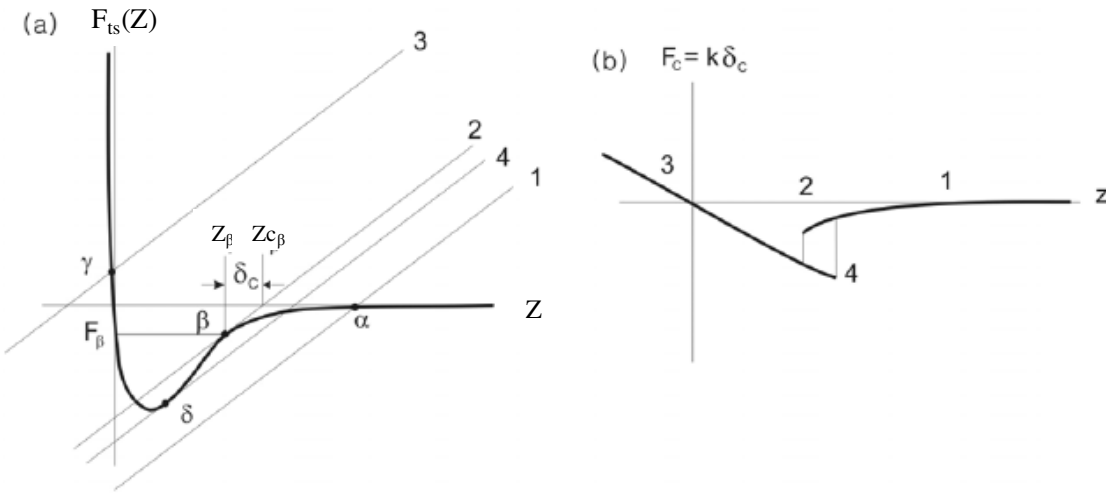

Figure 2-10 *(a) The curve $F_{ts}(Z)$ shows the typical shape of the tip-sample interacting force. The lines 1–4 show F_c as a function of Z. In an equilibrium state, the $F_{ts}(Z)$ should be equal to F_c and that point is given by the intersection (α, β, γ, δ) of two lines. At the intersection point β, F_β is the interacting force, Z_β is the tip-sample distance and the δ_c is the cantilever bending distance. (b) Interaction force as a function of distance. The interaction force is equal to F_c which bends the cantilever. This force is determined by δ_c depicted in (a) [5].*

by Hooke's law ($F_c = -k\delta_c$), where k is the cantilever stiffness and F_c the elastic force of the cantilever. The AFM force curve is given by balancing two contributing forces, which are the tip-sample interaction force $F_{ts}(Z)$ and F_c. By using the graphical interpretation shown in the Figure 2-10 [5], one can understand the resulting force-

displacement curve. In Figure 2-10a the curve $F_{ts}(Z)$ shows the typical shape of the tip-sample interaction force as a function of the distance Z. If Z_c is the initial tip-sample distance, $Z = Z_c - \delta$, and therefore, $F_{ts} = k(Z - Z_c)$. The lines 1-4 in the figure show F_c as a function of Z. In an equilibrium state, $F_{ts}(Z)$ should be equal to F_c and that point is given by the intersection (α, β, γ, δ) of two lines. At the intersection point β for example, the Z value is the real distance between the tip and the sample. The controllable (or measurable) value Z_c is given by the intersection between line 2 and the x-axis, and the δ_c is determined by the difference between Z_β and $Z_{c\beta}$ as depicted in the graph. The value we want to know is the force between the tip and sample which is equal to $F_c = k\delta_c$.

In Figure 2-10b the resulting force–displacement curve is illustrated. At each distance, the cantilever is bent until the elastic force of the cantilever becomes equal to the tip–sample interaction force. In this way, the system reaches equilibrium. When the tip is far from the sample (1), $F_{ts}(Z)$ is close to zero. At the intersecting point α in Figure 2-10a, δ_c is also close to zero, as indicated in (*b*). As the tip approaches the sample, the difference between Z and Z_c will grow monotonically. Because Z_c is larger than Z, δ_c and F_c are negative numbers, there is an attractive force. At point β, an abrupt change occurs that is called *jump-to-contact*. The jump-to-contact means that the cantilever bent by the attractive force jumps to the surface of the sample. At γ, F_c becomes a positive value meaning repulsive force. Since the repulsive force $F_{ts}(Z)$ is very stiff, in the region near 3 in Figure 2-10b the force curve is close to a straight line. In a retracting process, the cantilever will follow the trace from 3 to 4 producing a hysteresis loop. At point δ, there is another abrupt change called *jump-off-contact*,

which means that the tip is separated from the sample surface, all of a sudden. The curves shown in Figure 2-10b are called force–displacement *hysteresis* curves. On the other hand, in the case of a stiff cantilever (k is larger) the slopes of lines 1, 2, 3 and 4 are steeper. Then, the abrupt change at β and δ will not occur and no hysteresis will be observed.

2.2.2 Force spectroscopy using dynamic AFM

There are also dynamic-mode AFM methodologies that are frequently used for the construction of the force curves by monitoring the amplitude change or the frequency change of the cantilever when it is interacting with the surface. It is well known that the resonance response of the cantilever is very sensitive to the external perturbations, which results in changes in the amplitude and frequency under the influence of interaction forces. This can be explained by approximating the motion of a vibrating tip in a dynamic mode by a point-mass model equation of motion,

$$m\frac{d^2z}{dt^2} = -kz - m\frac{\omega_o}{Q}\frac{dz}{dt} + F_{ts}(Z) + F_0\cos\left[\omega(t)t\right] \tag{2.2}$$

where t is time, z is the instantaneous tip position with respect to its equilibrium rest position, k the harmonic force constant for the displacement of the tip with respect to its equilibrium rest position, m the cantilever's effective mass, $\omega_o = 2\pi v_o = (k/m)^{1/2}$ the free resonant angular velocity (v_o is the free resonant frequency), Q the quality factor, Z the instantaneous tip position with respect to the sample $(Z_c\text{-}z)$, $F_{ts}(Z)$ the *vertical* component of the tip-sample interaction force, and $F_0cos[\omega(t)t]$ the oscillating excitation force applied to the cantilever.

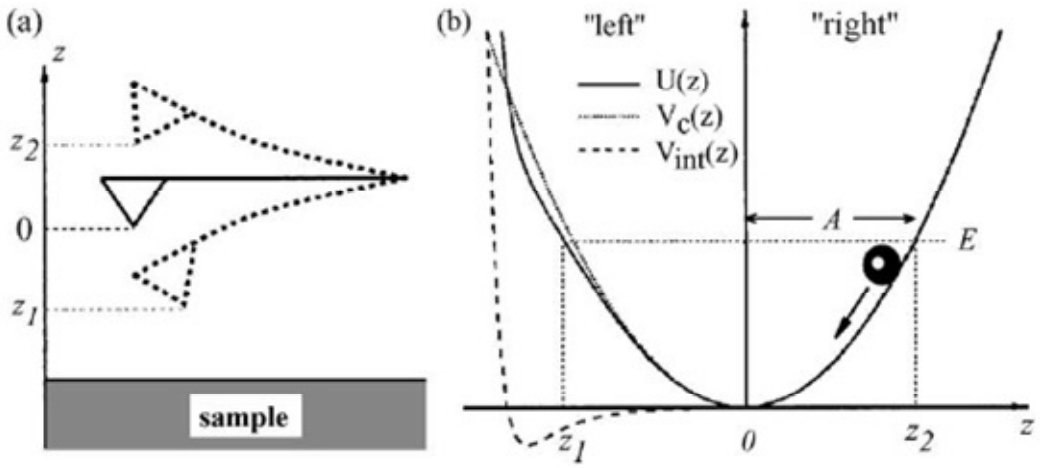

Figure 2-11 *The effective tip potential (solid line) is the sum of the parabolic cantilever potential (dotted line) and the tip-sample interaction potential (dashed line) [2].*

The above equation is that of a damped harmonic oscillator if the tip-sample interaction force term, $F_{ts}(Z)$, is not present. However, this harmonic behavior is altered when the tip is brought closer to the sample due to the change in the potential that determines the response. The effective potential becomes the sum of the harmonic potential of the free cantilever (U) and the tip-sample interaction potential (V_{int}). This effective potential (V_c) has an asymmetric shape (Figure 2-11) and the tip oscillation becomes anharmonic, i.e., the frequency of the oscillation depends on the amplitude [2]. Considering the tip-sample interaction potential as a parabolic potential $(\alpha\, z^2)$, the force would be proportional to z, and the force gradient would be constant. We can write the force as,

$$F_{ts} = \left(\frac{dF_{ts}}{dZ}\right) z + const \tag{2.3}$$

By inserting this in the equation of motion, one can obtain an effective spring constant k_e and hence, a modified resonance frequency,

$$\omega_e = \sqrt{\frac{k - (dF_{ts}/dZ)}{m}} \tag{2.4}$$

This approximation of parabolic potential is valid in most cases for weakly perturbed tip-sample interactions. The small change in the resonance frequency, calculated using the equation 2.4, result in change in oscillation amplitude and phase shift between the drive and the response of a cantilever. The inversion of output variables to force curves using commonly used dynamic modes of operation has been discussed in this section.

Even though AM-AFM is experimentally easier to implement, more commonly used for operation in air and its dynamics has been extensively studied and understood by analytical and numerical methods, there had been a lack of understanding about the inverse problem of how to extract the tip-sample interactions from the measured variables (oscillation amplitude and phase shift between the drive and the response). This is mainly because of the bistable and hysteretic behavior, as discussed in the previous section, which makes the analysis complicated. This was until 2006, when Lee and Jhe [66] presented a rigorous derivation of characteristic differential equations 2.5 and 2.6, as shown below, describing the interaction forces, which can be numerically integrated to determine the unknown interactions from the cantilever response measured with respect to the vertical tip-sample distance.

$$\sum_{k=0}^{\infty} \frac{A^{2k+1}(z)}{2^{2k+1}k!\,(k+1)!} \frac{d^{2k+1}}{dz^{2k+1}} F_c(z) = -\frac{F}{2} sin\theta(z) + \frac{A(z)}{2}(k - m\omega^2), \tag{2.5a}$$

$$\sum_{k=0}^{\infty} \frac{A^{2k}(z)}{2^{2k+1}k!\,(k+1)!} \frac{d^{2k}}{dz^{2k}} \Gamma(z) = \frac{1}{2}\left(\frac{F}{A(z)\omega} cos\theta(z) - b\right) \tag{2.5b}$$

with the boundary conditions,

$$\frac{d^k}{dz^k}F_c(z) = \frac{d^k}{dz^k}\Gamma(z) = 0 \; as \; z \to \infty, k = 0, 1, 2, ... \tag{2.6}$$

where z is the vertical position of the cantilever base above the sample, $A(z)$ the response amplitude, $\theta(z)$ the phase shift of the oscillation, F the driving force, k the cantilever stiffness (the index k represents the order of the differential equation), m the effective mass of the probe, ω the excitation angular frequency, $\Gamma(z)$ the effective damping coefficient of a given dissipative interaction, and b is the damping coefficient of the environment cantilever is oscillating through.

To demonstrate the validity and accuracy of the method, they assumed an interaction model comprising conservative and dissipative tip-sample forces to simulate the cantilever motion using the damped harmonic oscillator equation. They compared the force curves plotted using the analytical model with the force curves constructed by using the response amplitude and phase shift values obtained from the simulation in the above equations, and showed that the agreement improved by considering the higher order solutions of the equation.

FM-AFM, on the other hand, is well formulated and more straightforward for theoretical analysis. FM-AFM spectroscopy is usually performed by monitoring the instantaneous cantilever frequency as a function of either the cantilever base position given a fixed excitation or amplitude, or the instantaneous oscillation amplitude given a fixed cantilever base position [9-13, 67]. As discussed earlier, the harmonic approximation provides an understanding of the relationship between frequency shift and tip-sample interaction force gradient, given by equation 2.4. The first-order approximation of this equation can be written as,

$$\Delta f \approx -f_0 \frac{k_{ts}}{2k} \tag{2.7}$$

where k_{ts} is the force gradient, f_o the free resonance frequency and k is the cantilever stiffness. The same relationship has been derived using many other approaches and is used frequently for constructing the force curves [68-70]. However, this relationship is useful only for small amplitude oscillations because it is based on the assumption that the distance dependence of the force is linear in the range of the cantilever motion, i.e., the force gradient is constant. For oscillations with large amplitudes, Giessibl [71] reported an analytical expression derived using the perturbation theory and relates the frequency shift to tip-sample forces,

$$\Delta f(z) = \frac{f_o^2}{kA} \int_0^{1/f_o} F_{ts}(z + A\cos(2\pi f_o t))\cos(2\pi f_o t)dt \tag{2.8}$$

where z is the vertical base position of the cantilever, A is the oscillation amplitude and $\Delta f(z)$ is the frequency shift as a function of z.

For the validation of the expression in equation 2.8, he conducted an experiment for a tungsten tip on a KCl(100) surface. Figure 2-12a shows the experimental frequency shift data calculated over a z range of 3 nm with steps of 25 pm. The operation parameters are, f_o = 25.0684 kHz, k = 1800 N/m and A = 0.15 nm. Figure 2-12b shows the corresponding tip-sample force calculated using the equation. The ability to perform inversion of the frequency shift data to force curves is very useful in the interpretation of images obtained in FM-AFM in terms of surface parameters. In addition to this, various other FM-AFM approaches have been proposed for achieving the same objective. A numerical method was introduced by Gotsmann *et al.*

[10]. Dürig and also Hölscher *et al.* proposed semianalytical methods for the deconvolution of the frequency shift data [12, 70].

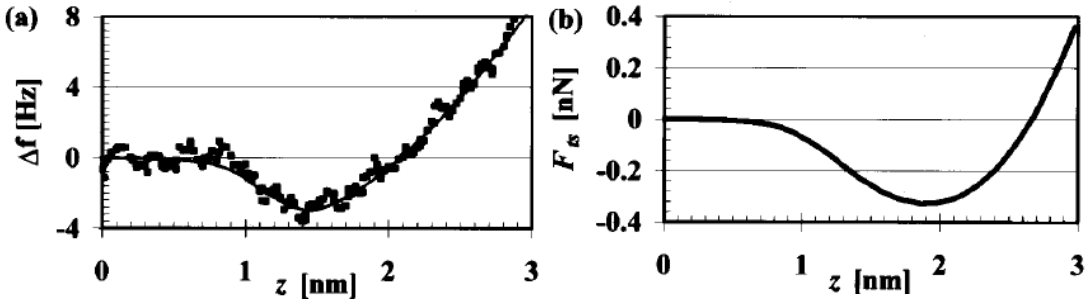

Figure 2-12 *(a) Experimental data of Δf (squares) for a tungsten tip and a KCl sample, recorded with an amplitude of A = 0.15 nm, a spring constant of k = 1800 N/m and f_o = 525.0684 kHz. The solid line is a smoothened curve used for the deconvolution; (b) tip–sample force $F_{ts}(z)$ corresponding to the Δf(z) data in (a) [71].*

The spectroscopy methods discussed so far in contact mode or dynamic mode are capable of measuring the tip-sample interactions but are deficient in that they can only provide the force curve at a fixed horizontal position on the sample at a time. Once the sample image is obtained, one has to move the tip to the point where the measurements are required and perform the tip approach and retract on the sample. Therefore, constructing force curves on multiple sample points to characterize the entire three-dimensional space above the surface could be a lengthy process. Recently, Albers *et al.* [72] reported an FM-AFM based method (similar work has been done in the past by Hölscher *et al.* [73]), where they have acquired *3D* force maps. First, they developed an AFM system capable of achieving atomic resolution in non-contact mode operation in ultrahigh vacuum conditions at low temperature. Figure 2-13a shows an individual force curve on the HOPG sample, recorded at T = 6 K with oscillation amplitudes of 0.25 nm, to demonstrate their instrument's capability

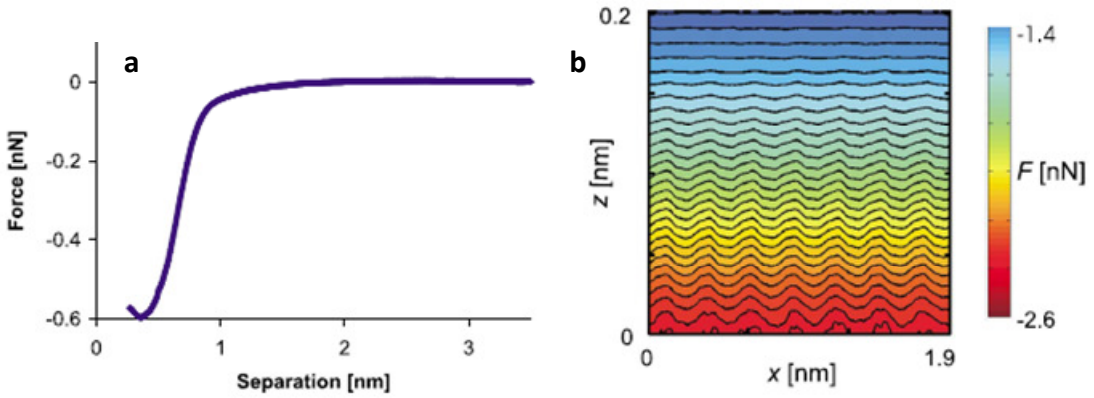

Figure 2-13 *(a) Force curve obtained on HOPG with an oscillation amplitude of 0.23 nm, (b) Two-dimensional array of 256 force curves recorded along a line of 1.9 nm length on HOPG. Contour lines of equal force, plotted every 40 pN, visualize force variations that are induced by the atomic lattice of the graphite sample [72].*

for force spectroscopy. A total of 256 curves are combined, as shown in Figure 2-13b, to form a two-dimensional, site-specific array. Now, a high-resolution 3D map of forces can be produced over the entire surface, but the whole process requires hours to days for the measurement and needs to uniform imaging environment maintained in order to avoid any instrument drift.

A significant development in force spectroscopy occurred with an approach by Sahin *et al.* [14] that allows simultaneous acquisition of topography and tip-sample force curves throughout the surface with a single scan. Their approach is based on the method proposed by Stark *et al.* [74], which consists of inverting the spectral response of the AFM cantilever for a range of frequencies from which the tip-sample interaction force can be extracted as a component of the driving force acting on the cantilever. Although this method has been demonstrated experimentally in its original conception for standard rectangular cantilevers, the signal-to-noise ratio of the signals observed in the spectrum can be low, such that its applications can be challenging. To

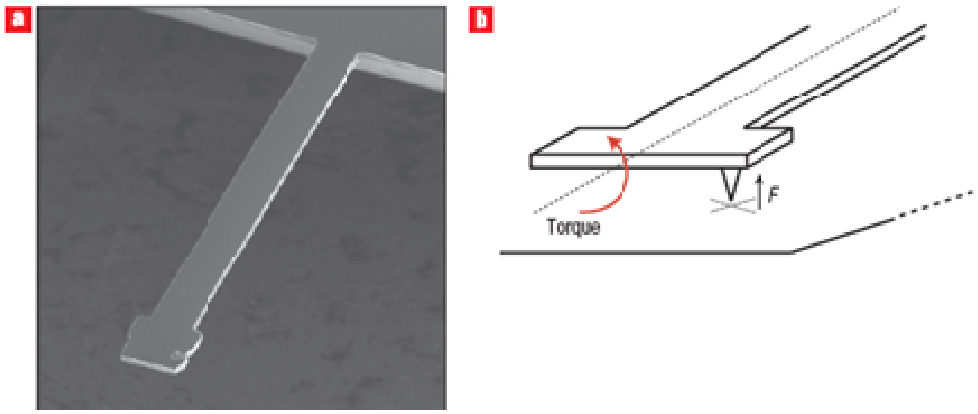

Figure 2-14 *Design of the torsional harmonic cantilever (THC) with an off-axis tip. (a) SEM image of the THC, (b) illustration of THC interacting with the surface [14].*

address this, Sahin *et al.* have used modified T-shaped cantilevers with off-centered tip, the so-called *torsional harmonic cantilevers* (THC), as shown in Figure 2-14. In their method, the flexural vibration is controlled through standard amplitude-modulation AFM (AM-AFM) while passive torsional vibrations are excited by the torque generated through impact between the laterally asymmetric cantilever and the sample, which provides a high signal-to-noise ratio. Since the torsional vibrations of the cantilever behave close to the well-known dynamics of harmonic oscillators, the tip-sample force curve can be extracted from the response of the torsional vibration as a function of the vertical tip position (i.e., as a function of the instantaneous position of the flexural oscillation), as shown in Figure 2-15.

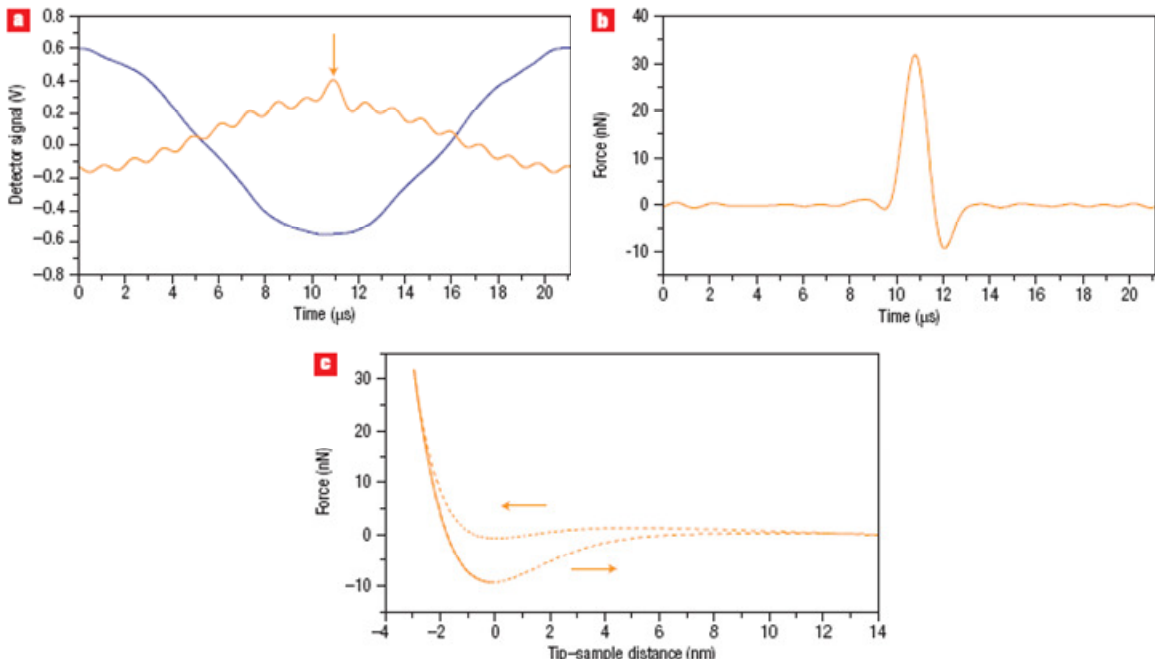

Figure 2-15 *Reconstructing the tip–sample force waveform. (a) Oscilloscope traces of the periodic flexural (blue) and torsional (orange) vibration signals at the position-sensitive detector, obtained on graphite. (b) Time-resolved tip–sample force measurements calculated on graphite. (c) The same data as in (b) plotted against tip–sample distance. Negative distances mean that the sample is indented. Arrows indicate the direction of motion. The solid part of the curve marks the points between the largest sample indentation and breaking of the contact on the retraction portion of the curve [14].*

2.3 Mapping conservative and dissipative tip-sample interactions in dynamic AFM

An important application of dynamic AFM, in addition to probing surface topography and conservative interactions, is the measurement of dissipative tip-sample interactions [15, 16-18, 22]. Dissipation in dynamic AFM represents a cumulative effect of interactions including, but not limited to, long-range

electrostatic, surface adhesion, viscoelasticity and hysteretic inter-atomic losses [19-22]. Typically, in most dynamic AFM methods, the observed variables are influenced by total tip-sample interactions, which are usually a result of both conservative and dissipative effects. Separation of their contributions is important in order to accurately interpret the images.

In conventional AM-AFM operation, by plotting phase shift changes on a sample, an improvement in the response to sharp topographical changes and to the samples with varying composition was obtained. However, due to the commonly observed bistable behavior in AM-AFM, understanding the origin of the contrast was difficult. The specific sample properties affecting the phase contrast were not clear. The early simulations performed by Tamayo and Garcia [23] to study the influence of elastic sample properties explained that in the absence of inelastic interactions, phase shifts are independent of the value of the elastic modulus of the surface. They showed that the effect of elasticity variations reflected in the phase shifts only if these variations were associated with some dissipative phenomenon on the surface. They used a non-linear driven model with damping to simulate the cantilever behavior. The short-range attractive interactions were represented by the van der Waals model, whereas Hertz's model was used for the repulsive contact forces. In their study, the motion was simulated under two types of dissipative effects on the surface, viscous damping and adhesion energy hysteresis. Figure 2-16 shows the phase shift calculated as a function of the elastic modulus for three cases, (1) only elastic interactions, (2) including viscoelastic interactions, and (3) including adhesion energy hysteresis. It can clearly be seen that the phase shift is insensitive to the large range of elastic

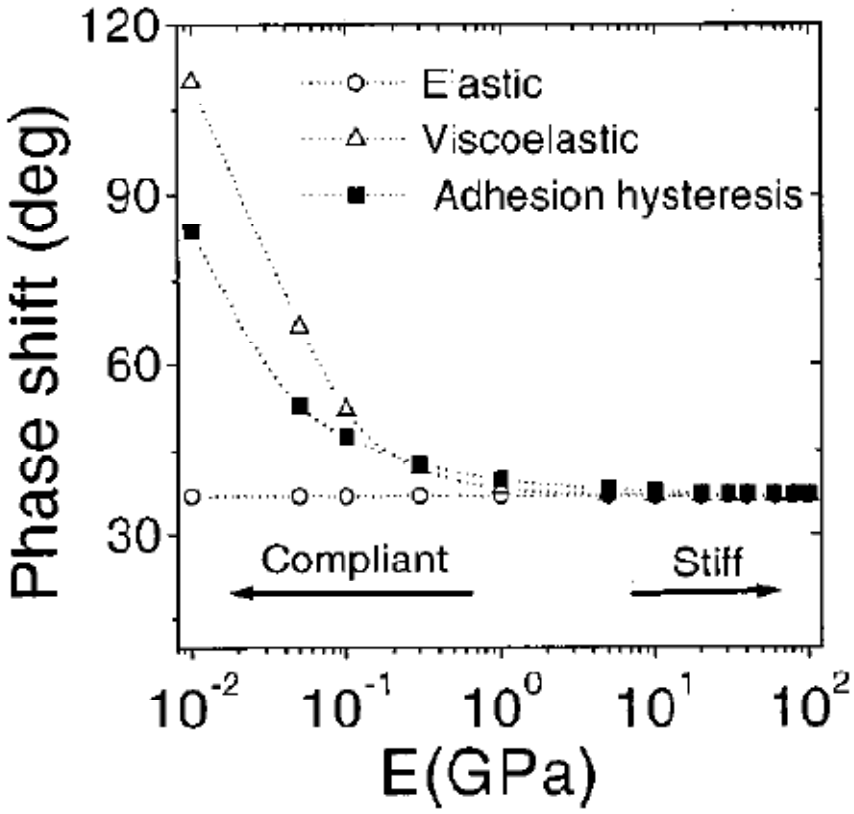

Figure 2-16 *Theoretical phase shift dependence on elastic properties for several tip–sample interactions. Elastic (circles); with viscous damping η=30Pa.s (triangles); with adhesion energy hysteresis, γ_A=10 mJ/m^2, γ_R=60 mJ/m^2 (squares) [23].*

modulus (most materials fall in this range) in the absence of dissipative processes. This is explained with the fact that in AM-AFM mode, the amplitude during imaging is maintained at a setpoint value, which compensates the effect of change in elastic modulus on the phase shift. They also verified these observations by performing experiments on two materials with different surface properties.

To study the role of dissipation further, Garcia *et al.* [16] and Cleveland *et al.* [15] developed the correlations for phase shifts in terms of energy dissipated on the surface. The energy analysis is based on the principle that in steady state the energy supplied to the cantilever should be lost due to hydrodynamic viscous damping and

due to the tip-sample inelastic interactions. Using this, the average power dissipated by the tip in AM-AFM mode could be calculated as,

$$P_{tip} = \frac{1}{2}\frac{kA^2\omega_o}{Q}\left[\frac{A_o}{A}sin\varphi - 1\right] \quad (2.9)$$

where k is the cantilever stiffness, A the oscillation amplitude, Q the quality factor, ω_o the free angular resonance frequency, A_o the free oscillation amplitude and φ is the phase shift. The assumptions for the derivation are sinusoidal motion of the cantilever in steady state and that the damping coefficient of the cantilever remains unchanged when the tip interacts with the sample.

It can be deduced from equation 2.9 that if the tip loses no energy, amplitude and phase shift are not independent ($\varphi = sin^{-1}(A/A_o)$). Now, since in AM-AFM mode, the oscillation amplitude is kept at a fixed value, the phase will show no variation in the absence of dissipation, which agrees with the simulation results discussed above. However, due to the bistable behavior in AM-AFM, the tip jumps between attractive (phase shift greater than 90^o) and repulsive (phase shift smaller than 90^o) interaction regimes. Therefore, the changes observed in the phase due to such jumps cannot be attributed to the surface dissipation and can result in false interpretation of images. This implies that the tip must be in either the purely attractive or purely repulsive regime in order for the phase to map the dissipative variations. Figure 2-17a and b show the amplitude and phase shift response for a silicon cantilever tapping on a silicon wafer, and c shows the dissipated power calculated using equation 2.9. It is observed that the energy dissipation is nearly constant in the repulsive region, which is due to the fact that the tip penetration into the sample and hence the peak forces are fairly constant after the transition from the attractive to the repulsive forces.

Essentially, this approach provides an easier way to interpret the AM-AFM imaging data.

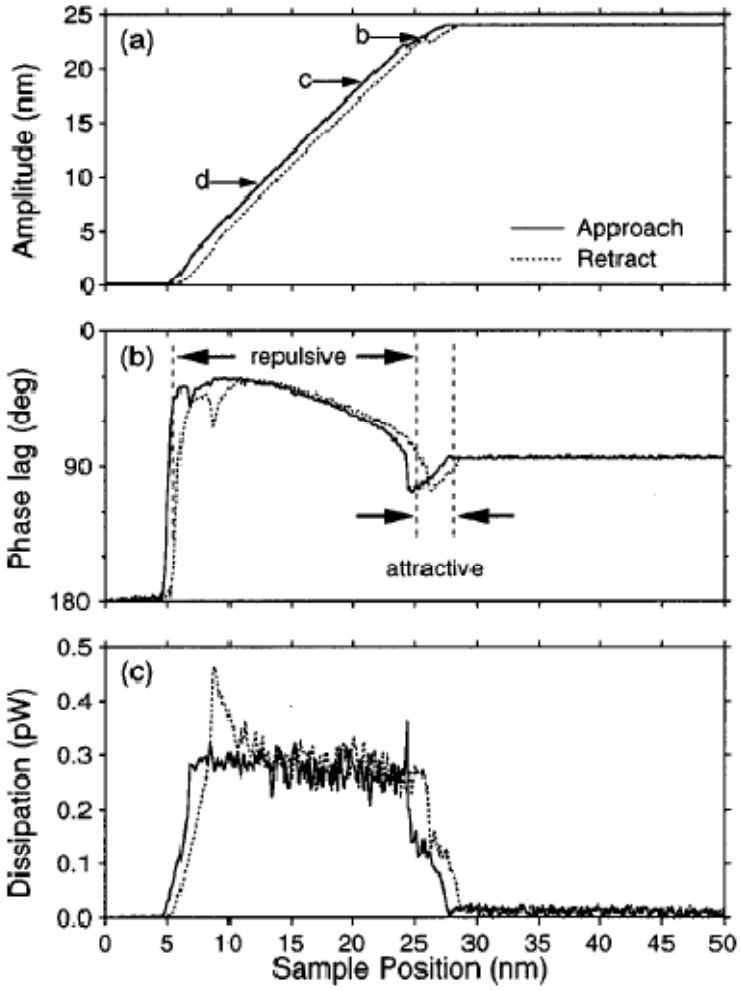

Figure 2-17 *Amplitude (a), phase (b), and power dissipation (c), of the resonating cantilever measured as the sample was approached (solid lines) and retracted (dotted lines). The regions labeled in (b) show where the tip is experiencing overall attractive or repulsive forces [15].*

FM-AFM mode of operation, on the other hand, provides a relatively straightforward way to separate conservative and dissipative contributions on the surface during imaging when operated in constant-amplitude mode [24, 75, 76]. It is

discussed earlier in section 2.1 that there are two common methods to control the cantilever in FM mode, constant-amplitude and constant-excitation (CA-FM and CE-FM), with variable drive and fixed drive, respectively. In the CA-FM mode, when the tip begins to experience the tip-sample interactions, an input gain factor is adjusted so that the response amplitude does not decrease as a result. Hölscher *et al.* have analyzed the motion of a cantilever in this mode and derived the expressions for frequency shift and gain factor in terms of the tip-sample interactions and operation parameters [24]:

$$\Delta f = -\frac{f_o^2}{Ak}\int_0^{1/f_o} F_{ts}[z(t), \dot{z}(t)]\cos(2\pi f_o t)\, dt \tag{2.10a}$$

$$|g| = \frac{1}{Q} + \frac{2f_o}{Ak}\int_0^{1/f_0} F_{ts}[z(t), \dot{z}(t)]\sin(2\pi f_o t)\, dt \tag{2.10b}$$

where f_o is the free resonance frequency, k the cantilever stiffness, A the oscillation amplitude, F_{ts} depends on both the position and velocity of the tip (to include effects of conservative and dissipative interactions), and Q is the quality factor. It can be inferred from the equations that the frequency shift depends only on the average of tip-sample forces and is independent of all the dissipative processes, whereas the gain factor is directly related to dissipation on the surface. They also verified these results through simulations. This is a very useful observation as it makes the interpretation of images obtained in CA-FM much simpler to understand, where the output channels are gain factor and frequency shift. The response in CE-FM mode of operation, however, does not exhibit the same properties. In this case, the drive is kept fixed and the oscillation amplitude is allowed to change due to interaction forces and consequently, the output imaging channels, frequency shift and oscillation amplitude,

are due to the coupled effect of both conservative and dissipative interactions. However, through mathematical analysis and simulations, Hölscher *et al.* [26] have shown that the separation of these interactions is possible even in CE-FM mode, making this method useful where softer mechanical contacts are desired.

For a comparative analysis of the two modes of FM operation, Hölscher and coworkers [25] have performed spectroscopy using both and have shown that the same information about the tip-sample interactions can be obtained in either CE-FM or CA-FM mode. They performed experiments in ultrahigh vacuum using a sharp silicon tip on HOPG sample. The operation parameters were, f_o = 259.542 kHz, k = 16.6 N/m and Q = 29900. The experiments were conducted in CE- and CA-FM mode at the same point on the sample, and corresponding output channels (response amplitude and frequency shift for CE-FM, and drive amplitude and frequency shift

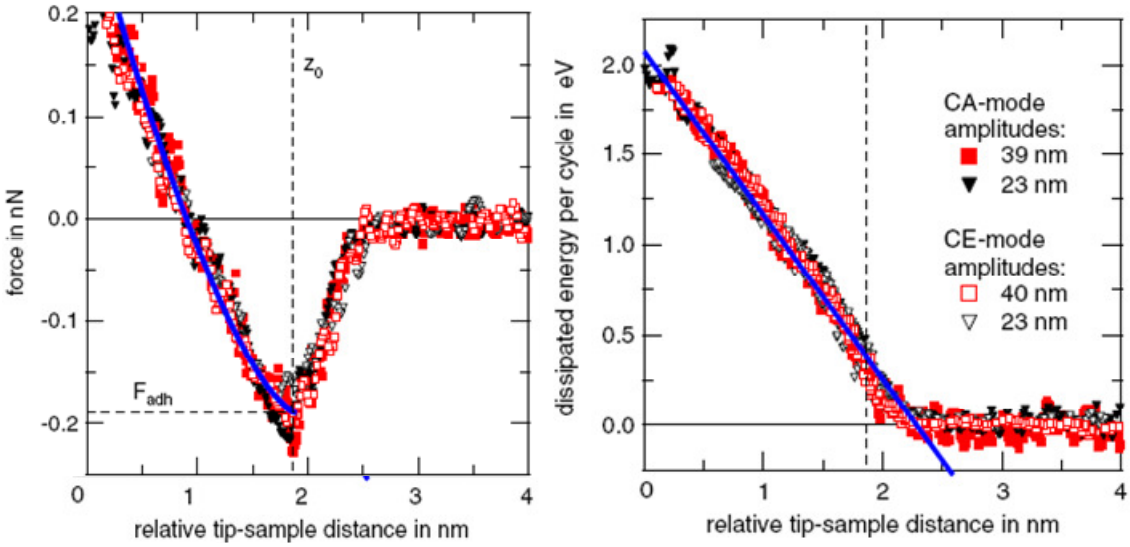

Figure 2-18 *Conservative tip–sample force and dissipated energy per oscillation cycle measured in the CE and CA modes for different oscillation amplitudes. The horizontal dashed line at position z_0 indicates the transition from the non-contact to the contact regime as assumed in the DMT model. The solid lines (blue) represent fits in the contact regime of the tip–sample interactions [25].*

for CA-FM) were measured as a function of z-piezo movement. The free oscillation amplitude for both cases was varied between 23.4 nm and 39.9 nm. Figure 2-18 shows that the conservative tip-sample force curves and dissipation energy plots calculated for the two methods are almost indistinguishable.

Of further interest in this direction is work by Martin *et al.* [75], where they have extracted conservative and dissipative components of tip-sample interactions in AM-AFM mode spectroscopy and compared them to those obtained using CA-FM mode. First, the amplitude and phase curves in AM-AFM mode have been acquired with respect to the cantilever base position above the sample, which are then converted to frequency shift and relative dissipation using the expressions,

$$\Delta f \approx 2f_o \frac{\cos(\varphi) - Qa(1-u^2)}{Qa} \tag{2.11a}$$

$$\frac{\gamma_{tot}}{\gamma_o} = -\frac{\sin(\varphi)}{ua} \tag{2.11b}$$

where f_o is the free resonance frequency, φ the phase shift, Q the quality factor, $u = f_{exc}/f_o$, $a = A/A_o$, f_{exc} the excitation frequency, A the response amplitude, A_o the free resonance amplitude, Δf the frequency shift and γ_{tot}/γ_o the relative dissipation. It shall be noted that the above expressions are obtained with the assumption that no higher harmonics/modes participate in the motion. For the experiments in AM-AFM mode, they first performed a comparison within AM-AFM by exciting the cantilever at two frequencies that are slight below the free resonance frequency. The corresponding amplitude and phase data is used in the above expressions for calculations. The cantilever was then excited in CA-FM mode, where the change in drive amplitude in response to the interactions (measure of relative dissipation) and frequency shift were

recorded. This allowed a direct comparison of similar quantities from two methods. Figure 2-19 shows a comparison of the two curves obtained in AM-AFM and the CA-FM curve for frequency shift and relative dissipation (all at an amplitude of 12.5 nm). A super sharp silicon tip has been used on a sample that is a mixed monolayer of n-octadecyltrichlorosilane and 21-aminohenicosyltrichlorosilane grafted on a silicon wafer. The sample is chosen due to its flatness to facilitate the analysis of the two methods. The cantilever parameters are, f_o = 159.186 kHz and Q = 340. The two excitation frequencies used for AM-AFM mode are, 158.961 kHz and 159.058 kHz. Good agreement can be seen in the data. They also plotted similar curves at an

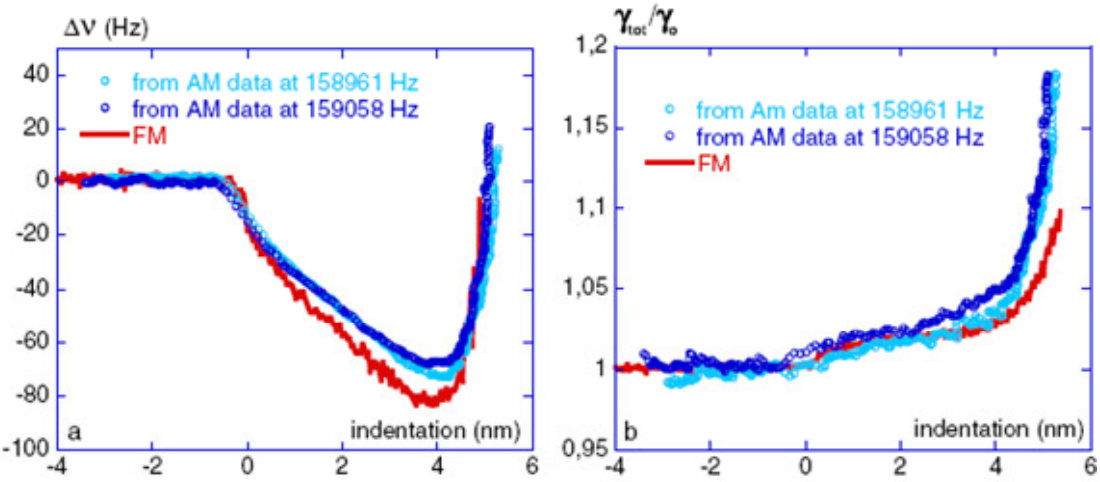

Figure 2-19 *Comparison of conservative components extracted from AM measurements with FM frequency shift (a) and dissipative components extracted from AM measurements with normalized damping signals (b) recorded at an amplitude of 12.5 nm at the same location on the grafted surface [75].*

amplitude of 26 nm, and observed an even better agreement. The important factors in these experiments have been the assumption that the other harmonics are absent and ensuring a very small variation in amplitudes in AM-AFM mode by using a very flat sample. Overall, it shows that AM and FM-AFM are two modes that can probe the same tip-sample interactions.

All the methods discussed above for measuring conservative and dissipative interactions are using the conventional single eigenmode excitation AM- and FM-AFM operations. The limitations of doing so are that the operation at setpoint amplitude in AM-AFM mode constrains the mapping of full range of interactions, and FM-AFM operation is most commonly performed in non-contact mode in vacuum conditions. As discussed in previous sections, multifrequency AFM offers an effective way to improve sensitivity to interactions [4, 27, 28] with the excitation of higher eigenmodes, these methods have been recently studied for mapping conservative and dissipative interactions, as discussed below.

Lozano and Garcia [77, 78] have developed a theory for phase spectroscopy in bimodal AFM, where two eigenmodes are excited at their free resonance frequencies with a fixed drive. With the application of the energy conservation principle, they have derived an analytical relationship between the observables (amplitude and phase) for two eigenmodes and two independent properties of the tip-sample interactions, the dissipated energy (E_{ts}) and the virial (V_{ts}). The virial term is the convolution of interactions with the tip position and carries information on conservative interactions, whereas the dissipated energy is a convolution of interactions with the tip velocity. The derived correlations are,

$$E_{ts}(i) = \frac{\pi k_i A_i}{Q_i}(A_{oi}\sin(\varphi_i) - A_i) \tag{2.12a}$$

$$V_{ts}(i) = -\frac{k_i A_o}{2Q_i} A cos(\varphi_i) \tag{2.12b}$$

where i represents the order of the eigenmode, A is the oscillation amplitude, A_o the free resonance amplitude, φ the phase shift, Q the quality factor and k the eigenmode stiffness. Using these expressions, the observables can be interpreted in terms of the conservative and dissipative tip-sample interactions. They have validated the expressions by comparing them with the simulations, as shown in Figure 2-20. During the bimodal imaging, where the first eigenmode is controlled in AM-AFM mode, its oscillation amplitude does not change, but the higher eigenmode amplitude and phase can be used to separate interaction information into conservative and dissipative channels.

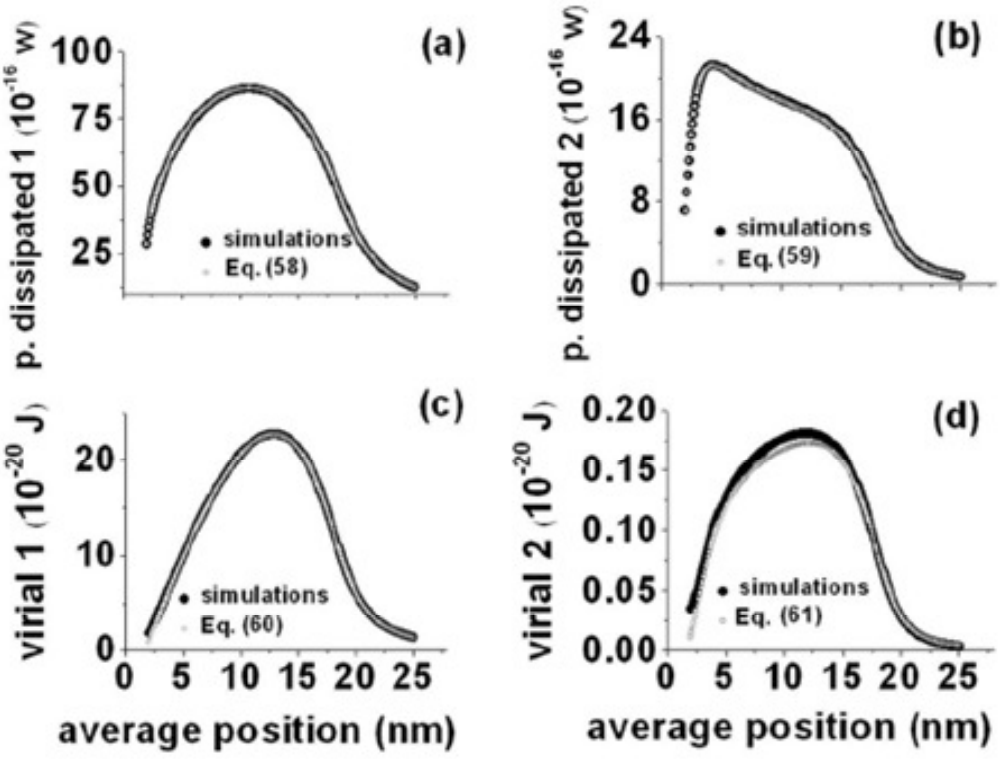

Figure 2-20 *Bimodal AFM operation. Comparison between theory (open dots) and numerical simulations (dark dots) for the virial and the dissipated power. (a) First mode dissipated power; (b) second mode dissipated power; (c) first mode virial; (d) second mode virial [77].*

Another multifrequency approach to map compositional properties of the surface was developed by Naitoh *et al.* [30], in which two eigenmodes of the cantilever were simultaneously excited in the constant amplitude FM-AFM mode in the non-contact operation. The first eigenmode response is used to observe the topography by scanning at a setpoint frequency shift (as is typical in FM-AFM) and the frequency shift of the higher eigenmode is directly related to the conservative tip-sample force gradients (as discussed before for $A_2 << A_1$). They have demonstrated it by mapping the elasticity of a Ge(001) surface with atomic resolution in ultrahigh vacuum. Figure 2-21 shows the simultaneously obtained topography, Δf_2 mapping and Δf_1 mapping of a Ge(001) surface taken at the first mode setpoint frequency shift of -59 Hz with oscillation amplitudes of A_1 = 73 Å and A_2 = 1.3 Å. This presents a useful technique to investigate surface elasticity at the atomic scale.

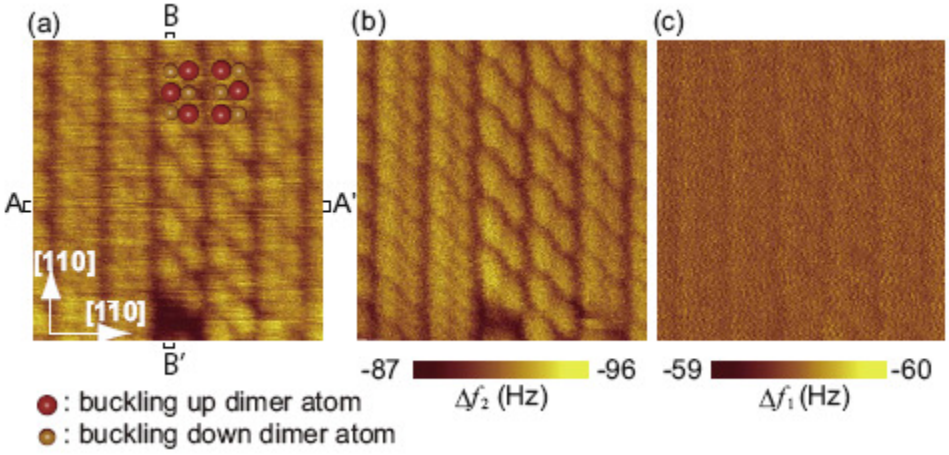

Figure 2-21 *(a) Topographic images of a Ge(001) surface obtained through multifrequency FM-AFM at room temperature maintaining the first mode frequency shift constant at $\Delta f_1 = -60$ Hz with oscillation amplitudes of A_1 =73 Å and A_2=1.3 Å. The scan size is 50x50 Å^2. Simultaneously obtained (b) Δf_2 mapping and (c) Δf_1 mapping of the corresponding Ge(001) surface area [30].*

2.4 Summary

This chapter summarizes the body of work previously conducted by others with respect to

1. Static and dynamic AFM imaging modes of operation
2. Multifrequency excitation of an AFM cantilever for simultaneous acquisition of topographical and compositional information
3. AFM force spectroscopy using static and dynamic modes of operation
4. Mapping of conservative and dissipative tip-sample interactions in dynamic AFM operation

The conventional imaging modes in dynamic AFM have been thoroughly studied and further developed in last 25 years and have also been widely used. A significant leap in dynamic operation occurred with the introduction of bimodal excitation AFM operation in 2004 for surface characterization. However, despite the improvements in imaging demonstrated by bimodal operation and the progress made in its understanding, the multifrequency technique is still not completely explored in its scope and applications. This is partially addressed by this dissertation through the development of new multifrequency imaging methods for acquiring quantitative information about conservative and dissipative interaction forces between the tip and the sample.

Through this literature survey, the current state of atomic force spectroscopy methods has also been thoroughly understood. Despite being one of the most common applications, even after almost 30 years of AFM's invention, there is only

one measurement method by Sahin *et al.* that allows acquisition of force curves in the 3-dimensional space above the surface simultaneously with the topographical imaging. Even this method provides accurate measurements only for soft samples. The other existing techniques are either slow due to selective measurements or require a highly controlled imaging environment for force-curve construction on every pixel of the surface. A novel multifrequency excitation based force spectroscopy method has been presented in this dissertation.

3. Computational development of single-frequency atomic force spectroscopy

In this section, a force measurement method called single-frequency-modulation atomic force spectroscopy is discussed [79], which makes use of the recently proposed frequency and force modulation AFM (FFM-AFM) imaging mode [46]. As briefly stated in the previous section, FFM-AFM mode combines existing knowledge from AM-AFM and FM-AFM to eliminate imaging bistability and to limit the magnitude of the repulsive tip-sample interaction forces. Simulations suggest that this mode of operation is capable of producing high-quality images with reduced sample damage and deformation as compared to conventional tapping-mode AFM. Simulation data obtained using this method was employed to develop a mathematical framework that could be used to extract force curves from the experimental data.

3.1 Simulation approach

The proposed method has been verified using a multi-scale simulation methodology combining atomistic and continuum modeling. This type of approach is necessary because an accurate simulation requires that each component of the system be treated at the length scale that permits acquisition of the relevant information describing its behavior, with the precision that corresponds to its relative importance in governing the response of the instrument. Therefore, since the relevant tip-sample forces for nanoscale tips are typically determined by a small number of atoms, they are most accurately calculated with atomistic techniques such as quantum mechanics

(QM) and molecular dynamics (MD). The cantilever tip motion can be modeled using equations of motion derived through continuum elasticity, and the construction of the

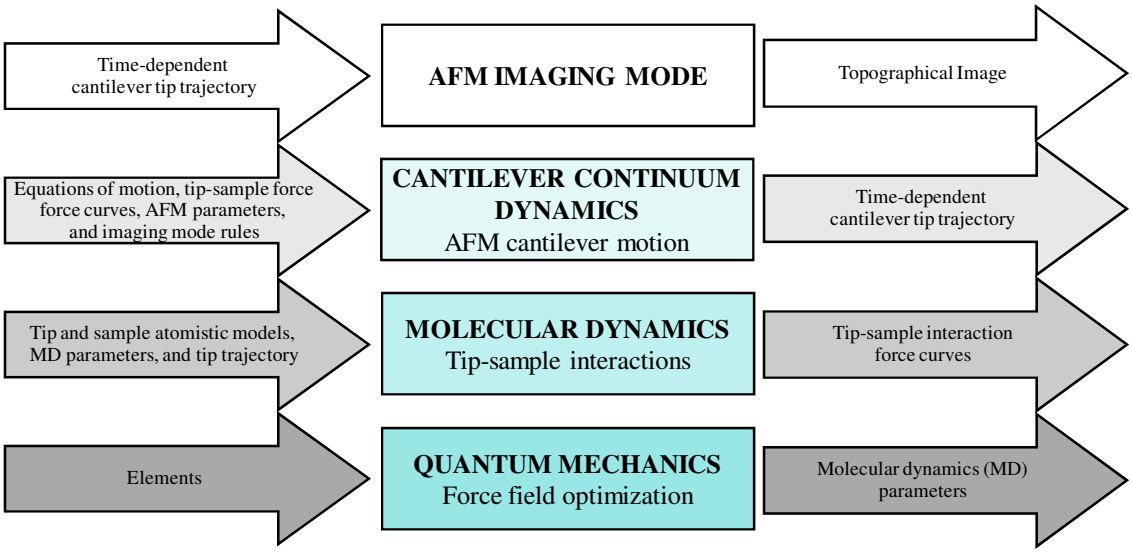

Figure 3-1 *AFM sequential modeling approach using molecular dynamics for constructing the tip-sample interaction force curves.*

image can be performed according to the particular imaging mode in use. Fortunately, the time scales at the different levels of simulation are in many cases such that the calculations can be carried out independently at each level, and then the results fed as input into the next level. This multi-scale computational strategy is illustrated in Figure 3-1 for the case where tip-sample interactions are studied with the molecular dynamics and where QM is used only to optimize the MD parameters (this need not always be the case).

For the numerical simulations, we also have to assume a representative functional form for the tip-sample interaction forces. In this section, the following interaction model has been used for the simulations,

$$F(Z) = \frac{-F_{max}}{1 + 30(Z(t) - Z_{Fmax})^2}; Z(t) \geq Z_{Fmax} \tag{3.1}$$

$$F(Z) = -F_{max} + S(Z(t) - Z_{Fmax})^2; Z(t) < Z_{Fmax}$$

where F_{max} is the maximum attractive tip-sample force on the force curve, Z_{Fmax} the position where F_{max} occurs, and S describes the steepness of the repulsive portion of the curve. $Z(t)$ is the instantaneous relative tip-sample distance. All forces are in nN, all distances are in nm, and S has units of nN/nm^2.

This model has been previously used to fit molecular dynamics force data for a conventional 15-nm-diameter silicon tip tapping on a flat Si(100)-OH surface, a 5.4-nm-diameter single-walled carbon nanotube (constructed based on AFM and TEM experimental data) tapping on the same surface, and a 2.4 nm radius triple-walled carbon nanotube approaching a bacteriorhodopsin molecule. These atomistic models are shown in Figure 3-2 [47, 80] and the force curves are displayed as graphs in Figure 3-3 [47, 80]. In all cases considered, it was assumed that all chemical bonds on the tip and the sample are saturated.

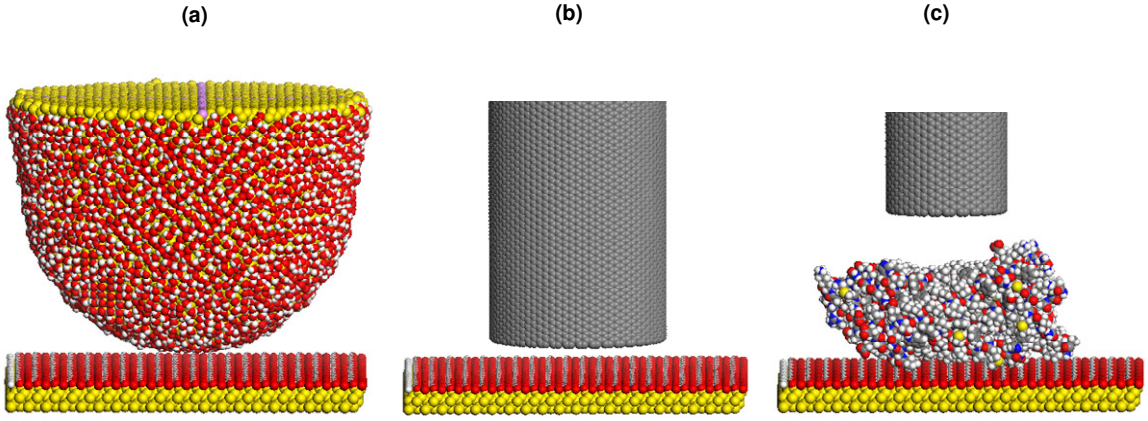

Figure 3-2 *Atomistic models used in the molecular dynamics simulations [47, 80].*

Now, in the remainder of the chapter, the above method is explained starting from the underlying concepts and control scheme used, extending through analytical models and measurement method.

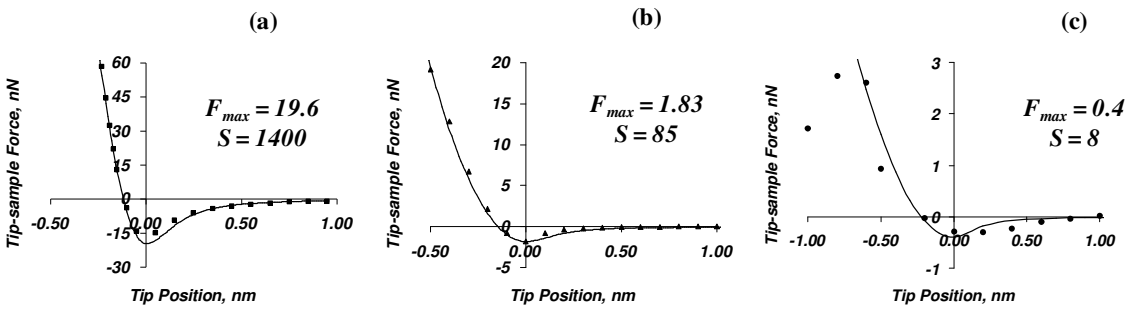

Figure 3-3 *Tip-sample interaction forces for the three cases depicted in figure 3-2. The markers represent the molecular dynamics data and the solid lines show how closely the proposed model matches the data for the corresponding values of* F_{max} *and S [47, 80].*

3.2 Frequency and force modulation (FFM) AFM

As mentioned above, this method uses FFM-AFM mode of operation as the basis for imaging and spectroscopy. FFM-AFM has been discussed in detail in previous publications [46, 47], but briefly, it consists of a tapping mode in which the cantilever is continuously excited at its variable *effective resonant frequency*, similar to the self- excited oscillators used in FM-AFM, to prevent bistability. Additionally, the *effective resonant frequency* is controlled to always remain at the *free resonant frequency* through the modulation of the excitation force amplitude. The control scheme for FFM-AFM is shown in Figure 3-4. Since increases in the effective resonant frequency are caused by the *repulsive* tip-sample interactions, limiting it is equivalent to limiting the magnitude of the repulsive forces. The FFM-AFM

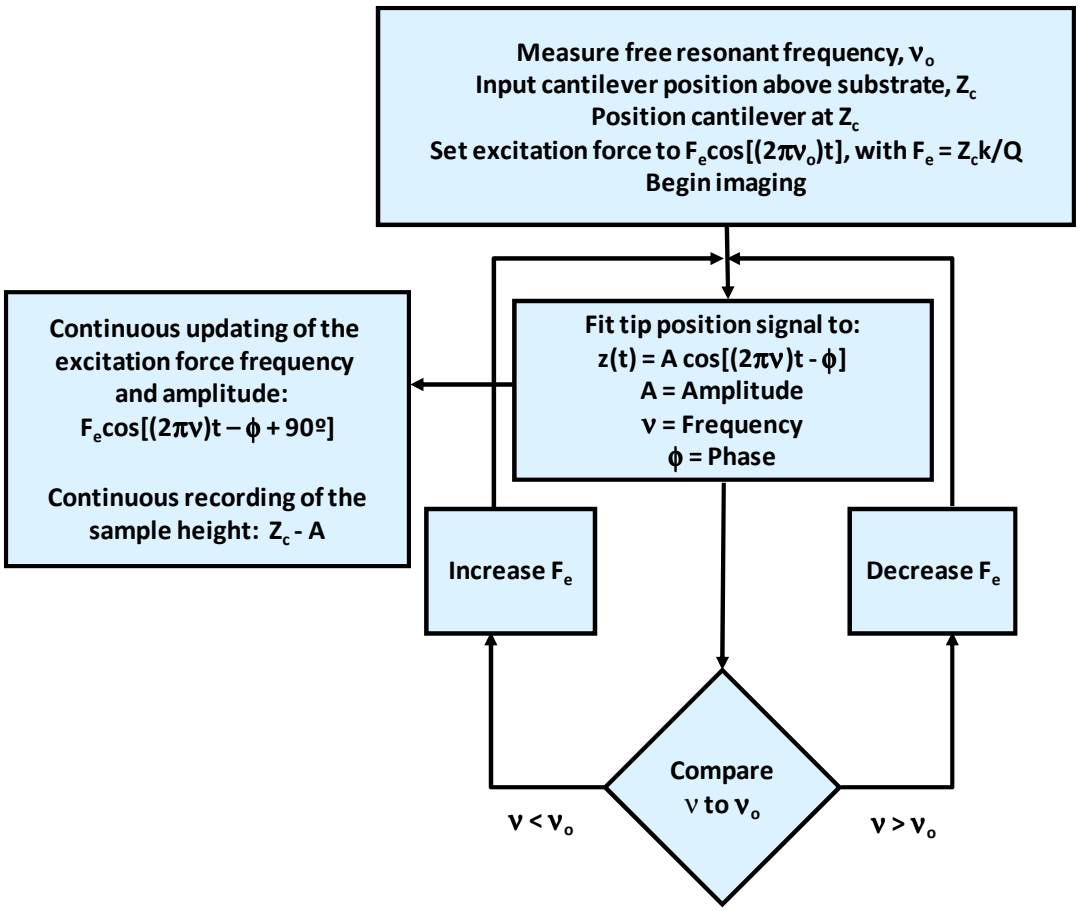

Figure 3-4 *Control scheme for FFM-AFM. The control system obtains the instantaneous frequency, oscillation amplitude, and phase angle from the real-time tip position signal. It continuously adjusts the excitation frequency to match the instantaneous effective frequency and varies the excitation amplitude to ensure that the cantilever is oscillating at the highest possible amplitude while its frequency remains at the free resonant frequency. The sample height is calculated as the fixed cantilever rest position minus the instantaneous oscillation amplitude (i.e., sample height = $Z_c - A$) as the cantilever travels horizontally scanning the sample. Q is the cantilever's quality factor, and k is its force constant.*

algorithm shows that if the effective frequency increases above the free resonant frequency, the controller reduces the amplitude of the excitation force in order to reduce the tip penetration into the repulsive part of the potential. This causes the effective frequency to decrease. If the effective frequency decreases below the free

resonant frequency, the controller increases the amplitude of the excitation force to ensure that the tip reaches the repulsive part of the tip-sample interaction potential, thus increasing the effective resonant frequency. There is also a possibility of controlling the tip penetration into the interaction forces by selecting a set-point frequency different than the free resonant frequency that the controller would maintain during the operation. A setpoint value higher than the free resonant frequency would result in operation in the repulsive regime, whereas a lower setpoint would mean that the tip motion is restricted to the attractive part of the potential.

3.3 Analytical model

The imaging mode being simulated determines the "rules" for controlling the motion of the cantilever, which in turn determines the most appropriate cantilever model to use. The mode of operation being used here can be accurately simulated using the equation of motion of a damped harmonic oscillator because here the cantilever is sinusoidally driven either at its free resonance frequency or very close to it. In such cases, only the fundamental eigenmode of the cantilever is excited significantly, which can be accurately represented by a point mass model [2] as shown in Figure 3-5. The governing equation of motion is the following,

$$m\frac{d^2z(Z_c,t)}{dt^2} = -kz(Z_c,t) - m\frac{\omega_o}{Q}\frac{dz(Z_c,t)}{dt} + F_{ts}(Z) + F(t)\cos[\omega(t)t] \qquad (3.2)$$

where t is time, $z(Z_c,t)$ is the instantaneous tip position with respect to its equilibrium rest position (Z_c), k the harmonic force constant, m the cantilever's effective mass, $\omega_o = 2\pi\nu_o = (k/m)^{1/2}$ the free resonant angular velocity (ν_o is the free resonant frequency), Q the quality factor, $Z(t)$ the instantaneous tip position with respect to the sample,

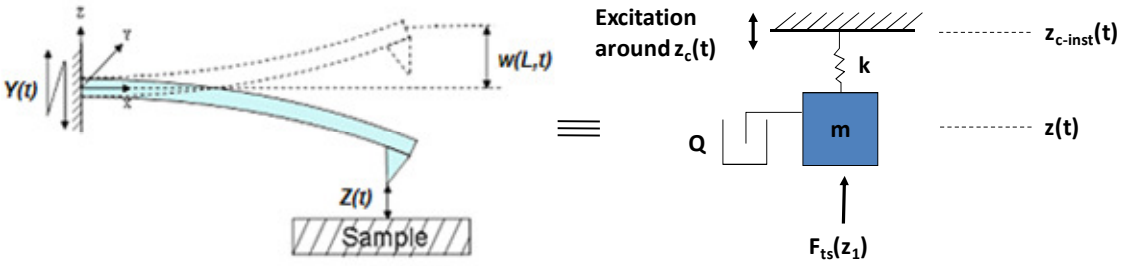

Figure 3-5 *A point mass model representation of a cantilever when only the fundamental mode is excited. $Z_c(t)$ is the instantaneous equilbrium position.*

$F_{ts}(Z)$ the *vertical* component of the tip-sample interaction force as defined in equation 3.1, and $F(t)cos[\omega(t)t]$ the oscillating excitation force applied to the cantilever. The parameters k, v_o and Q are properties of the cantilever and the environment in which characterization is being performed (vacuum, air, or liquid), $F_{ts}(Z)$ is determined by the geometry and physiochemical properties of the tip and the sample, and *excitation force* and Z_c are determined by the imaging mode selected. $z(Z_c,t)$ is of course constantly updated as the tip oscillates at an amplitude over the sample.

3.4 Method

In the single-frequency-modulation spectroscopy method, we derive a relationship between the frequency shift and the cantilever oscillation amplitude, for different values of F_{max} and S. For a starting value of S and F_{max} (see table 1 for a list of parameters used), simulations were run sweeping the setpoint frequency from 350 to 351 kHz for the cantilever in use in small steps while the excitation frequency was modulated in FFM-AFM such that the operation was maintained at effective

resonance (note that this differs from the original FFM-AFM method in that here the frequency shift is not always set to zero). From the output data, the oscillation amplitude *towards the sample* was acquired for all the frequency shifts. Then we gradually changed the values of S and F_{max} until we covered the range specified in table 1.

Table 1 Cantilever and operation parameters

Parameter	**Value/Range**
Force constant, N/m	40
Quality Factor	400
Free resonant frequency, kHz	350
Frequency shift range, kHz	0-1
Cantilever rest position (nm)	15-35
S	0-100
F_{max}	0-2

These amplitude values were plotted against the frequency shift for different S and F_{max} values to observe the variation of amplitude with these parameters. Consecutively, through a rigorous regression analysis of the data, an analytical model was developed relating the cantilever oscillation amplitude to the frequency shift, S and F_{max} as follows,

$$\Delta A(\nu) = A(\nu) - A(\nu_0) = -(\alpha(\nu - \nu_0)^{0.46} + 0.637)S^{-0.415} + 1.406\frac{{F_{max}}^{0.27}}{S^{0.451}} \quad (3.3)$$

where, $\alpha = 0.97(|A(\nu_0)| - 4.85)^{0.55}$, $A(\nu)$ is the oscillation amplitude *towards the surface* at any frequency ν and $A(\nu_0)$ is the oscillation amplitude *towards the surface* at the free resonant frequency of the cantilever ν_0, i.e., at zero frequency shift.

The formula above is straightforward to apply. The user has to perform an FFM-AFM raster scan of the entire surface at three frequency shifts: 0, $\Delta\nu_1$ and $\Delta\nu_2$ and record the values of corresponding oscillation amplitudes *towards the surface* –

$A(v_0)$, $A(v_1)$ and $A(v_2)$ – at each surface point. Using these values and the equation above, S can be calculated as:

$$S = \left(\frac{-\alpha(\Delta v_2^{0.46} - \Delta v_1^{0.46})}{\Delta A(v_2) - \Delta A(v_1)} \right)^{1/0.415} \tag{3.4}$$

The above calculated value can be used to find the maximum attractive force, F_{max} using equation 3.3 and these values can then be used to generate the force field above any surface point by using the tip-sample model shown in equation 3.1. The accuracy and applicability of the method are demonstrated in the results section with examples.

For this method, frequencies v_1 and v_2 should be chosen such that the frequency shift remains between 0.02 to 1 kHz for *soft* samples (such as proteins) and between 0.15 to 1 kHz for samples with *moderate to high* hardness (such as metals and semiconductors). A frequency shift range of 0.2 to 1 kHz is recommended for best results in all cases. The careful selection of frequency shifts is required because very soft samples such as proteins cannot withstand the forces that correspond to frequency shifts beyond 0.05 kHz with an equilibrium tip-sample separation of 25 nm. Hard samples such as Si-OH, on the other hand, can be safely imaged up to frequency shifts of 1 kHz for the same tip-sample separation. The recommended range for the cantilever rest position is between 20nm to 30nm. The model above inherently compensates for an error of +/-5 nm in the adjustment of the cantilever rest position above the sample. The analytical expression above in equation 3.3 is applicable for the tips shown in Figure 3-2b and c, and for cantilevers with the properties listed in table 1. However, it is possible to derive an expression for different tips or cantilevers by following the same approach as above.

3.5 Results and discussion

Figure 3-6 shows results of characterizing a Si(100)-OH surface with a 5.4-nm-diameter single-walled carbon nanotube probe. The force curve obtained by molecular dynamics has been compared with the one obtained using the method explained in section 3.4 and the plots show that they are very close to one another.

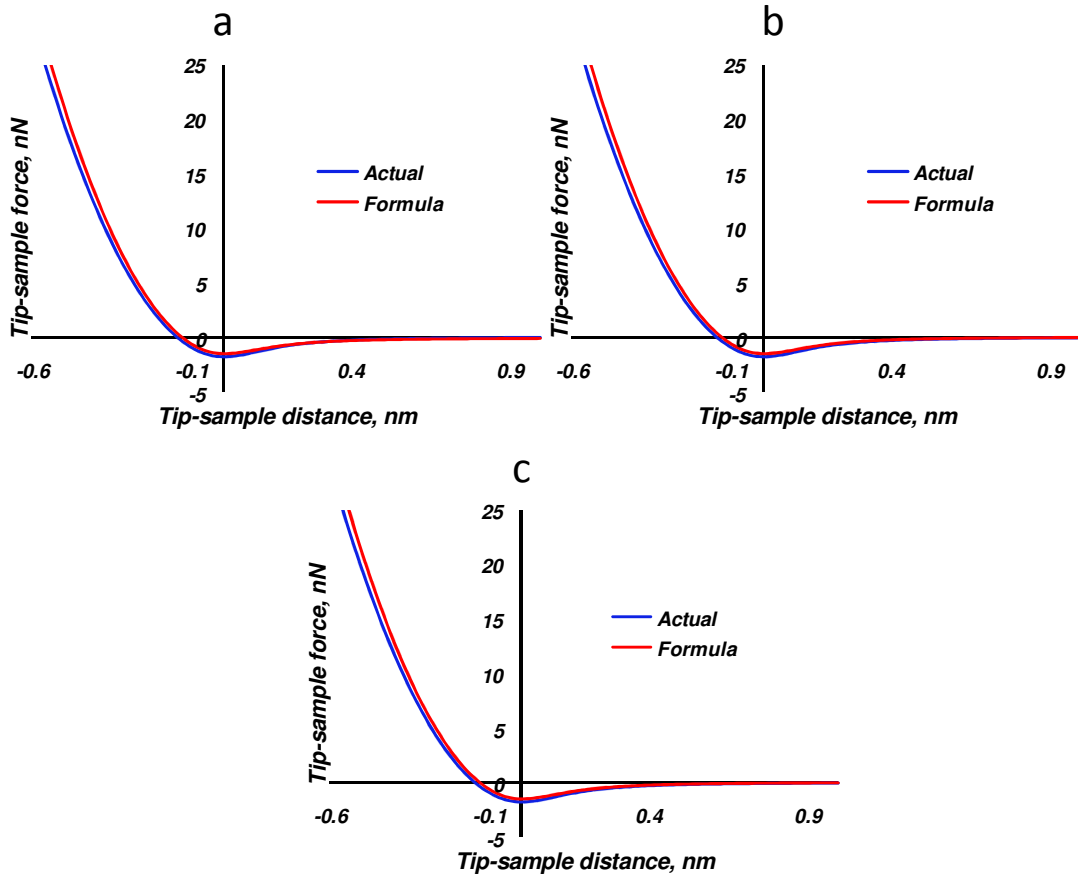

Figure 3-6 *Comparison of force curves obtained by molecular dynamics simulations and from amplitude data by simulating the FFM-AFM operation for a 5.4-nm-diameter single-walled carbon nanotube tapping on a Si(100)-OH surface. The equilibrium distance between tip and sample is 20nm, 25nm and 30 nm, respectively, for cases a, b and c.*

Another comparison is shown in Figure 3-7 between the interaction force curves for a bacteriorhodopsin molecule imaged using a 2.4-nm-diameter triple-walled carbon nanotube, obtained from molecular dynamics and the proposed method. The frequency shifts chosen in this case were 0, 20 and 50 Hz. Again, the curves are almost indistinguishable.

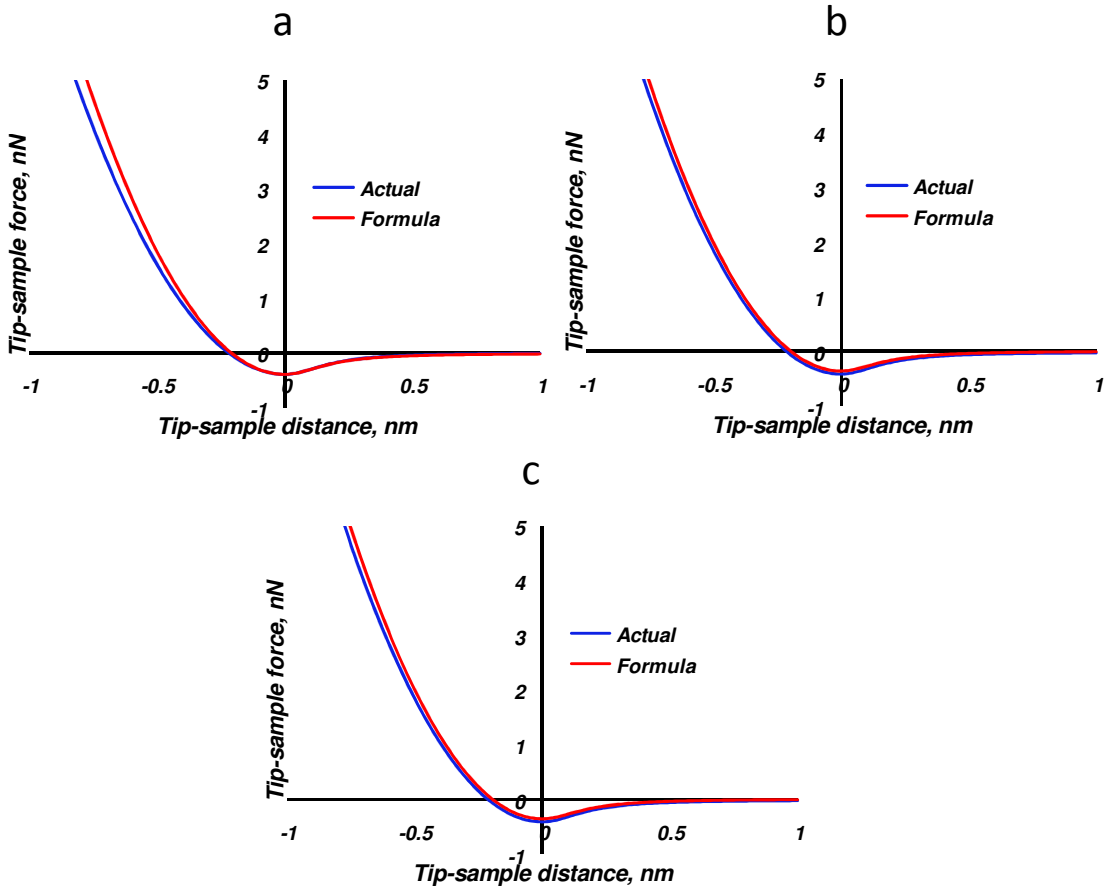

Figure 3-7 *Comparison of force curves obtained by molecular dynamics simulations and from amplitude data by simulating the FFM-AFM operation for a 2.4-nm-diameter triple-walled carbon nanotube tapping on a bacteriorhodopsin molecule. The equilibrium distance between tip and sample is 20nm, 25nm and 30 nm, respectively, for the cases a, b and c.*

Using the values obtained for F_{max} and S, from equations 3.3 and 3.4, it is also possible to develop a regression model to estimate the maximum repulsive force and tip penetration into the sample at any chosen value of the frequency shift in FFM-AFM. Following model was developed for the tip-penetration as a function of the maximum attractive force and the repulsive regime steepness:

$$Z_{min}(\nu, F_{max}, S) = \Delta A(\nu) - 1.4F_{max}^{0.448}S^{-0.46} \tag{3.5}$$

where $\Delta A(\nu) = A(\nu) - A(\nu_0)$ and can be obtained from experiment as explained for equation 3.3. One can also find the actual tip-sample gap once $A(\nu)$ and Z_{min} are determined, as follows:

$$Z_{actual} = |A(\nu)| - |Z_{min}(\nu)| \tag{3.6}$$

Now, by substituting the value of tip penetration into the tip-sample interaction force model (equation 3.1), the maximum repulsive force experienced for a given value of F_{max} and S can be calculated.

Despite the promising results observed by the use of this method, the model is limited to only a given type of cantilever with the parameters shown in table 1. Within the scope of these parameters, we noticed that a variation of +/- 10% in the values of parameters shown in table 1 (Q, k, ν_o) will keep the force curve error within 5%. Also, selection of a different interaction force model that has a larger number of independent parameters instead of the one used here with two parameters to fit the molecular dynamics simulations data can reduce the error. This exercise, however, would make the regression approach very complex.

Despite demonstrating the capability to measure the tip-sample force curves over a wide range of parameters, the analytical expressions in this approach have been derived using the values of observables obtained by simulating the imaging operation under a predefined type of tip-sample interactions and set of control rules. The force model used for simulations may not be representative of all the forces that the tip experiences during actual experiments and hence, it might result in deviations in the measured force curves using this method. In the next section, a robust bimodal excitation spectroscopy approach has been discussed, which is not specific to type of interactions and is applicable to any type of tip and sample combinations.

4. Development of bimodal AFM imaging and spectroscopy methods

In this section, the applications of driving and controlling a higher cantilever eigenmode in addition to the fundamental eigenmode are explored through numerical simulations and experiments for tip-sample force spectroscopy and for obtaining compositional contrast on the sample. In the first section, it is shown computationally that frequency-modulated control of a higher eigenmode enables rapid reconstruction of the tip-sample interaction forces in the 3-dimensional space above the sample. This is followed by the development of an experimental setup and progress towards the implementation of this method. Finally, the applications of various higher eigenmode control methods in mapping conservative and dissipative processes on the surface in bimodal AFM imaging experiments are presented.

4.1 Computational development of dual-frequency-modulation atomic force spectroscopy method

We have already reported on theoretical simulations of a new approach called dual-frequency-modulation (dual-FM) atomic force spectroscopy, based on FM-AFM and bimodal excitation, to simultaneously acquire the tip-sample force curves and topography [79, 81-83]. We simulated this method by exciting two flexural modes of an AFM cantilever, and also with a *dual-cantilever* system consisting of two cantilevers in series. In contrast to the work of Sahin *et al.* [14] (discussed in chapter 2), our concept is based on the active, frequency-modulated control of the oscillations

at two frequencies, such that the response of the signal from which the tip-sample force is calculated is not dependent on tip-sample impact alone. The frequency and amplitude of the low-frequency oscillation are modulated in order to control the level of tip penetration into the tip-sample interaction potential, and the shift in the frequency of the high-frequency oscillation is recorded to calculate the tip-sample force gradient as the tip explores the three-dimensional space above the sample.

Although the single-frequency spectroscopy method presented in chapter 3 is capable of acquiring the force curves from AFM imaging scans, it lacks the robustness and wide applicability that we intended to have in a spectroscopy method. As will be discussed, the dual-FM approach provides a more versatile methodology with the use of fundamental principles of AFM excitation and control. This method can enable the measurement of tip-sample forces for the entire *volume* above the selected microscale surface area with a single scan and without making any assumptions about the force curve's functional form. For a typical cantilever beam sensor, the fundamental eigenmode oscillation performs the conventional imaging operation to obtain topography by intermittently contacting the surface, while the

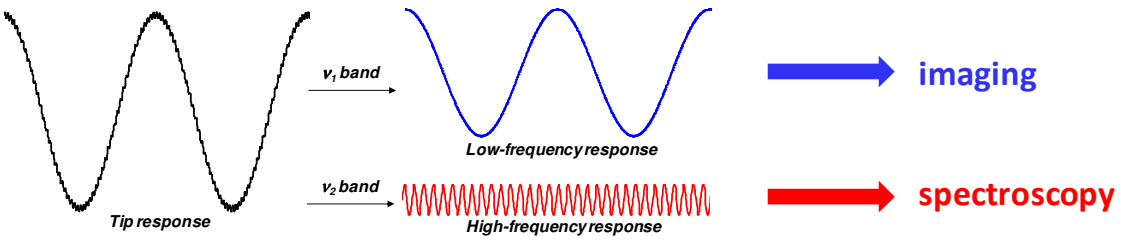

Figure 4-1 *Dual-frequency spectroscopy principle. Schematic of the combined response of the two oscillations (left) and filtered low- and high-frequency responses (right).*

higher eigenmode frequency shift is converted to the tip-sample forces for vertical tip position above the sample obtained from the fundamental eigenmode motion. The basic idea behind this method is illustrated in Figure 4-1.

4.1.1 Measurement technique

We have used two different physical models to achieve the desired dual oscillation response: a) a dual-cantilever system with two cantilevers in series, and b) two flexural modes of a single cantilever. Development of analytical models for both of these designs is explained in the next section. The underlying measurement technique and simulation approach, however, are same in both the cases, which are explained below.

For either of the physical systems, two cantilevers in series or two eigenmodes of a cantilever, excitation is provided such that the low-frequency motion has an amplitude of several nanometers and causes the probe to intermittently contact the sample, while the high-frequency response has a much smaller amplitude ($A_2 << A_1$). Tip vibration is accomplished through the imposition of a compound sinusoidal boundary condition (equation 4.1) at the base of the cantilever or the ensemble of two cantilevers,

$$Y(t) = y_1(t)\cos\left[2\pi\nu_1(t).t - \varphi_1(t) + \frac{\pi}{2}\right] + y_2\cos\left[2\pi\nu_2(t).t - \varphi_2(t) + \frac{\pi}{2}\right] \quad (4.1)$$

where $Y(t)$ is the *instantaneous* position of the base at time t, $y_1(t)$ and y_2 are the amplitudes of the low- and high-frequency excitations, respectively (note that y_1 is time-dependent, but y_2 is not), $\nu_1(t)$ and $\nu_2(t)$ are their respective instantaneous

frequencies (after filtering the tip response into a low- and a high-frequency oscillation, as described below), and $\varphi_1(t)$ and $\varphi_2(t)$ are the phases of the respective oscillation responses.

The control scheme is illustrated in Figure 4-2. Initially v_1 and v_2 are set equal to the free resonant frequencies, $v_{1\text{-}o}$ and $v_{2\text{-}o}$, respectively, of large and small cantilevers

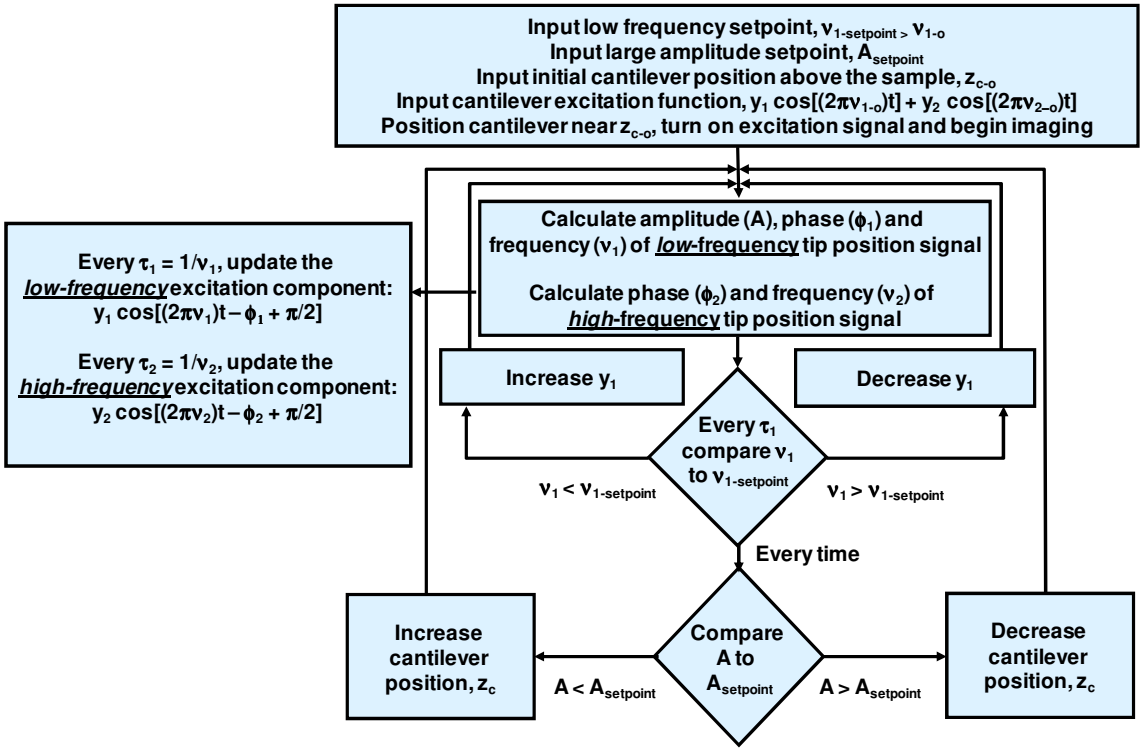

Figure 4-2 *Proposed dual frequency modulation control scheme. Here, $v_{1\text{-}o}$ and $v_{2\text{-}o}$ are the free resonant frequencies of the two oscillations, y_1 and y_2 are the excitation amplitudes at the two frequencies, $v_{1\text{-setpoint}}$ and $A_{1\text{-setpoint}}$ are the frequency and amplitude setpoints for the low-frequency oscillation, φ_1 and φ_2 are the phases of the two frequency responses, A and v_1 are the instantaneous amplitude and frequency, respectively.*

or of the two eigenmodes modes of the cantilever and both phases are set equal to zero. The initial value of y_1 as well as the value of y_2 is provided by the user. Once both cantilevers begin to vibrate, the tip response is composed primarily of two

sinusoidal waves with frequencies close to $\nu_{1\text{-}o}$ and $\nu_{2\text{-}o}$, which can be separated through band-pass filters as illustrated schematically in Figure 4-1, and controlled as described in Figure 4-2.

The *low-frequency* oscillation is controlled through an algorithm similar to the previously reported frequency and amplitude modulation AFM method (FAM-AFM) [48], whereby (1) the cantilever is continuously excited at resonance (i.e., at its effective resonance frequency and with a phase that is $\pi/2$ *ahead* of the response), (2) the excitation amplitude, y_1, is increased or decreased in order to achieve a user-defined frequency setpoint ($\nu_{1\text{-}setpoint}$), which must be greater than $\nu_{1\text{-}o}$, and (3) the average position of the cantilever base, Z_c, is increased or decreased in order to achieve a user-defined amplitude setpoint ($A_{1\text{-}setpoint}$). Larger values of $\nu_{1\text{-}setpoint}$ result in greater tip penetration into the surface, which allow probing of increasingly repulsive tip-sample forces. Control of y_1 is performed through a proportional-integral-derivative (PID) loop, while control of Z_c is performed through a proportional-integral (PI) loop (parameters and equations for both control loops are given in the next section). The topography is given by Z_c as a function of the horizontal position on the surface, similar to AM-AFM. The *high-frequency* response is also controlled to be excited at resonance, although no changes are made to its excitation amplitude, y_2. In this case, the operation at resonance requires that the excitation has the same instantaneous frequency as the tip response, and that its phase be $\pi/2$ ahead of the response.

As the surface is scanned, the instantaneous *effective* resonance frequency of the high-frequency response is recorded as a function of the low-frequency tip position

(that is, the vertical tip position obtained after filtering out the high-frequency oscillation) throughout the sample. This is equivalent to having the tip-sample force gradient as a function of the vertical tip position for each point on the surface because the frequency shift and the tip-sample force gradient are, at a first approximation, related by,

$$\Delta\nu_2 = \nu_2 - \nu_{2-o} = \frac{k_{ts}}{2k_2}\nu_{2-o} \tag{4.2}$$

where $\Delta\nu_2$ is the frequency shift of the high-frequency response, ν_2 its instantaneous resonance frequency, $\nu_{2\text{-}o}$ its free resonance frequency, k_2 its harmonic force constant, and k_{ts} is the tip-sample force gradient. The tip-sample force curve is obtained by simple numerical integration of the data describing the tip-sample force gradient vs. vertical tip position, with the boundary condition that the tip-sample force far away from the sample is zero. The required calculations are simple and could be performed during characterization, so that after the sample has been scanned, the user would have collected the tip-sample interaction force as a function of the three-dimensional tip position.

Due to the constant changes made to y_1 during the force curve acquisition process, the large quality factors associated with vacuum AFM, and the fact that the first cantilever transient times are on the order of $2Q/(2\pi\nu_1)$, the dual-FM method may not be suitable for vacuum operation as presented (unless the sample is very flat and requires only minor adjustments to y_1), but could be adapted if one uses a control scheme in which y_1 is fixed, such as using constant-excitation FM-AFM to control the low-frequency oscillation instead of FAM-AFM. Furthermore, our simulations

indicate that the concept could also work when the fundamental mode is controlled using AM-AFM for quality factors corresponding to ambient air, as long as bistability is avoided through the selection of suitable imaging parameters.

It is also worth mentioning that imposing a dual frequency excitation at the base of the cantilever system is not the only option to excite the tip. One could, for example, apply a low-frequency *boundary condition* to the base while applying a high-frequency oscillatory *force* to a magnetic tip on the other end. This would have the advantage of eliminating the high-amplitude, high-frequency excitation at the base of the imaging sensor (note that the amplitude of the high-frequency excitation must be relatively high if applied at the base in order to get a clear high-frequency response for higher eigenmodes with high stiffness).

4.1.2 Proposed physical models and analytical models

The proposed physical set-up is similar to that of current AFMs, except that modifications in the cantilever and excitation may be required to achieve a dual-frequency response. We have proposed two physical models to do so, which are explained below with the development of their corresponding equations of motion.

4.1.2.1 Dual-cantilever system – a system with two cantilevers in series

Shown in Figure 4-3 is the proposed dual-cantilever system with two cantilevers in series [82]. For the simulation purposes, we assume point-mass behavior for each of the cantilevers. This is reasonable as long as the effective resonance frequency of the small cantilever response is not near one of the eigenfrequencies of the large

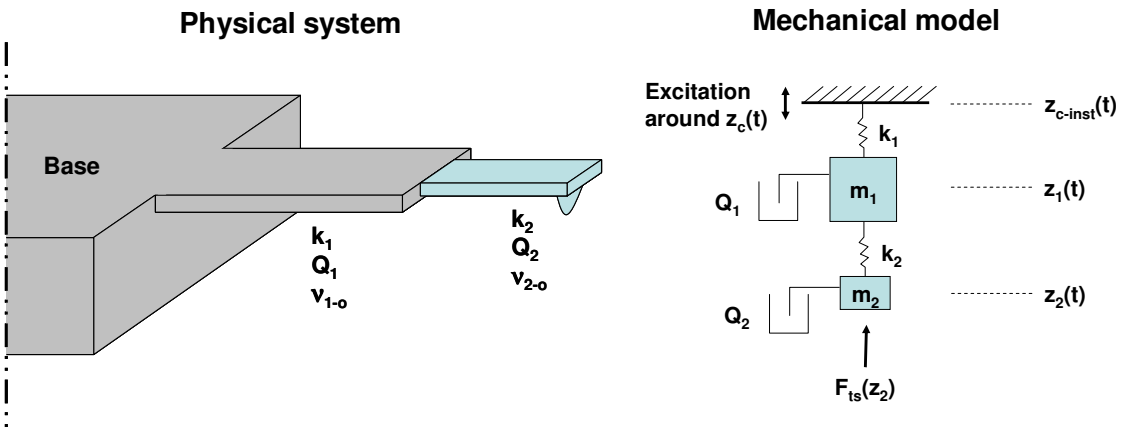

Figure 4-3 *Schematic of the proposed dual cantilever system and associated mechanical model based on point-mass-spring systems.*

cantilever, which could be tested for during manufacturing of the cantilevers. Within the chosen model, the equations of motion for each of the cantilever tips are:

$$m_1 \frac{d^2 z_1(t)}{dt^2} = -k_1[z_1(t) - z_{c-inst}(t)] + k_2[z_2(t) - z_1(t)] - m_1 \frac{2\pi\nu_{1-o}}{Q_1}\frac{dz_1(t)}{dt} \tag{4.3a}$$

$$m_2 \frac{d^2 z_2(t)}{dt^2} = -k_2[z_2(t) - z_1(t)] - m_2 \frac{2\pi\nu_{2-o}}{Q_2}\frac{dz_2(t)}{dt} + F_{ts}[z_2(t)] \tag{4.3b}$$

where m_1 and m_2 are the effective masses of cantilevers 1 and 2 (large and small), respectively, k_1 and k_2 their respective force constants, $z_1(t)$ and $z_2(t)$ their respective instantaneous tip positions, Q_1 and Q_2 their respective quality factors, and $F_{ts}[z_2(t)]$ the tip-sample interaction force experienced by the tip that is attached to the second cantilever, where the probe is located.

Using a system like this allows us to select the parameters such that we can manipulate the fundamental modes of the two cantilevers as desired. The excitation for the smaller cantilever at the end of the ensemble is transmitted through the long

cantilever on which it is attached. We have also explored an alternative design that can be used to effectively achieve the same physical motion and is shown in Figure 4-4. In this system, a paddle is attached at the end of the cantilever through torsional arms, rotation of which (due to the unbalanced mass of the paddle about its axis creating a moment) results in the tip motion at a frequency different from the

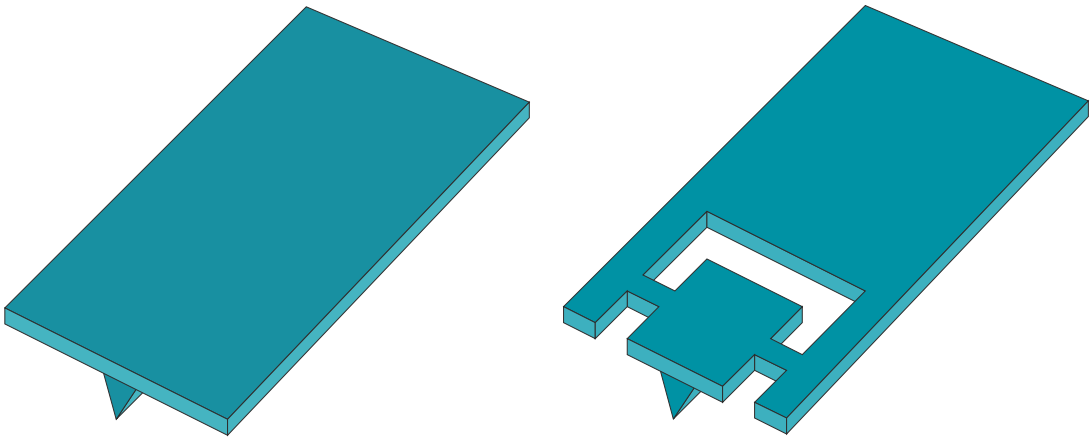

Figure 4-4 *Conventional AFM cantilever (left) and proposed paddle cantilever design (right). Design by Dr. Hendrick Hölscher, Institute for Microstructure Technology, Forschungszentrum Karlsruhe, Germany.*

cantilever's fundamental frequency, resulting in a response composed of two frequencies. Preliminary finite element analysis of test designs has been performed along with the development of analytical expressions to make it possible to choose the dimensions of the arms and the paddle in order to place its natural torsional frequency at a desired value with respect to the cantilever's eigenfrequency. Also, some cantilevers with this design have been manufactured and tested for their viability during imaging. A manufactured prototype is shown below in Figure 4-5. The work on the paddle cantilevers was conducted in collaboration with the *Institute for Microstructure Technology, Forschungszentrum Karlsruhe, Germany*, with Dr.

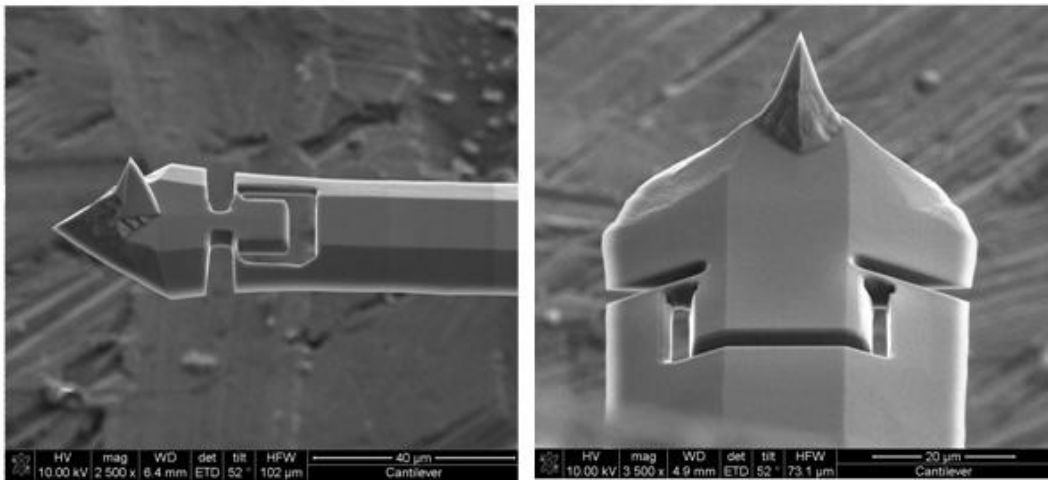

Figure 4-5 *Paddle cut in an AFM cantilever using FIB to test for imaging. FIB by Daniela Exner at the Institute for Microstructure Technology, Forschungszentrum Karlsruhe, Germany.*

Hendrik Hölscher. For the simulations, this system can also be represented as a point-mass ensemble with its corresponding parameters (m, k, Q etc.) in the equation set 4.3. The speculated advantage of this system is that it will be easier to excite the paddle than achieving normal vibrations of the small cantilever in the two-cantilevers-in-series system. A numerical analysis of this system has been presented in the previous publications [84, 85].

4.1.2.2 Using two eigenmodes of a single cantilever

In this case, the desired dual-frequency response is achieved by exciting two eigenmodes of a single cantilever [81] instead of exciting fundamental modes of two cantilevers in series. The low-frequency oscillation is imparted by the fundamental eigenmode and high-frequency motion is achieved by exciting a higher eigenmode. In order to simulate the cantilever dynamics, two coupled eigenmodes of a linear elastic-Bernoulli-Euler-rod model for straight, rectangular cross-sectional microcantilevers

were used, which allowed the treatment of the cantilever as a multiple-degrees-of-freedom (MDOF) system [86-88]. The physical system is shown in the Figure 4-6. Within the model and as required by the measurement technique, tip vibration is accomplished through the imposition of a compound sinusoidal boundary condition at the base of the cantilever as for the dual-cantilever system (equation 4.1). Under the

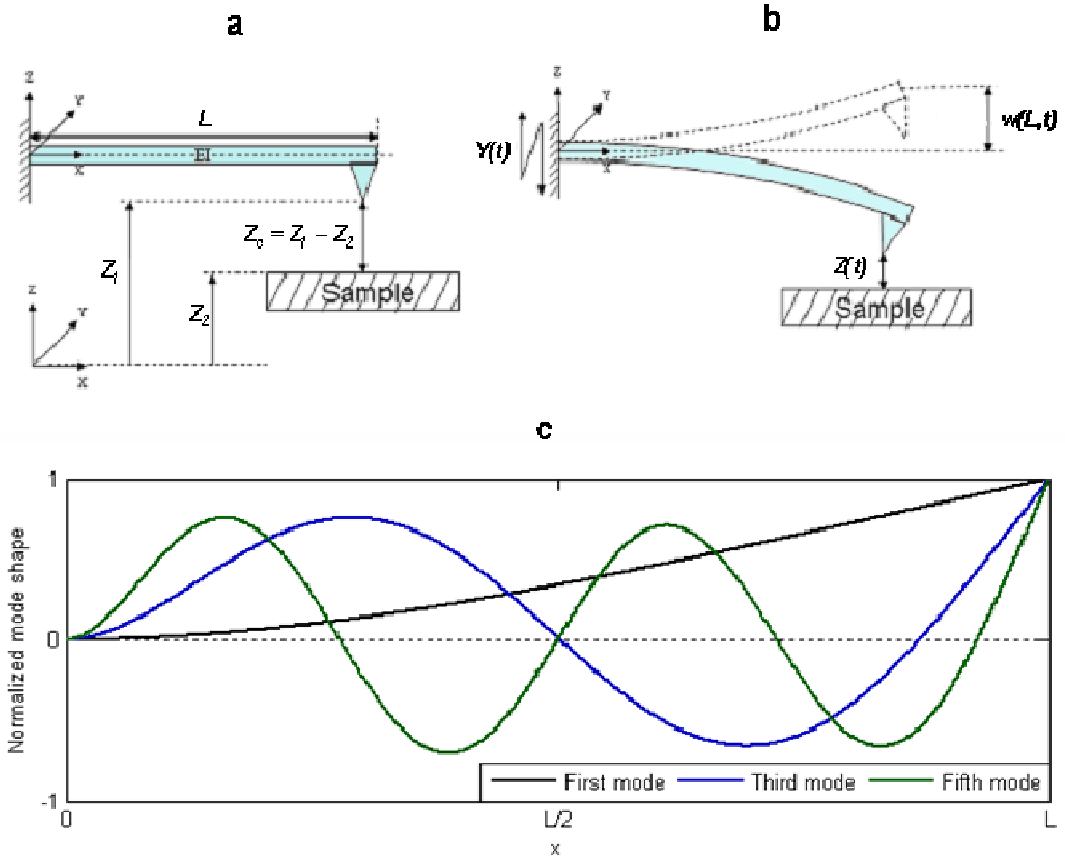

Figure 4-6 *Schematic of the cantilever's initial and intermediate configurations for the fundamental eigenmode vibration (a and b), and cantilever configurations in the first, third and fifth eigenmodes (c).*

influence of tip-sample interaction forces acting at the tip, the governing equation of motion of the microcantilever is given by:

$$\rho A\ddot{u}(x,t) + D\dot{u}(x,t) + (EIu''(x,t))'' = -F(Z_c - u(L,t))\delta(x-L) \qquad (4.4)$$

where ρ, A and L are, respectively, the mass density, cross-section, and length of the beam, EI is its flexural rigidity and Z_c is its rest position above the sample. $u(x,t)$ is its total time-dependent deflection and satisfies the boundary conditions,

$$\begin{aligned} u(0,t) = Y(t) = y_1(t)\cos\left[2\pi\nu_1(t).\,t - \varphi_1(t) + \frac{\pi}{2}\right] \\ + y_2\cos\left[2\pi\nu_2(t).\,t - \varphi_2(t) + \frac{\pi}{2}\right] \\ u'(0,t) = u''(L,t) = u'''(L,t) = 0 \end{aligned} \tag{4.5}$$

We approximate the solution of (4.4) and (4.5) as,

$$u(x,t) = w(x,t) + u(0,t) \tag{4.6}$$

where $w(x,t)$ is the cantilever deflection relative to a non-inertial frame (Figure 4-6b) attached to the moving base and satisfies the boundary conditions,

$$w(0,t) = w'(0,t) = w''(L,t) = w'''(L,t) = 0 \tag{4.7}$$

The discretization of the partial differential equation in equation 4.4 may be suitably achieved through a projection of the dynamics onto the linear modes of the cantilever:

$$w(x,t) = \psi_r(x)w_r(t) \tag{4.8}$$

where $\psi_r(x)$ are orthonormal eigenfunctions of a cantilever freely vibrating away from the surface and can be obtained by solving the following linear eigenvalue problem,

$$\rho A\ddot{w}(x,t) + \left(EIw''(x,t)\right)'' = 0 \tag{4.9}$$

and are given by,

$$\psi_r(x) = (\sin(\beta_r x) - \sinh(\beta_r x)) + \lambda_r(\cos(\beta_r x) - \cosh(\beta_r x)) \tag{4.10}$$

where,

$$\lambda_r = -\frac{\sin(\beta_r L) + \sinh(\beta_r L)}{\cos(\beta_r L) + \cosh(\beta_r L)} \tag{4.11}$$

and β_r are the roots of,

$$\cos(\beta_r L)\cosh(\beta_r L) = -1 \tag{4.12}$$

Substituting (4.6) and (4.8) into (4.4) and integrating over the length of the cantilever, we obtain the equations of motion of the cantilever modes coupled through the non-linear tip-sample interaction force *F(Z)* as,

$$\ddot{w}_r(t) + \delta_r\omega_r\dot{w}_r(t) + \omega_r^2 w_r(t) = \frac{-K_{r-a}}{\rho A}F\big(Z(t)\big)K_{r-b} + \Big[\Big(y_1\Omega_1^2 cos\left(\Omega_1 t - \varphi 1t + \pi 2\right. \\ \left. + y2\Omega 22cos\Omega 2t - \varphi 2t + \pi 2 + \delta r y1\Omega 1\omega r sin\Omega 1t - \varphi 1t + \pi 2 + y2\Omega 2\omega r sin\Omega 2t - \varphi 2t + \pi 2\right. \tag{4.13}$$

where,

$\omega_r = \beta_r^2\sqrt{EI/\rho A}$ gives the natural frequency of r^{th} mode of the cantilever,

$\delta_r = \left(\frac{D}{\rho A\omega_r}\right) = \frac{\omega_1}{\omega_r}1/Q$ are the modal damping coefficients,

$K_{r-a} = \psi_r(L)/\int_0^L \psi_r^2(x)dx = \frac{4}{L\psi_r(L)}$,

$K_{r-b} = \int_0^L \psi_r(x)dx \,/\, \int_0^L \psi_r^2(x)dx$,

$Z(t) = Z_c + Y(t) + w(x,t)$ is the instantaneous tip-sample separation,

and $\Omega_r = 2\pi\nu_r$.

After scaling the time variable as $t \to \omega_1 t$ and letting $\eta_r(t) = w_r(t)\psi_r(L)/Z_c$, we can rewrite equation 4.13 as,

$$\ddot{\eta}_r(t) + \delta_r\frac{\omega_r}{\omega_1}\dot{\eta}_r(t) + \frac{\omega_r^2}{\omega_1^2}\eta_r(t) = \frac{-K_{r-a}}{\rho A\omega_r^2}\frac{\psi_r(L)}{Z_c}F\big(Z(t)\big) + K_{r-b}\psi_r(L)\Big[\Big(\bar{y}_1\bar{\Omega}_1^2 cos\left(\bar{\Omega}_1 t - \right. \\ \left. -\varphi_1(t) + \frac{\pi}{2}\right) + \bar{y}_2\bar{\Omega}_2^2 cos\left(\bar{\Omega}_2 t - \varphi_2(t) + \frac{\pi}{2}\right)\Big) + \delta_r\Big(\bar{y}_1\bar{\Omega}_1\frac{\omega_r}{\omega_1}sin\left(\bar{\Omega}_1 t - \varphi_1(t) + \right. \tag{4.14}$$

$\frac{\pi}{2}\right)+\bar{y}_2\bar{\Omega}_2\frac{\omega_r}{\omega_1}sin\left(\bar{\Omega}_2 t-\varphi_2(t)+\frac{\pi}{2}\right)\Big)\Big]$

where, $\eta_r(t)$ is dimensionless, $\bar{\Omega}_r = \Omega_r/\omega_1$ and $\bar{y}_r = y_r/Z_c$.

4.1.3 Simulation approach

The controls scheme described in Figure 4-2 was implemented within numerical integration of the coupled equations of motion for each mode or each cantilever (equation 4.14 or equation set 4.3, respectively). Control of the effective frequency of the low-frequency vibration, was performed using the following PID equations:

$$\alpha = K_p\left[\nu_1(t) - \nu_{1-setpoint}\right] \tag{4.15a}$$

$$\beta = K_i \sum_{i=1}^{i=10}\left[\nu_1(t - i*\tau_1) - \nu_{1-setpoint}\right] \tag{4.15b}$$

$$\delta = K_d[\nu_1(t) - \nu_1(t-\tau_1)] \tag{4.15c}$$

$$y_1(t) = y_1(t-\tau_1)*(1+\alpha+\beta+\delta) \tag{4.16}$$

where α, β and δ are the proportional, integral, and derivative corrections, respectively, $\tau_1 = 1/\nu_1$ is the instantaneous period of the low-frequency response, and equation 4.16 indicates how the value of $y_1(t)$ was updated after every complete oscillation of the large cantilever. K_p, K_i and K_d are the proportional, integral and derivative gains respectively. Our simulations used K_p between -0.010 and -0.025, K_i between -0.00008 and -0.00025, and K_d between -0.033 and -0.1. All frequencies are in kHz.

Control of the average base position, Z_c, was performed using the following PI equations:

$$\varepsilon = K_p\left[A_1(t) - A_{1-setpoint}\right] \tag{4.17a}$$

$$\rho = K_i \sum_{i=1}^{i=10}\left[A_1(t - i * \tau_1) - A_{1-setpoint}\right] \tag{4.17b}$$

$$Z_c(t) = Z_c(t - \tau_1) + \varepsilon + \rho \tag{4.18}$$

where ε and ρ are the proportional and integral corrections, respectively, and equation 4.18 indicates how the value of Z_c was updated after every complete oscillation of the cantilever. K_p and K_i are proportional and integral gains, respectively, corresponding to amplitude correction. Our simulations used K_p between -0.0008 and -0.0025, and K_i between -0.00008 and -0.00025.

In using the tip-sample interaction force model discussed in chapter 3 (equation 3.1), it was assumed that all chemical bonds on tip and sample are saturated (i.e., covalent bond formation and breaking do not take place during tip-sample intermittent contact), that the surfaces are dry (i.e., there are no thin-fluid-film effects such as capillary adhesion) and that the tip and sample are neutral (i.e., no net long-range electrostatic forces are active).

Tables 2 and 3 provide a list of parameters used in successful simulations for which the results have been presented, while using a two-cantilever system and two modes of a cantilever, respectively. The cantilever parameters used for the single-cantilever case are same as for commercial AC160TS silicon cantilevers manufactured by Olympus. For most simulations, the cantilever was set into oscillation using the controls scheme described above and the different variables were recorded and analyzed when the oscillation reached steady state on the flat surface. The tip-sample force gradients and forces were then calculated, and the force curves

were compared to those given by the actual force curves described by the equation set 3.1. Additionally, to illustrate the simultaneous collection of force curves and topography, a simulation was performed using previously reported methods for the case of a 1.5-nm-diameter double-walled carbon nanotube tip imaging a square, 5.5-nm-wide, 1.4-nm-deep Si(111)-H surface trench with graphite bottom (see section 4.1.4). Different materials were used for the trench terraces and bottom in order for them to have different force curves. Force curves were collected throughout the scan and compared to the actual curves at various locations. This also included locations near the step edges of the trench, where the tip-sample force curves are discontinuous. A flexible carbon nanotube tip was chosen for this simulation instead of a more rigid conventional tip in order to explore the artifacts caused by the step edges.

Table 2: Parameters used in the numerical simulations for a dual-cantilever system

First cantilever free resonant frequency ($\nu_{1\text{-}o}$), kHz	10
Low-frequency setpoint ($\nu_{1\text{-}setpoint}$), kHz	10.1
First cantilever force constant (k_1), N/m	10-50
First cantilever quality factor (Q_1)	100-200
Second cantilever free resonant frequency ($\nu_{2\text{-}o}$), kHz	500-2000
Second cantilever force constant (k_2), N/m	500-2000
Second cantilever quality factor (Q_2)	500-600
Low frequency amplitude setpoint ($A_{1\text{-}setpoint}$), nm	5 - 30
High frequency amplitude (A_2, not controlled), nm	0.02 – 0.4
Maximum attractive tip-sample force in the force curve (F_{max}), nN	2 - 30
Steepness of the tip-sample force curve (S_{rep}), nN/nm^2	85 - 1000
Initial low-frequency excitation amplitude (y_1, controlled), nm	0.15 – 0.25
High-frequency excitation amplitude (y_2, not controlled), nm	2 - 8
Scan speed, nm/s	5 - 20

Table 3: Parameters used in the numerical simulations with two eigenmodes of a single cantilever

Cantilever thickness, μm	4.6
Cantilever width, μm	50
Cantilever length, μm	160
Quality factor (Q^*)	500
Cantilever material density, kg/m^3	2330
Fundamental frequency, kHz	233
Fundamental-mode stiffness, N/m	45
Frequency ratio – seventh mode to fundamental mode sixth mode to fundamental mode fifth mode to fundamental mode fourth mode to fundamental mode third mode to fundamental mode	118.6 84.9 56.8 34.4 17.6
Cantilever elastic modulus, GPa	150
Fundamental-mode amplitude setpoint ($A_{1\text{-}setpoint}$), nm	5
Second frequency oscillation amplitude, nm	0.05 – 0.2
Maximum attractive tip-sample force in the force curve (F_{max}),	1 – 20
Steepness of the tip-sample force curve (S_{rep}), nN/nm^2	85 – 1000

Most calculations are based on using two cantilevers or two eigenmodes such that the frequency ratio is greater than a hundred, which the results suggest, would provide a suitable output resolution, although other combinations could also be used, as will be discussed in the next section.

4.1.4 Results and discussion

For both the cases, i.e., dual-cantilever and single-cantilever, the behavior of the low-frequency oscillation, including its stability in horizontal scanning, was as expected and has been previously discussed [48, 81, 82]. This oscillation is simply imposed to cause the tip to oscillate in intermittent contact with the sample in a smooth trajectory, without any mechanical bifurcations (e.g., AM-AFM bistability).

Figure 4-7a shows a graph of the *effective frequency* of the high-frequency oscillation with time for a complete oscillation of the low-frequency response, beginning and ending at the high point farthest away from the sample. This response looks similar for both physical systems. The frequency starts out at the unperturbed value, and remains there until the tip begins to experience attractive interactions towards the sample, which causes the frequency to decrease according to equation 2.4

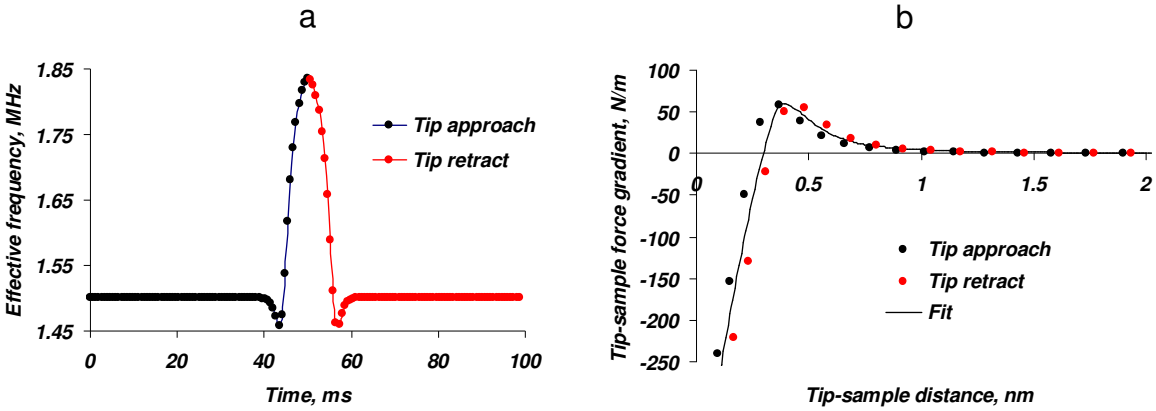

Figure 4-7 *Instantaneous frequency of the high-frequency response as a function of time, for a complete oscillation of the low-frequency response (a) and calculated tip-sample force gradient as a function of the low-frequency response tip position (b), for a silicon tip tapping on a flat Si(100)-OH surface. The results in graph (a) come from the AFM scan, and the results in graph (b) are calculated using equation (2). The simulation parameters were* $\nu_{1\text{-}o}$ *= 10 kHz,* $\nu_{1\text{-}setpoint}$ *= 10.1 kHz,* k_1 *= 50 N/m,* Q_1 *= 100,* $\nu_{2\text{-}o}$ *= 1500 kHz,* k_2 *= 1000 N/m,* Q_2 *= 500,* $A_{1\text{-}setpoint}$ *= 5 nm,* A_2 *= 0.1 nm,* F_{max} *= 20 nN,* S_{rep} *= 1000 nN/nm*^{2}*,* y_1 *(initial) = 0.15 nm,* y_2 *= 4 nm. This type of data could be collected for any other low-frequency oscillation at any horizontal position on the sample as the topographical image is acquired.*

(due to the negative force gradient in the attractive region). After a minimum, the tip begins to experience repulsive interactions (positive force gradient) and the frequency

increases up to the point of maximum tip penetration (i.e., the lowest point in the trajectory of the low-frequency motion), and then follows a behavior during retract that is almost the mirror image of the previous half of the oscillation. Figure 4-7b shows the tip-sample force gradients calculated with equation 4.2 for each frequency data point on the curve of Figure 4-7a as a function of the tip position on the low-frequency oscillation. Although not evident in Figure 4-7a, some hysteresis can be observed in Figure 4-7b, which was attributed to a delay in the response of the system to the rapid changes in the force gradient. Note that the hysteresis in the force gradient data could prevent the accurate acquisition of irreversible force curves (for example, when capillary adhesion is present) because in such cases it would not be obvious to the user to what extent the observed hysteresis corresponds to force curve irreversibility or to method error. Hysteresis can be reduced by using higher ν_2/ν_1 ratio and lower high-frequency oscillation amplitudes, but there could be some practical limitations with regards to the experimental implementation.

For the case of a dual-cantilever system, Figure 4-8a shows the result of numerically integrating the curve of Figure 4-7b for a few different values of $\nu_{2\text{-}o}$ and A_2. The lowest-error curve shown on the graph corresponds to $\nu_{2\text{-}o}$ = 1.5 MHz ($\nu_{2\text{-}o}/\nu_{1\text{-}o}$ = 150) and A_2 = 0.1 nm, which is very close to that obtained for $\nu_{2\text{-}o}$ = 1.0 MHz ($\nu_{2\text{-}o}/\nu_{1\text{-}o}$ = 100) and A_2 = 0.2 nm. In both cases, the measured force curve is in very close agreement with the actual curve. The third curve shows that the quality of the measurement begins to deteriorate for A_2 = 0.4 nm. This is because equation 4.2 is a first order approximation that assumes a constant tip-sample force gradient, which is not the case for larger tip oscillation amplitudes. Other results for $\nu_{2\text{-}o}$ = 2.0 MHz ($\nu_{2\text{-}}$

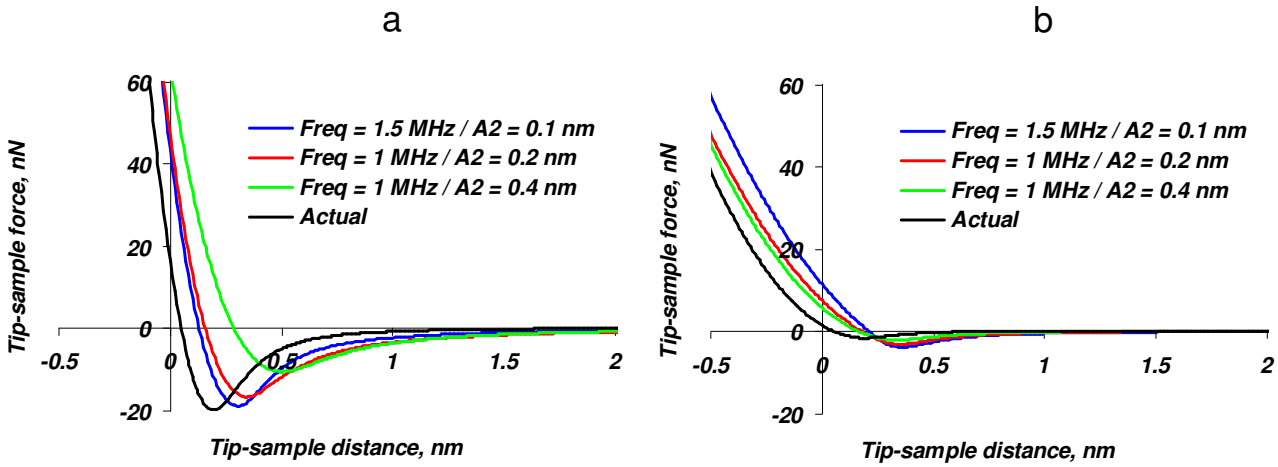

Figure 4-8 *Comparison of the tip-sample force curves acquired within simulations of the new method to the actual force curves for a 15-nm-diameter silicon tip (a) and a 5.4-nm-diameter carbon nanotube tip (b) tapping on flat Si(100)-OH. The curves labeled as "actual" correspond to equation set 3.1 with the appropriate values of* F_{max}, z_{Fmax}, *and* S_{rep} *in each case (given in the text). The blue curve in (a) (closest to the actual curve) is the numerical integral of the data shown in figure 4-7b. The other two curves on the same graph were constructed using the same AFM parameters, except for the indicated values of* $\nu_{2\text{-}o}$ *and* A_2 *(note that different values of* A_2 *also require different values of* y_2*). The curves in (b) were constructed in a similar fashion.*

$_o/\nu_{1\text{-}o}$ = 200) and A_2 = 0.02 nm gave nearly perfect agreement with the actual curve, although such small values of A_2 would be much more difficult to detect experimentally. The results of the less steep force curves of the 5.4-nm carbon nanotube tip tapping on the Si(100)-OH surface (Figure 4-8b) follow a similar trend. The "actual" curve in Figure 4-8a and b corresponds to the equation set 3.1, using the appropriate parameters for each case (that is F_{max} = 19.6 nN, Z_{Fmax} = 0.45 nm, S_{rep} = 1000 nN/nm^2 for the silicon tip, and F_{max} = 1.8 nN, Z_{Fmax}= 0.2 nm, and S_{rep} = 85 nN/nm^2 for the carbon nanotube tip).

For the same tip and sample combinations as in Figure 4-8, i.e., 15-nm-diameter silicon tip and a 5.4-nm-diameter carbon nanotube tip tapping on Si(100)-OH surfaces, respectively, Figure 4-9a and b compare the simulated force curves acquired with single- and dual-cantilever systems. The results are very similar for both approaches. In all cases, the acquired force curve is slightly shifted in the positive tip-

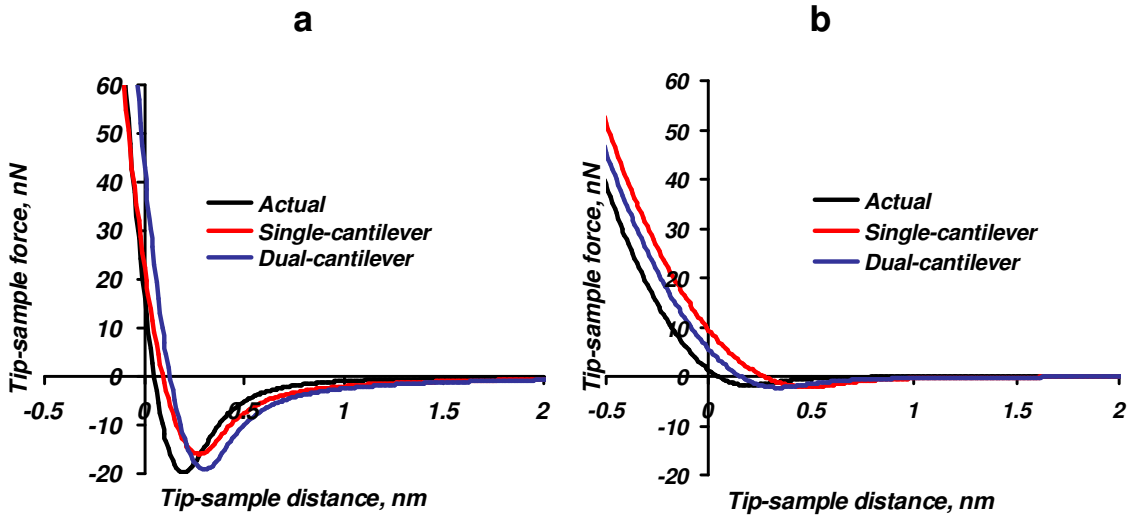

Figure 4-9 *Comparison of the tip-sample force curves acquired within simulations of the dual-FM scheme to the actual force curves for a 15-nm-diameter silicon tip (a) and a 5.4-nm-diameter carbon nanotube tip (b) tapping on flat Si(100)-OH. The curves labeled as "actual" correspond to equation set 3.1 with the appropriate values of F_{max}, Z_{Fmax}, and S_{rep} in each case (given in the text). The relevant eigenmode frequencies and amplitudes for the single cantilever case are the same as for the results of figure 4-4. The dual cantilever results have been previously reported.*

sample distance direction (horizontal axis). This shifting is due to the fact that the tip-sample distance used in plotting the dual-FM curves is the *average* position of the cantilever tip during one full high-frequency oscillation (i.e., the tip position according to the low-frequency oscillation). Since the tip is actually oscillating around this vertical position according to the high-frequency oscillation amplitude, it

is able to sense the tip-sample interactions when the vertical position is higher than one might expect by inspecting the "actual" force curve, which is based on the static tip position (that is, without any oscillation). The high-frequency oscillation is also responsible for the difference in curvature between the dual-FM curves and the actual curves. This is because the high-frequency oscillation allows the tip to probe *a range* of tip-sample distances, which causes the cantilever to sense an *average* force for that range instead of the actual force at the *fixed* tip-sample distance given by the low-frequency response deflection. These effects are magnified when lower frequency ratios or larger amplitudes are used for the high-frequency oscillation.

Figure 4-10 shows the results of the simulated surface scans for velocities between 5 and 20 nm/s. Although the overall topography is reproduced correctly in

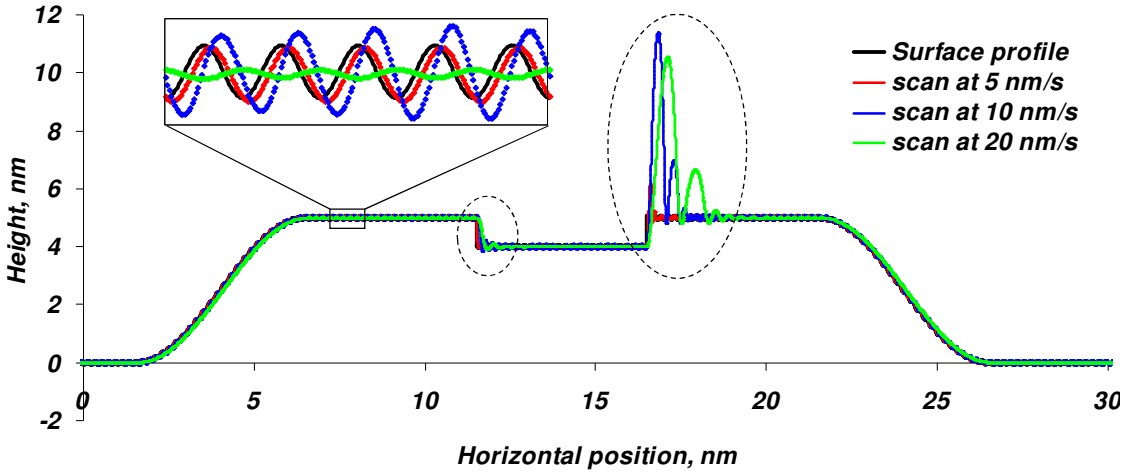

Figure 4-10 *Simulated surface scans for a hypothetical surface containing gentle up- and down-steps with a maximum slope of 2.5, abrupt 1-nm-high up- and down-steps, and atomic-scale oscillations with interatomic spacing of 0.2 nm and atomic-level height oscillations of 0.05 nm. The expanded rectangle shows that the atomic level detail begins to distort at scan velocities of ~10 nm/s and is completely lost at 20 nm/s. The dashed ovals highlight the measurement errors obtained near the abrupt surface steps.*

all cases, except for the disturbances that take place around the abrupt surface steps, the graphs show that the atomic-level oscillations are only accurately measured by the scan taken at 5 nm/s. The atomic height is over-estimated at 10 nm/s, and is completely lost at 20 nm/s. The disturbances are small for all three scan speeds around the down-step but are significant after the up-step, particularly at 10 and 20 nm/s. Since the collection of the tip-sample curves depends on a stable oscillation of the high-frequency oscillation, the results suggest that the method would only be accurate for scan speeds below 5 nm/s for the parameters selected. However, the response time of oscillators excited at resonance is inversely proportional to the frequency, so it should be possible to perform faster scans using cantilevers with higher frequencies. Additionally, since topographical information is lost for approximately 1 nm of horizontal travel after both the down- and up-steps, the method may be restricted to the most regular surfaces when high accuracy is sought.

Figure 4-11 shows the atomistic model and simulation results for characterization of the Si(111)-H/graphite surface trench. The discrepancies between the acquired and actual topography (Figure 4-11b) have been previously discussed [89, 90] and are caused by the non-zero tip diameter and by the tip-sample sliding effects illustrated in Figure 4-12, whereby the tip bends laterally upon contact with the trench terrace, such that it is able to continue traveling towards the bottom. This causes discontinuities in the force curve during the approach and causes the force curve to be different for the approach and retract. Both effects introduce dissipation into the system. The agreement between the dual-FM and actual force curves is similar to the results of Figure 4-9 when the tip is imaging the flat Si(111)-H or

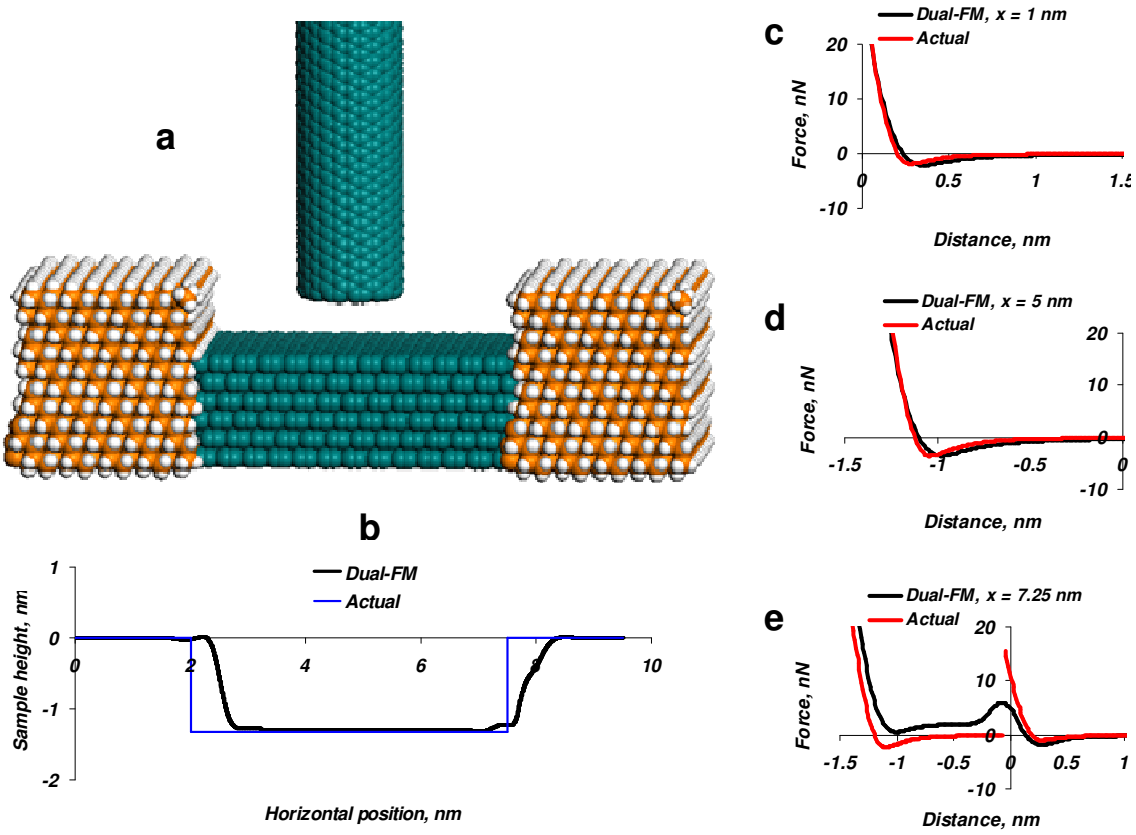

Figure 4-11 *(a) atomistic model of a 1.5-nm-diameter double-walled carbon nanotube AFM tip imaging a hypothetical 5.5-nm-wide, 1.37-nm-deep surface trench on a Si(111)-H surface with graphite bottom; (b) simulated dual-FM topography using parameters similar to those given for figure 4-9 for a single-cantilever case and a scan speed of 125 nm/s; (c)-(e) comparison of the actual and dual-FM force curves at various horizontal positions in figure 4-9b, x = 1, 5 and 7.25 nm, respectively. For clarity figure 4-11e shows only the approach force curves, which are different from the retract curves when probe slipping occurs, as illustrated in figure 4-12. The dual-FM curve for this case was constructed from the force gradient collected during the tip approach.*

graphite surfaces (Figure 4-11c and d), away from the steps. However, the agreement is poor when imaging directly over the trench edge due to the sharp changes in the force curve. This suggests that the proposed approach may only be accurate when the tip-sample force curves are smooth.

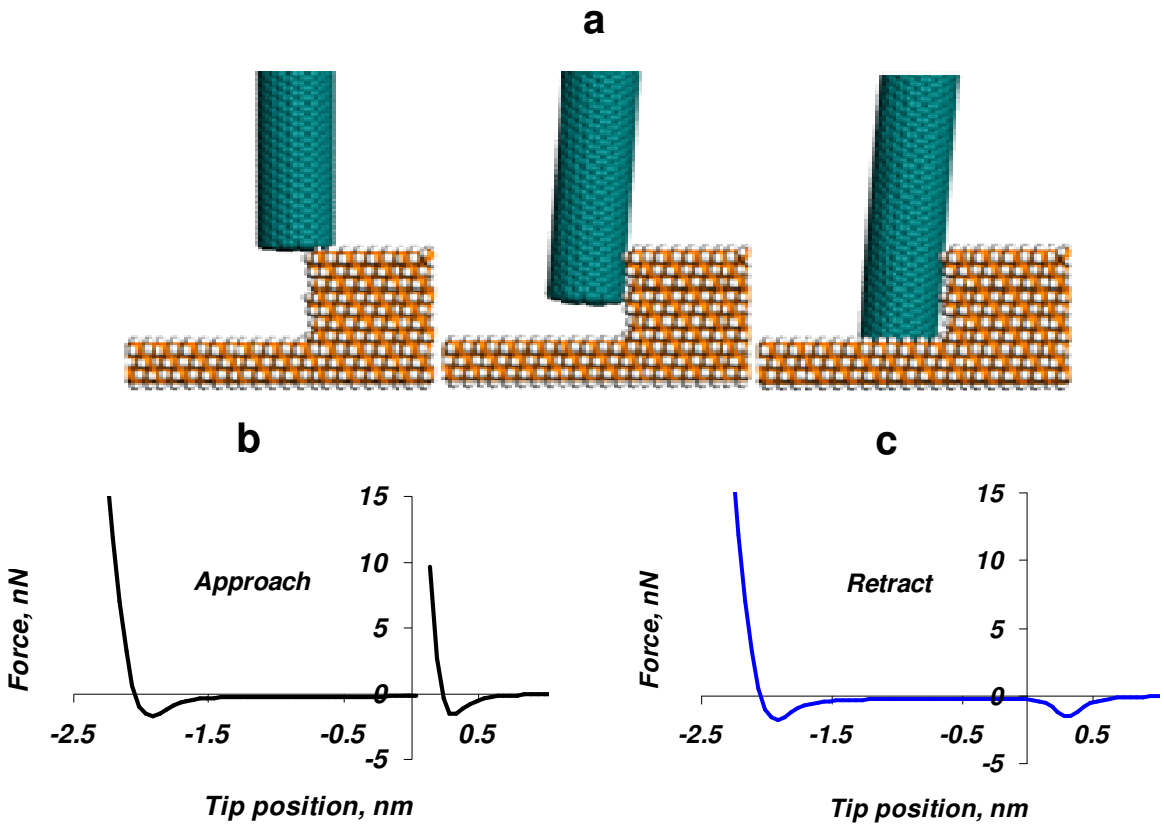

Figure 4-12 *(a) model of a 1.5-nm-diameter double-walled carbon nanotube probe approaching a sharp step edge on a Si(111)-H surface. As the images show, the probe initially compresses the step, but then bends (snaps) around it and continues descending until it reaches the lower terrace. As shown in (b) and (c), the tip-sample interaction force curve is different for the probe approach and retract.*

Although the expected performance is comparable for the single- and dual-cantilever schemes, there are some important differences between them, which have experimental implications. The single-cantilever approach is advantageous in that it does not require specialized cantilever design and manufacturing (standard cantilevers could be used), and in that the higher slope of the cantilever's free end (due to the higher curvature along the cantilever) *could* magnify the amplitude of the high-frequency oscillation measured by the laser-beam method if the beam can be focused precisely on the cantilever end. However, if the laser beam is not properly

focused on the cantilever end and is instead reflected simultaneously on regions of opposite slope between nodes along the cantilever, the intensity of the laser spot impinging on the photodetector that tracks the cantilever position could be reduced, leading to decreased sensitivity. Thus it is possible that more sophisticated tip tracking systems may be required.

The single-cantilever approach also has the disadvantage of requiring higher-than-typical excitation forces to induce vibration of the higher eigenmodes. This is because the effective stiffness of the different modes scales with the square of the frequency through the harmonic relationship,

$$\omega = 2\pi\nu = \sqrt{\frac{k}{m}} \tag{4.19}$$

where ω is the angular velocity, ν is the frequency, k the force constant and m the effective mass. Consider for example the AC160TS cantilever used in this study, which has a force constant of ~45 N/m for the fundamental mode. Based on the ratios of the various eigenmode frequencies to the fundamental frequency (shown in table 3), and the fact that the effective mass does not change, the 3rd, 5th and 7th eigenmodes have effective force constants of ~13,939, 145,181, and 632,968 N/m. Thus, the inertial force amplitude required to excite each mode for the same tip oscillation amplitude ($F = Ak/Q$, where A is the tip oscillation amplitude) increases rapidly with respect to the fundamental frequency, limiting the amplitude response of the higher modes that can be achieved with standard AFM piezoelectric exciters. Note that this refers to the *inertial force amplitude* required to excite the cantilever at the base, not the required *spatial oscillation amplitude* of the base, which is small (the inertial

force applied at the cantilever base is the mass times the second derivative of the position, which is proportional to the square of the frequency [87, 88, 92]). Significantly softer cantilevers (e.g., $k << 1$ N/m, as in biological applications) could be used to overcome this difficulty, but that may require using larger oscillation amplitudes of the fundamental frequency (to keep the tip from sticking to the surface) which would reduce the resolution of the force curve. Lower eigenmodes could be used, but this would also result in lower resolution. For example, Figure 4-13 presents the force gradient results (similar to those shown in Figure 4-7b) obtained using eigenmodes three, five and seven. It can be seen from graphs in Figure 4-13a, b and c that as the eigenmode order is increased, one obtains a finer resolution and lower hysteresis of force-gradient data and hence, a more accurate regression fit, which in turn results in a force curve that is in better agreement with the actual curve, as shown in Figure 4-13d (only odd eigenmode results are shown in this figure but we verified that the trend also holds when even eigenmodes are included). The high-frequency excitation force amplitudes required in the dual-cantilever approach are not necessarily as high as in the single-cantilever case because only the fundamental frequencies of each of the cantilevers are excited. Since the mass of the second cantilever can be selected to be small, the force constant of the second cantilever does not increase in the same fashion as with the single-cantilever case. Note that, as pointed out previously, the dual-cantilever scheme could require large base excitations for the second frequency due to the fact that the high-frequency excitation needs to pass through the first cantilever to get to the base of the second cantilever. However, this challenge could be overcome by directly exciting the second cantilever

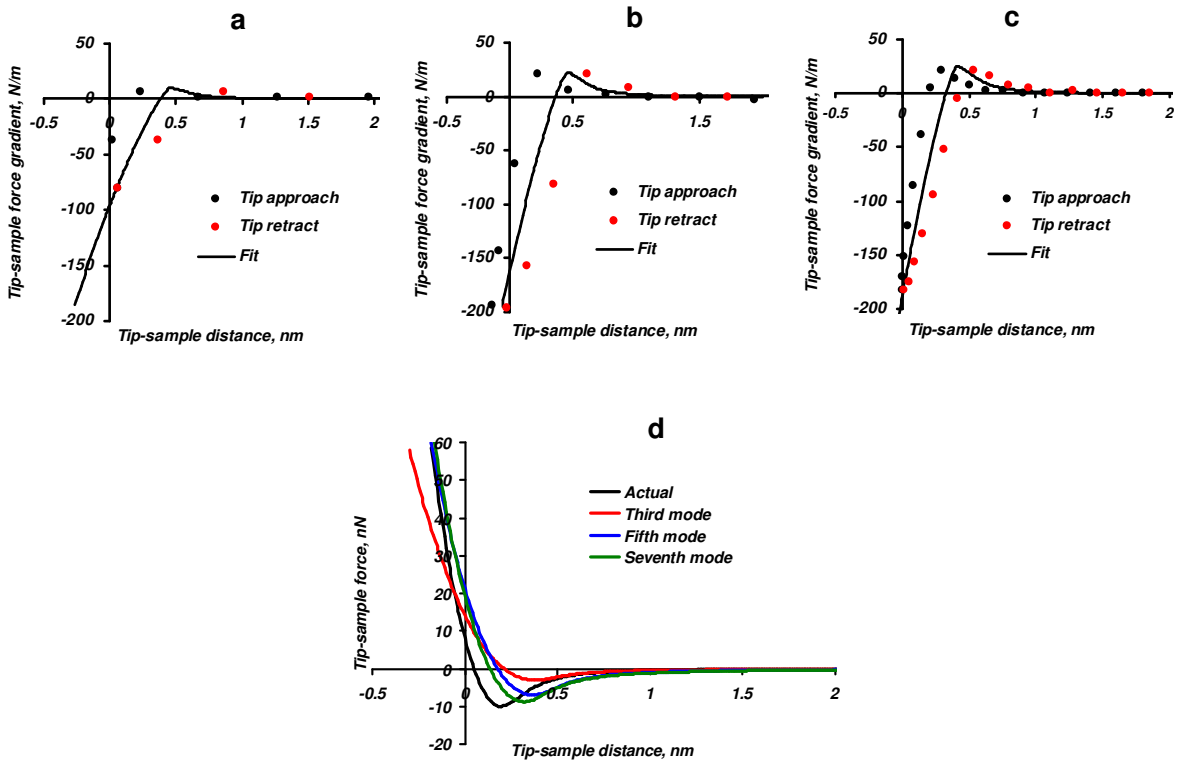

Figure 4-13 *Comparison of tip-sample interaction force gradient curves acquired using the third, fifth and seventh eigenmodes of the cantilever (a, b and c, respectively), and corresponding tip-sample interaction force curves (d). The simulation parameters used are same as those provided for figure 4-7, except for the appropriate frequencies and force constants of each eigenmode.*

tip through magnetic forces. Also, an alternative paddle-cantilever design that is conceptually similar to two cantilevers in series, shown in Figure 4-4 and Figure 4-5, can be easier to excite than the cantilevers-in-series design and can potentially be used.

Finally, an important challenge that affects both approaches is detection and processing of the large frequencies associated with higher eigenmodes. For the cantilever considered here, the 3rd, 5th and 7th eigenmodes have frequencies of ~4.1, 13.2 and 27.6 MHz, which are beyond the range of typical AFM equipment and have only been used in very specialized applications such as magnetic resonance force

microscopy. Depending on experimental limitations, the successful implementation of the dual-FM methods using standard AFM equipment may require a combination of using cantilevers with low force constant and fundamental frequency, and using relatively low eigenmodes such as the 3rd and 4th for the higher order oscillation.

Despite the experimental challenges, the proposed methodology is based on simple physical concepts whose feasibility has been verified through extensive numerical simulations (a significant number of cases involving cantilevers with force constants ranging from 5 to 300 N/m were also explored, giving qualitatively similar results to those reported here) and whose implementation holds significant promise in rapidly collecting *quantitative* mechanical information about the tip and the sample.

Upon thoroughly understanding the requirements of the dual-FM method for force curve measurements through numerical simulations, the first step towards experimental implementation was to build a robust setup that is capable of performing multifrequency operation including frequency-modulated control of the higher eigenmode. The preliminary experiments were conducted on a standard AFM system in our lab by modifying the operating software source code, but we soon realized that due to the order of frequencies involved and the stability required, a more advanced and dedicated control system is required. In the following section, the capabilities of standalone AFM are explained, along with that of the instruments that were obtained to be integrated with it in order to achieve the desired control of the cantilever. Following that, an approach towards the experimental implementation of this method with the data and observations will be discussed.

4.2 Development of the experimental setup

Our experimental setup consists of three external components that are integrated with a standard Atomic Force Microscope (AFM) system in order to extend its capabilities for obtaining improved control of oscillations at high frequencies (>1 MHz), to enable frequency-modulation control of the eigenmodes, to deploy extra lock-in amplifiers for detections at multiple frequencies and to perform data acquisition. This section will cover the details of all the components, with their capabilities and operation independently and as a single unit. The components that constitute the setup in our lab are: an Asylum Research [93] (Santa Barbara, CA, USA) MFP3D AFM, an RHK Technologies [94] (Troy, MI, USA) PLL Pro 2 controller, a Krohn-Hite Corporation [95] (Brockton, MA, USA) model 3945 filter, and an Agilent Technologies [96] (Santa Clara, CA, USA) DSO5012A oscilloscope.

4.2.1 Asylum Research MFP3D AFM

The MFP3D standard control system components include the following: a computer for the control software, the MFP3D head, a base to house the optics configuration, a vibration isolation table and a controller that communicates commands between the computer and the head. The controller has BNC ports on the front panel that allow connections with the external instrumentation. Within the controller, there are two digital lock-in amplifiers allowing driving and detection of the signals. The head has a cantilever holder attachment on which the AFM cantilever is mounted. It also contains piezo actuators to control the motion of the cantilever in x, y and z directions, and a segmented photodetector and a photodiode to capture the

laser beam bouncing off the cantilever to record the deflection. The base has a camera that projects live video of the cantilever and sample on the computer, allowing adjustments of the laser spot on the cantilever for suitable feedback on the photodetector. The sample is placed on the base and once the cantilever is installed on the holder, it is attached to the head and the head is then inverted and positioned above the sample on the base to start the imaging process. These components are seated atop a vibration isolation table in order to minimize interference from the surroundings. Ambient interference is also minimized by placing the whole imaging setup inside an acoustic enclosure that can be closed during scanning. Figure 4-14 shows the above mentioned components. The control software is based on Igor Pro from Wavemetrics and allows user to input the operation parameters and also provides a simple interface to acquire and analyze the data.

Once the sample and cantilever have been installed, the cantilever can be operated in one of the stable modes (contact-mode, amplitude-modulation mode, bimodal mode, force-curve acquisition mode) that the AFM is equipped with. The underlying principles behind these modes have been discussed in chapter 2 and their experimental operation procedures are explained below.

1. Contact-mode: To operate in contact-mode, the user defines a setpoint deflection value in the software and engages the tip to the sample. Before starting the imaging, scan speed, scan size and gains also need to be input. During imaging,

the deflection of the cantilever changes due to the topographical variations on the surface, to which the z piezo responds by moving up or down in order to maintain

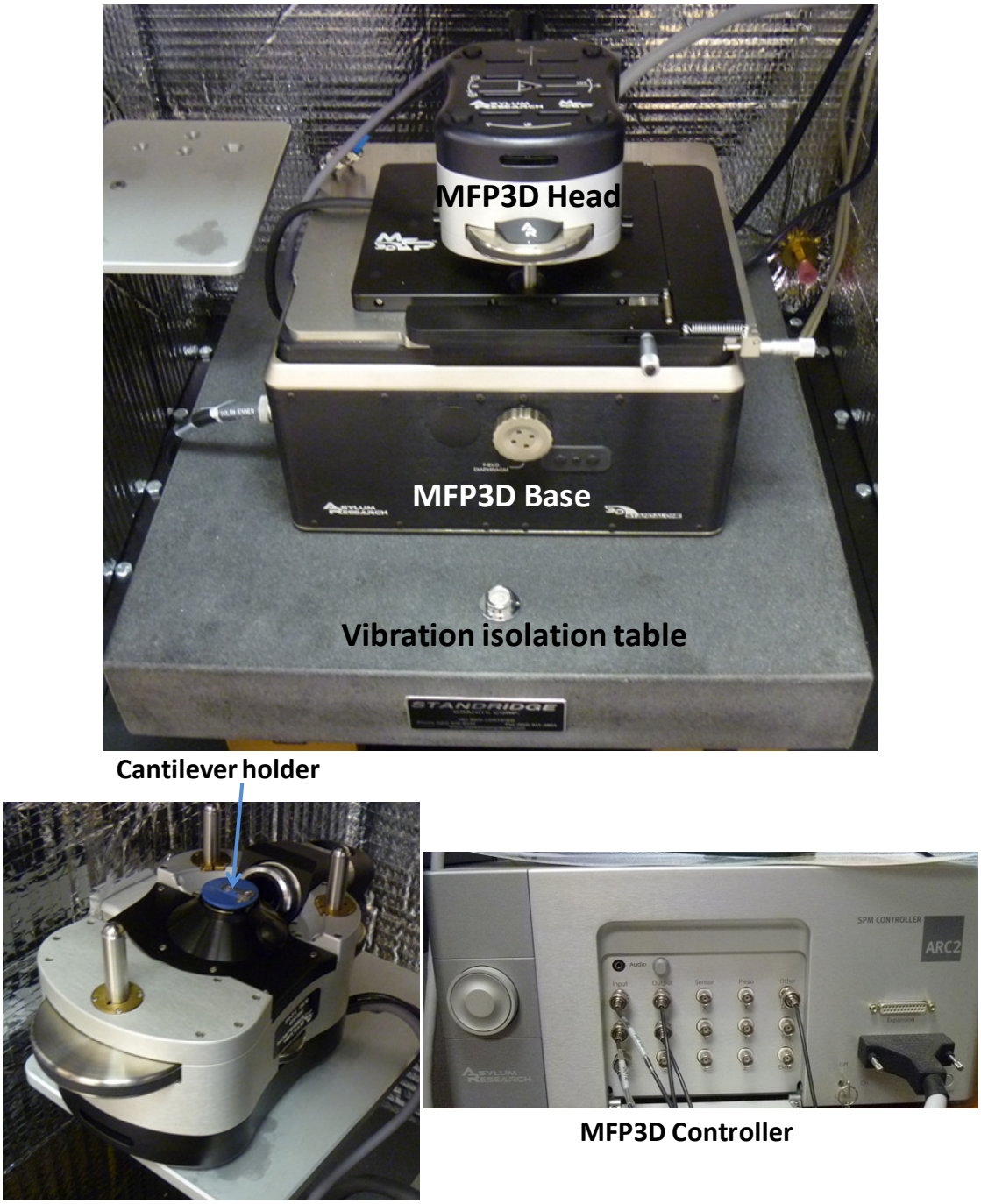

Figure 4-14 *(Top) AFM components as labeled, (bottom-left) Inverted MFP3D head, and (bottom-right) MFP3D controller.*

the deflection at the setpoint value. The change in deflection and *z* piezo movement values are transmitted to the software through the controller, which processes them in the form of 2- or 3-dimensional topographical image.

2. Amplitude-modulation mode (AC™ mode): In AC mode, the cantilever is first tuned to oscillate at the free resonance frequency of (typically) fundamental eigenmode with a user-defined target amplitude. The drive frequency can then be set to be at the resonance or any other value, as required. Next, a setpoint amplitude is defined and the cantilever is lowered towards the sample until the oscillation amplitude reduces to the setpoint value. Other operation parameters are same as for the contact-mode that need to be input before starting the scan. The output channels in this case are, height, amplitude error and phase shift between the drive and response. The height trace provides the topographical features on the surface by maintaining the setpoint amplitude and the phase shift can provide enhanced contrast corresponding to sharp variations in topography or can map the compositional variations on the surface.

3. Bimodal AFM (Dual AC™ mode): Here, in addition to an eigenmode that performs the imaging by operating at a set-point value (as in the AC mode), a higher eigenmode is also tuned to oscillate at a user-defined amplitude, at or away from its resonance frequency, and there is no setpoint feedback control incorporated for this eigenmode. The drive amplitude and drive frequency remain fixed for both of the eigenmodes during imaging. The output channels in this case

are amplitude error and phase shift for first eigenmode, and oscillation amplitude and phase shift for the higher eigenmode, in addition to the z piezo movement (height). Any of these channels can be visualized individually or by superimposing on the 3-dimensional topographical image as color maps to observe corresponding contrast variation on the surface.

4. Tip-sample force curve acquisition mode: In addition to the topography, the AFM can also acquire tip-sample interaction force curves in static mode, whereby the forces are directly obtained by measuring the cantilever deflection. To perform these measurements, a sample image is obtained using any of the above discussed imaging modes, then the points of interest are selected and the cantilever tip is moved to each of those points. The user defines the range of z piezo motion for force curves and a trigger-point deflection for the cantilever at which the z piezo reverses the direction of motion. The tip approaches and retracts from the sample and the resulting deflection data is recorded. The slope of this curve combined with thermal tuning of the cantilever allows calculation of the fundamental eigenmode stiffness. Consequently, the curves can be converted to tip-sample force versus sample indentation using the procedure described in chapter 2.

The operation modes discussed above are the ones available on the standard MFP3D AFM in our lab. However, with appropriate hardware and software modifications, the AFM can also be operated in many other modes such as magnetic force microscopy, phase-modulation mode etc. The MFP3D AFM offers

commendable flexibility with the availability of several BNC ports (Figure 4-14) on the front panel that make interfacing with external hardware straightforward, assisted

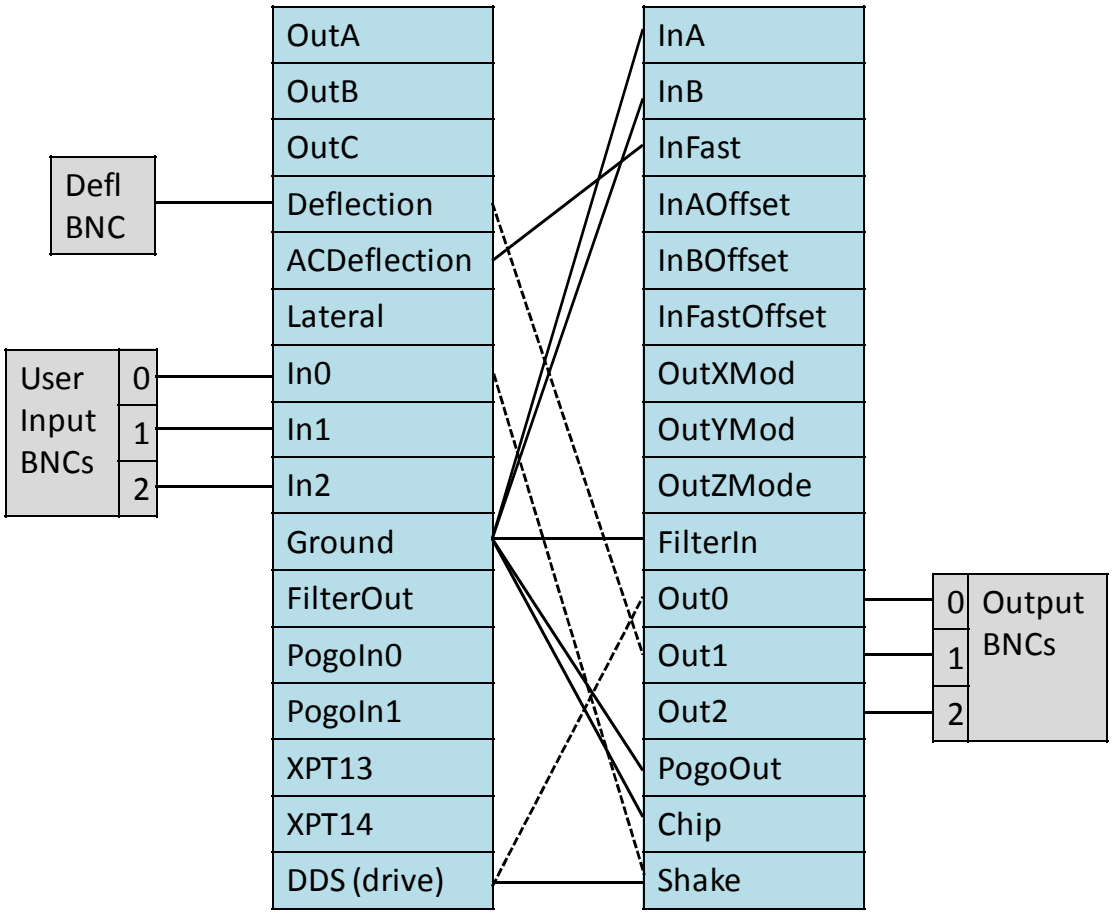

Figure 4-15 *Wire diagram of cross-point switch in MFP3D controller. Default connections in the controller (solid), examples of changes in software user interface (dashed). Gray boxes show some of the BNC ports on the front panel.*

by an in-built cross-point switch with a user interface in the control software that allows the user to change connections among the input and output channels. This allowed us to incorporate multifrequency operation with frequency-modulated higher eigenmode control, as will be discussed in the following sections. Figure 4-15 shows the wire diagram of the cross-point switch (with solid lines showing default internal connections) inside the controller with lists of available channels shown in *blue*

boxes. The *gray* boxes are the BNC ports available on the front panel for external connections (this figure shows only the BNC ports that were relevant for our experimental use and not all of them). A similar user interface in the software allows the changes in connections. For example the drive signal (*DDS*) that is by default connected to the shake piezo, can be instead generated externally and sent through the BNC *input port 0* (dashed line), and so on. Similarly, the response signals can be externally analyzed by connecting the appropriate channel to one of the output BNC ports (for example, drive signal is connected to *Out0* and deflection is connected to *Out1*, as shown with the dashed lines). Overall, there are three input ports that allow external signals to be sent to the AFM, three output ports making possible that the signals can be used for external processing, and a deflection port that outputs the cantilever deflection/oscillation signal. The wire connections with external hardware will be discussed in more detail in forthcoming sections while explaining the interfacing of external instrumentation with AFM.

4.2.2 RHK Technologies PLL Pro 2 controller

The PLL Pro 2 controller is a versatile AFM controller designed with a capability to simultaneously measure static deflection and the oscillation properties of a vibrating cantilever. It consists of a fully digital phase-locked-loop (PLL) circuit to perform amplitude and phase detection, and a DSP processor that calculates the drive signal and PLL tracking signals. The PLL Pro 2 controller has a control software installed on the computer that communicates the user inputs to it. This controller can interface with any standard AFM controller and can in turn be used to control the

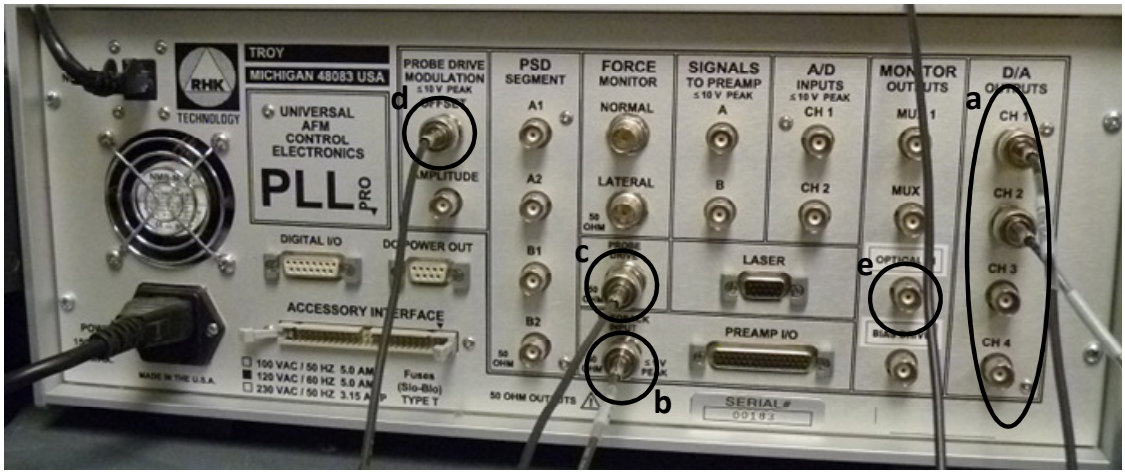

Figure 4-16 *PLL Pro 2 controller.*

cantilever motion. The BNC ports on the PLL Pro 2, as shown in Figure 4-16, allow signals to be sent in and out of it. There are four 20 bit D/A channels (Ch1, Ch2, Ch3 and Ch4 – labeled as '*a*' that have a range of +/-10 V and where the output signals from the PLL Pro 2 are available. There is a feedback input BNC port *'b'*, where the photodetector signal from AFM controller is sent as a feedback signal. Optical-In port *'e'* can also be used to send a signal in to PLL Pro 2, if required. Probe drive BNC port *'c'* provides the output signal generated by the PLL Pro 2 based on the feedback

signal received, depending on the mode of operation. The probe drive signal from the controller can also be offset with any external waveform by sending that signal to the probe-drive-modulation-offset port *'e'*. This port has an attenuation of 10 times built into it, which means that any input on this port will reflect 10 times smaller in the offset of the probe drive. In addition to these, there are other connection ports available, which can be useful for various applications, but are not directly relevant to the experimental methods discussed in this dissertation. The internal circuit diagram of the PLL Pro 2 is shown in Figure 4-17.

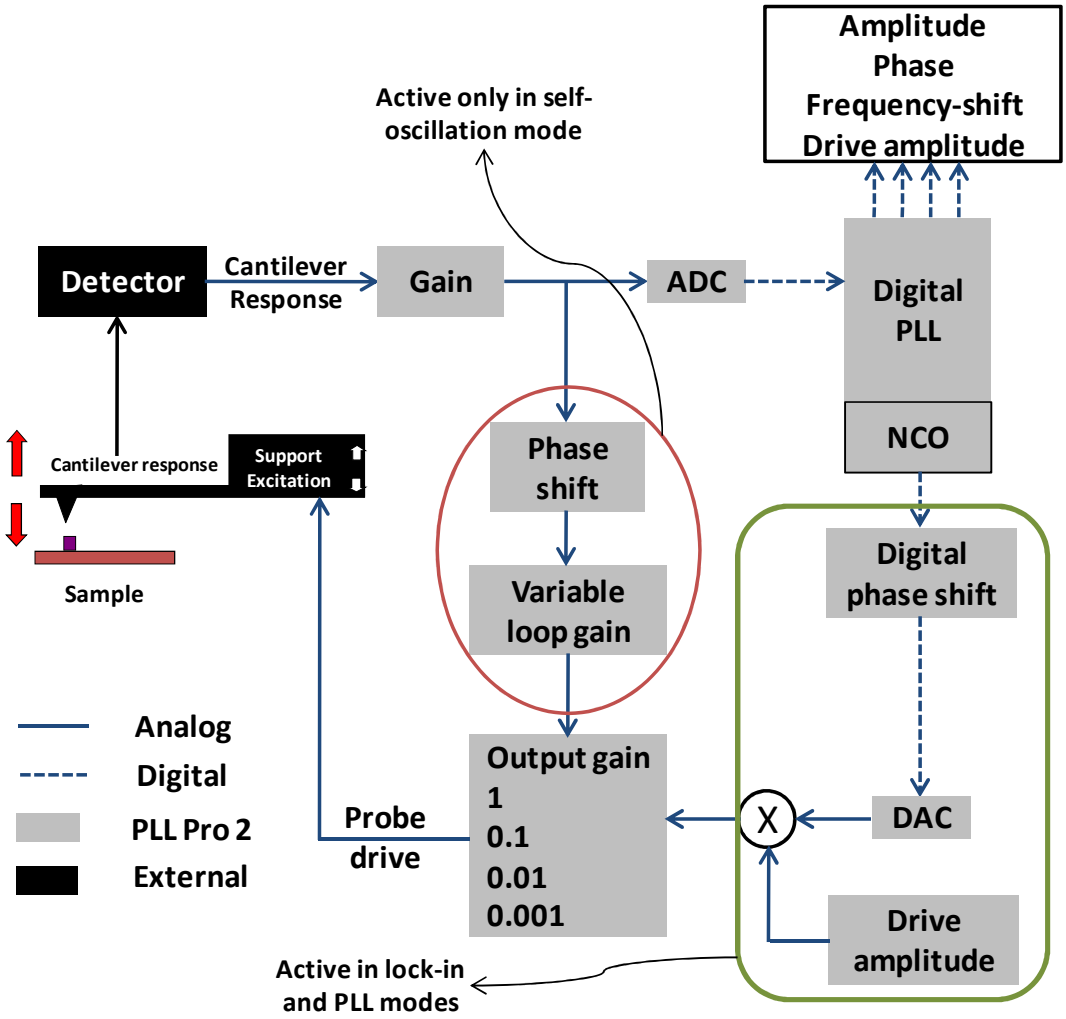

Figure 4-17 *Internal circuit diagram of PLL Pro 2 controller.*

The software interface to control the PLL Pro 2 operation also allows real-time monitoring of the signals, such as amplitude, phase shift, frequency shift etc. The controller can operate in four modes: static mode, lock-in mode, self-oscillation mode and PLL mode, as discussed below.

1. Static mode: This is basically the standard *contact mode* operation, in which the cantilever is not oscillated and the measured feedback parameter is the deflection. Since the MFP3D AFM controller is capable of performing this operation, the PLL Pro 2 has not been operated in this mode for our experiments.

2. Lock-in mode: The primary purpose of this mode is to operate the controller as a lock-in amplifier to measure the amplitude of the oscillation and the phase shift between excitation and response signals, by calculating the in-phase (I) and quadrature (Q) components. This mode can also be used for amplitude-modulation operation similar to the AC mode discussed for the MFP3D controller, in which a fixed drive amplitude is sent to the cantilever at a fixed drive frequency for its excitation. The feedback received on the PLL Pro 2 is the cantilever oscillation signal. In general, any frequency can be input by the user if the objective is to only monitor the corresponding response amplitude and phase shift. However, if the goal is to drive the cantilever at or around its resonance frequency, the steps involved in operating the PLL Pro 2 are, (a) tuning of the cantilever to find the peak in the amplitude response of the frequency sweep curve, (b) selecting the resonance frequency for the operation, which also allows

calculation of the signal to drive ratio, and (c) adjusting the drive amplitude that results in the desired value of the amplitude of the cantilever. Once tuned, this can drive the cantilever and the resulting amplitude and phase shift can be monitored on the display panel of the software. The measured variables can also be sent to the AFM controller to create images or to the oscilloscope to observe their time response.

3. Self-oscillation mode: In this mode, the control of the oscillation is analog (Figure 4-17), where the PLL Pro 2 shifts the phase and amplifies the response signal from the cantilever and feeds it back into the probe drive output as the new cantilever excitation. This means that the PLL circuit is not a part of the excitation loop here and is only used as a device for detecting the amplitude and frequency of the cantilever oscillation. In self-oscillation mode, as discussed in the chapter 2 for the FM-AFM mode operation, the operation is always at resonance by enforcing a 90^{o} phase shift between the drive and the response. For the PLL Pro 2 operation in self-oscillation mode, first the cantilever is tuned in lock-in mode, and then switched to this mode. There are two modes of self-oscillation operation, 1) constant-excitation (CE), in which the drive amplitude is fixed, and 2) constant-amplitude (CA), in which the response amplitude is maintained at a constant value by adjusting the drive. After the cantilever control is switched to this mode, the phase shifter setting needs to be adjusted for maximum amplitude response in CE mode and minimum drive signal in CA mode. Also, before the imaging can be performed in either of these modes, it is necessary to tune the PID

gains to respond to the changes in the frequency shift and oscillation amplitude (for CA mode). The tuning of the gains is simpler and is typically performed by operating in the PLL mode (discussed next) prior to switching to the self-oscillation mode. The output channels available in this mode are response amplitude, phase shift, frequency shift and drive amplitude. The advantage of operating the PLL Pro 2 in this mode is its fast feedback to variations in the cantilever oscillations. The disadvantage is that unless a bandpass filter is applied around the frequency of interest, there is no control over the eigenmode that gets excited when the cantilever has multiple resonances in the range of the instrument.

4. Phase-Locked-Loop (PLL) mode: Here, the PLL circuit is the essential part of the cantilever excitation loop (Figure 4-17). The PLL reference oscillator generates the probe drive signal and maintains the phase between the drive and the response at a fixed value by using cantilever response as the feedback. The operation can be in CE-PLL or CA-PLL modes, similar to the self-oscillation mode. The PLL measures the amplitude and phase of the oscillation signal. The amplitude value is then used as an input for PID controller that maintains stable drive amplitude for the CE mode or constant response amplitude for the CA mode. A significant advantage of operating in the PLL mode is that the drive signal is a clean sinusoidal wave. However, the disadvantage is its relatively slow response to distortions in cantilever oscillations. The output channels in this mode are the same as for the self-oscillation mode.

4.2.3 Krohn-Hite Corporation model 3945 filter

This filter is a programmable Butterworth/Bessel filter that provides one Butterworth channel (*CH 2.1*) of low-pass, tunable over the range from 170Hz to 25.6MHz; and two independent Butterworth or Bessel channels (*CH 1.1*, *CH 1.2*) of low-pass, high-pass, by-pass or one channel of band-pass or band-reject, tunable over the range from 3Hz to 2MHz. The filter has been specifically designed for applications requiring high frequency band-pass filtering. The high cutoff may be set to any frequency between 170Hz and 10MHz, and low cutoff to any frequency between 3Hz and 2MHz. Channels *1.1* and *1.2* furnish Bessel or Butterworth transfer functions and can be programmed to operate as two low-pass, two high-pass, one band-pass or one-band reject filter with gains up to 40dB per channel. The input gain is useful to increase the amplitude of the signal and improve the signal-to-noise ratio

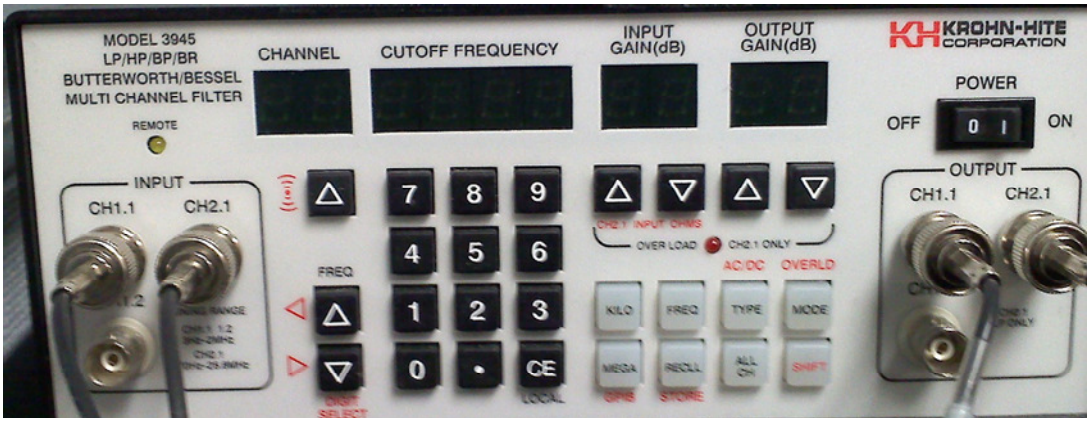

Figure 4-18 *Front panel of the filter.*

before filtering. Each channel also has an option to adjust the output gain. Figure 4-18 shows the front panel of the filter consisting of the display, BNC input/output ports and the controls. The BNC ports enable us to input and output the signal to and from MFP3D and PLL Pro 2 controllers. Another application the filter can be employed for

is as an amplifier. If any of the channels is not set to the filter function, it can be used only as a gain multiplier to the incoming signal, if required.

4.2.4 Agilent Technologies DSO5012A oscilloscope

The front panel of the oscilloscope is shown below in Figure 4-19. This is a 2 channel oscilloscope with a bandwidth of 100 MHz and a sampling rate of 2GSa/s, which is useful to monitor the high-frequency AFM signals. It is also possible to perform data acquisition on this and save up to 8 million points of a waveform, with up to 12 bits resolution. An important function of oscilloscope in this setup is monitoring the response while tuning PID gains for the PLL Pro 2. The objective is to adjust the gains such that the sharp changes in the variables can be tracked effectively by observing a high-resolution signal.

Figure 4-19 *Front panel of the oscilloscope.*

4.2.5 Interfacing PLL Pro 2 with MFP3D AFM for frequency-modulated control of higher eigenmodes

The primary objective of having the above instruments in addition to the MFP3D AFM system was to operate them in parallel in order to incorporate frequency-modulation control on a higher eigenmode for dual-FM spectroscopy. Upon understanding the capabilities of PLL Pro 2 and MFP3D controller, it was realized that new imaging techniques can also be implemented through bimodal and trimodal operations using the PLL Pro 2 to control higher eigenmodes in lock-in, PLL and self-oscillation modes. The lock-in mode operation in the PLL Pro 2 is useful for the eigenmodes with frequencies above 1 MHz due to its more stable control as compared to the in-built open-loop control in MFP3D controller.

The basic wire connection layout of the instruments for all these operations is the same, as is shown in Figure 4-20 (note that not all but only the BNC ports on the instruments that are required in our experiments are shown in the block diagram). The deflection signal is taken from the *deflection* output port on MFP3D controller and sent to the filter *input port 1.1* to apply a band of frequencies around the eigenmode of interest. The corresponding *output port 1.1* of the filter is then connected to the PLL Pro 2 as the *feedback input* from the AFM. Based on the mode of operation of the PLL Pro 2, it generates a drive signal, which is sent to the filter *input port 2.1* through *probe drive* output on the PLL Pro 2. In this case, the filter acts as an amplifier (if required) and the output from *port 2.1* is sent to the MFP3D controller *input port 0*, which is connected to the cantilever shaker. At the same time, for multifrequency operations, the MFP3D controller provides excitation for one or two

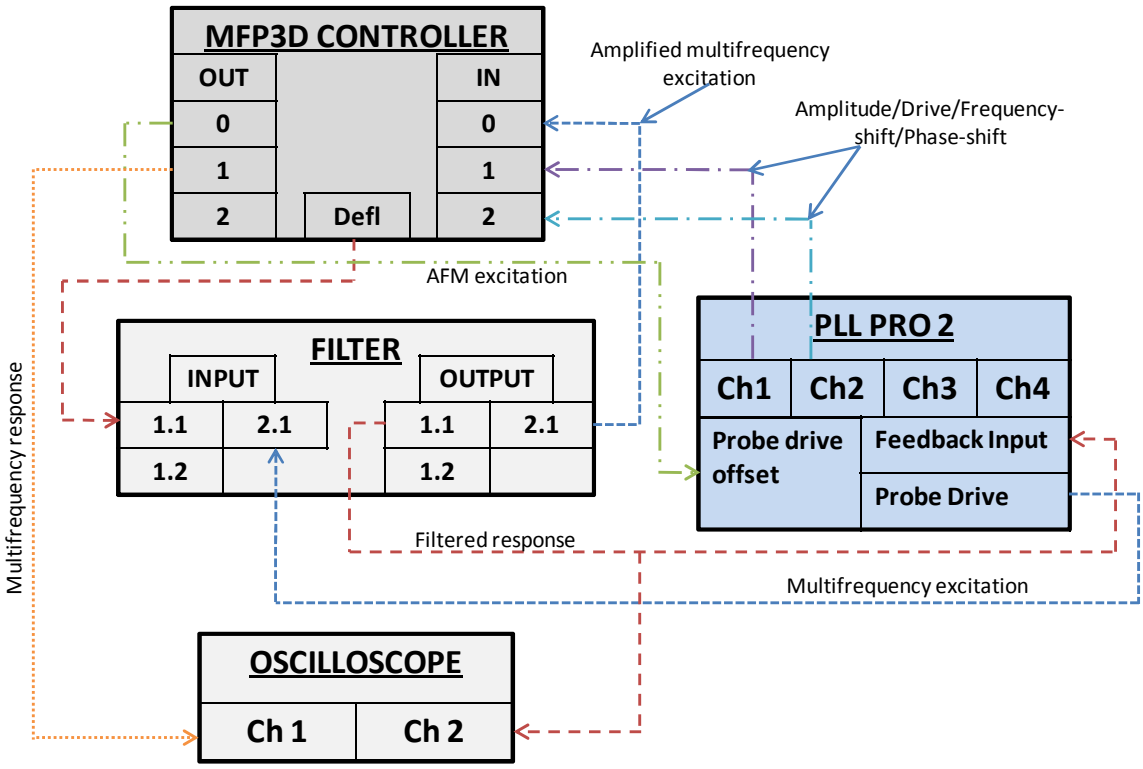

Figure 4-20 *Connection diagram of the instruments. Only the BNC ports that have been used for experiments are shown and not all that are present on the instrument.*

eigenmodes, which are connected to *probe drive offset* port on PLL Pro 2 as a bias signal through *output port 0*. The response variables for the PLL Pro 2 controlled eigenmode can be output using *channels 1 to 4* and analyzed either within the AFM control software by connecting them to *input ports 1 & 2* on the MFP3D controller or to oscilloscope *input channels 1 & 2*. Any signals of interest can be taken from the remaining of the MFP3D output ports and can be sent to the oscilloscope to monitor them. Note that appropriate changes are required to be made in the crosspoint panel in the MFP3D software in order for these connections to work, as explained in section 4.2.1. Using this setup, the applications of the bimodal and trimodal operations are discussed with results in sections 4.3, 4.4 and 5.2, with the respective steps involved in simultaneous operation of the controllers for specific modes of operation.

In summary, various modes of operation in the stand-alone AFM and MFPD controller have been understood through their independent operations. The flexibility provided by the presence of connection BNC ports on the MFP3D controller with crosspoint switch and excellent controls in the PLL Pro 2 controller have enabled us to explore applications of various control modes in bimodal and trimodal imaging and spectroscopy. As first of its applications and the original motivation, experimental work for the implementation of dual-FM spectroscopy method is discussed in the following section.

4.3 Dual-FM atomic force spectroscopy: experimental progress

A block diagram of the control scheme required to experimentally implement the dual-frequency spectroscopy method is illustrated in Figure 4-21. The signal processing block of the diagram represents the processing required on the high-frequency oscillation in order to track the fast changes in its response due to the tip

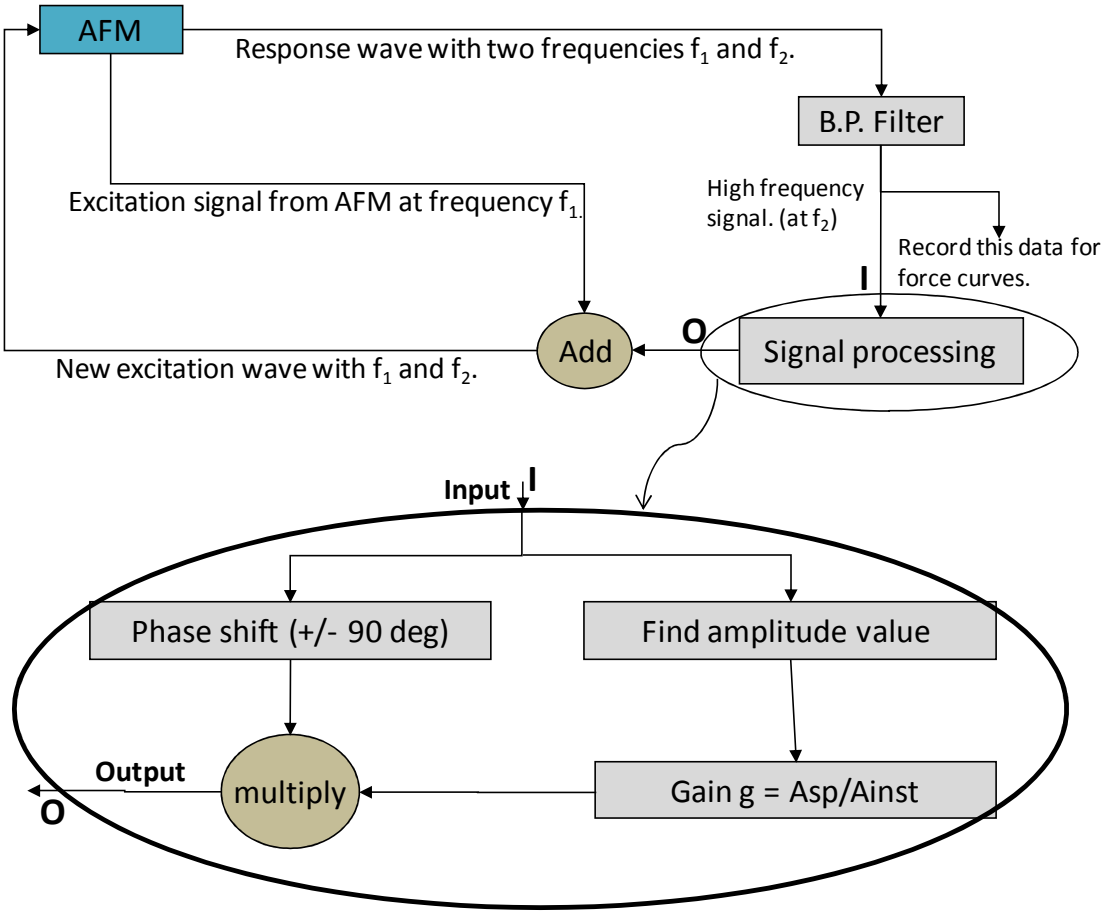

Figure 4-21 *Block diagram of the experimental set up required for dual-frequency atomic force spectroscopy method.*

interactions with the sample. This signal processing circuit needs to be integrated with a standard AFM system that controls the low-frequency oscillation to perform

intermittent-contact imaging on the sample. Of the two AFM sensor designs discussed in section 4.1, for the efforts discussed here, we have used two eigenmodes of a standard AFM cantilever for achieving the dual-frequency motion. As shown in Figure 4-22, the objective is to be able to record the changes in the frequency of each oscillation of the higher eigenmode (the circled region in the figure is where the tip is interacting with the sample and each oscillation has a different frequency) with the instantaneous tip position obtained by assuming harmonic response for the fundamental eigenmode, which can be converted to force curves using the steps discussed in section 4.1. This section covers the experimental development of the above control scheme on our AFM system, followed by the results and observations.

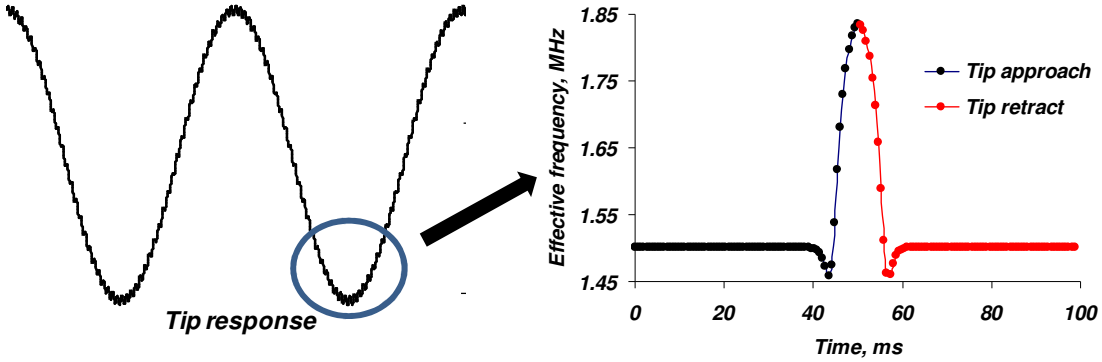

Figure 4-22 *Instantaneous frequency of a higher-mode oscillations for one low-frequency cycle (region shown in circle is where tip is interacting with the sample).*

4.3.1 Experimental implementation of dual-FM controls

The signal processing block shown in the Figure 4-21 is similar to self-excitation controls that are routinely employed in the FM-AFM mode of imaging. As previously discussed, in this method, the cantilever excitation is directly determined by the cantilever response and 90 degrees phase shift is always enforced between the response and the excitation. The required dual-frequency motion with the higher

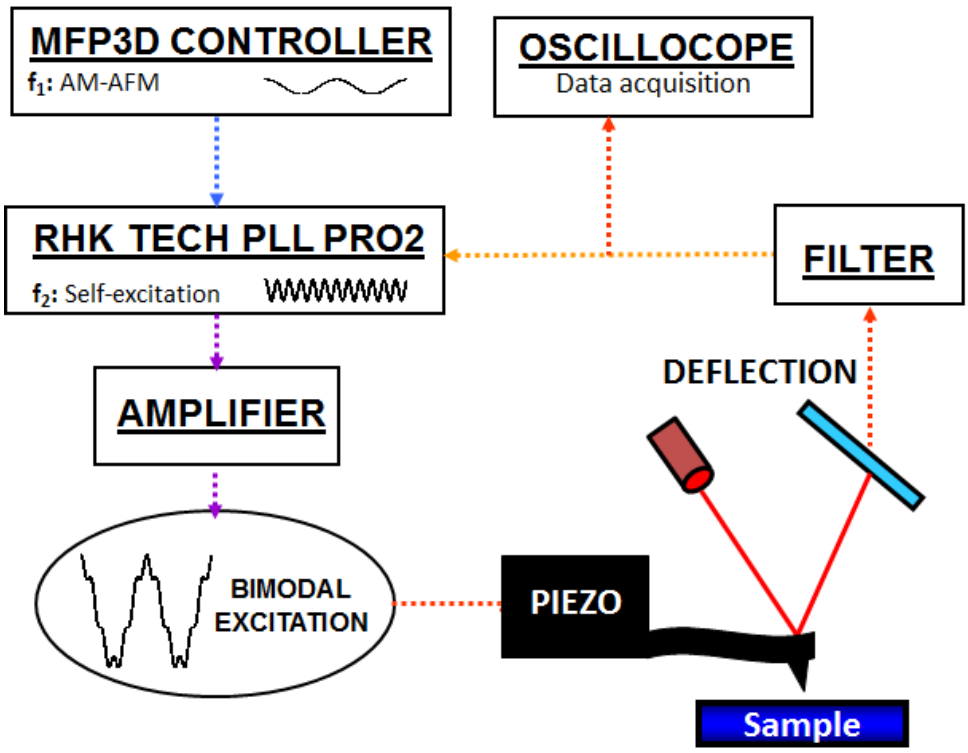

Figure 4-23 *Schematic of dual-FM experimental setup.*

eigenmode in self-excitation loop has been achieved on our setup by interfacing the PLL Pro 2 controller with the MFP3D AFM system. The schematic of the instrumentation is shown in Figure 4-23 and the start-up steps consisted of (1) tuning the first eigenmode in the MFP3D controller to operate in AC mode, (2) independent tuning of a higher eigenmode in self-oscillation mode in the PLL Pro 2 controller (upon processing the deflection signal through the bandpass filter around the higher eigenmode), and (3) combining the excitation signals of the two eigenmodes to drive the cantilever. The details of tuning the eigenmodes in each controller with their connections have been explained in section 4.2. The first eigenmode has a fairly large amplitude in order to achieve stable tapping on the sample, while the PLL Pro 2 controller tracks the response of the higher mode oscillating through the tip-sample interaction potential at a relatively much smaller amplitude.

4.3.2 Results and discussion

The experiments were performed using cantilevers with different eigenmode parameters on various samples covering a range of surface properties. For the presented data, the first and fifth eigenmodes of a Nanoworld Zeilr-10 silicon cantilever [97] have been driven in AM-AFM and self-excitation modes, respectively, in order to obtain a sufficiently high frequency ratio. The operation parameters are, free resonance frequencies f_1 = 27 kHz and f_5 = 1.39 MHz (frequency ratio ~ 52), free oscillation amplitudes $A_{1\text{-}o}$ ~ 80nm and $A_{5\text{-}o}$ ~ 4nm, with $A_{1\text{-}setpoint}/A_{1\text{-}o}$ = 0.75. Stable imaging operation on a silicon sample was achieved with these parameters. However, a challenge was encountered in the direct measurement of the instantaneous frequency for every oscillation of the fifth eigenmode, which is necessary in order to successfully construct the force curves from frequency shift data. Typically, the frequency measurements in FM-AFM systems are performed by a PLL circuit by averaging the data over a large number of oscillations, which is different from the requirement here. The approach adopted to address this issue was by acquisition of the time response of the filtered higher eigenmode using an oscilloscope (Figure 4-23) and post-processing this data to detect the zero crossings of the signal, which can be converted to its instantaneous frequency. In the portion of the oscillation where the cantilever motion is influenced by the tip-sample interaction forces, the frequency of each of the high-frequency oscillations should be different.

Figure 4-24 shows the total recorded response of the cantilever with time when it was operated under dual-FM controls (a), the filtered higher eigenmode time-response including the region where the tip was interacting with the surface (b), and

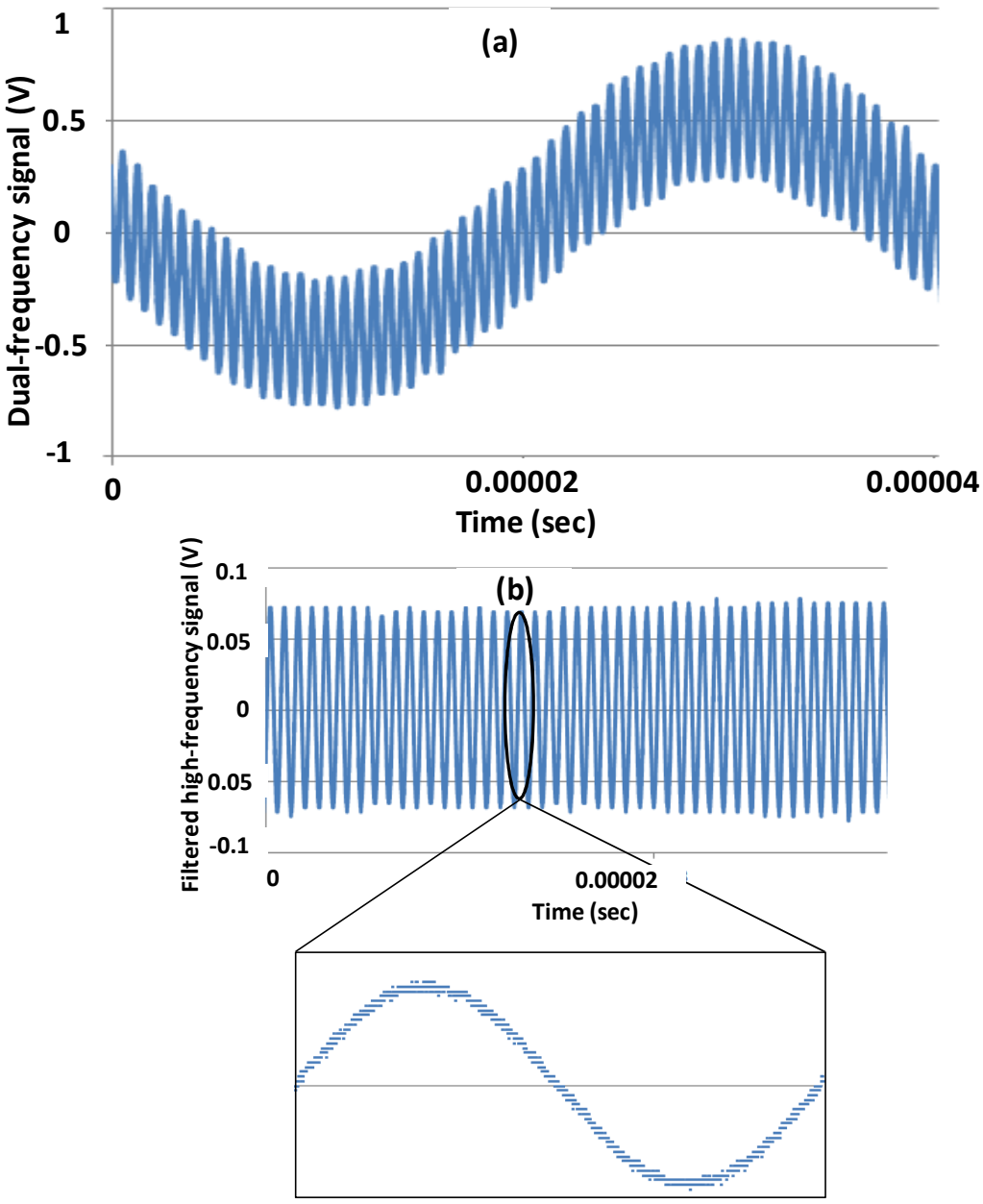

Figure 4-24 *Response of an AFM cantilever in dual-frequency operation, where the fundamental eigenmode is controlled in tapping-mode and the fifth eigenmode is controlled in self-excitation mode. (a) is the complete signal with the high-frequency oscillation superimposed on the fundamental oscillation, (b) is the filtered high-frequency oscillation which is used to calculate its instantaneous frequency.*

a zoomed-in view of the filtered signal showing only one higher eigenmode oscillation. In the magnified image, it is observed that,

1. Because the oscilloscope has a maximum vertical resolution of 8 bits in the normal acquisition mode, it does not capture the changes in the signal that are smaller than the minimum detectable voltage and assigns the same value to more than one point even if the values are actually different. This results in a discontinuous stream of the recorded data, making it impossible to obtain an accurate representation of the signal.
2. Given the time scales, even a small noise in the system will result in loss of precision in the representation of the data on the time axis.

Now, due the fact that the higher eigenmode frequency is very high (i.e., has very small periods of oscillation), even a small misrepresentation of the acquired signal on the time axis will result in large deviations in the frequencies calculated using the method of zero-detection by post-processing the data. Such falsely observed shifts in frequencies can be greater than or of the same order as the expected frequency shift in the response due to the tip-sample interactions, rendering this approach of frequency calculation ineffective. The observations were similar for experiments performed with different acquisition modes of the oscilloscope and with different operation parameters of the cantilever.

Despite the capability to operate a cantilever with the proposed control scheme, the implementation of the dual-FM spectroscopy technique is still not completely possible due to the lack of proper instrumentation to capture the fast frequency changes. Most of the instruments that are commonly used for measuring frequencies

operate with a set bandwidth that performs the calculations by averaging over several oscillations. Some possibilities have opened up with recent developments of AFM sensors with very high frequencies (of the order GHz) [98]. Such sensors could possibly be used to develop systems similar to the dual-cantilever system shown in section 2.1, in order to achieve a large number of high-frequency oscillations superimposed on the low-frequency motion, such that the averaging is possible for frequency shift measurement with the standard instrumentation. However, advanced AFM systems will be required to control the oscillations at such high frequencies.

In summary, an experimental approach has been discussed as a part of the efforts towards experimental implementation of the dual-FM force spectroscopy method and the challenges associated with it have been laid out. Further developments in the instrumentation or an improved way to measure frequencies will be required to successfully perform force curve acquisition using this technique.

4.4 Mapping of conservative and dissipative tip-sample interactions in bimodal AFM imaging experiments

As previously mentioned, an important application of dynamic modes of AFM, in addition to probing surface structure and conservative forces, has been measurement of dissipative tip-sample interactions [15-18]. Dissipation in dynamic AFM represents a cumulative effect of interactions including, but not limited to, long range electrostatic and hysteretic inter-atomic energy losses that occur during approach and retraction of the tip from the surface [19-22]. Both of the commonly used single-frequency modes, amplitude-modulation (AM-AFM) and constant-amplitude frequency-modulation (FM-AFM), have been shown to be capable of mapping dissipation on the surface in the form of phase shift and drive amplitude output channels, respectively. However, since either the amplitude or the frequency shift is maintained at a set-point value during imaging in these modes of operation, it has been shown that in the absence of dissipation, the output variables exhibit no sensitivity to variations in conservative interactions. Therefore, the advantage of performing these measurements in bimodal operation is that the unrestricted sensitivity of the higher eigenmode response to the tip-sample interactions, as has been discussed.

In this section, the focus is to study mapping of tip-sample interactions during bimodal AFM imaging in ambient air, where the fundamental eigenmode is controlled in AM-AFM mode and a higher eigenmode oscillates in open-loop mode

or is actively controlled in constant-excitation and constant-amplitude phase-locked-loop modes, hereby referred to as CE-PLL and CA-PLL modes, respectively [99]. In open-loop operation, the higher eigenmode is always driven at its free resonance frequency with a constant drive amplitude and is allowed to freely respond to the tip-sample interactions. In CE-PLL mode, on the other hand, the drive amplitude is fixed but the excitation frequency is continuously updated to the effective resonance frequency of the eigenmode by maintaining a 90 degrees phase shift between the response and the drive. CA-PLL mode differs from CE-PLL mode in that the drive is not fixed and varies to maintain a constant response amplitude when the tip is interacting with the sample. The objective is to quantitatively compare and understand the applications of the three aforementioned control modes. Such a control scheme, with higher eigenmode in frequency-modulated mode (PLL) while the fundamental eigenmode is in AM-AFM mode in air, has not been incorporated before and its comparison with the conventional bimodal operation in air will be useful in understanding their merits in imaging the surface composition.

4.4.1 Experimental method and measurements

The schematic of experimental setup is shown in Figure 4-25. The MFP3D AFM controller has been used to control the fundamental cantilever eigenmode in AM-AFM mode to dictate the primary oscillation for the topographical scan. A higher eigenmode (in the presented work the third eigenmode due to its high Q, allowing stable PLL mode controls) oscillation governed using the PLL Pro 2, was superimposed on the fundamental eigenmode oscillation, interchangeably in open-

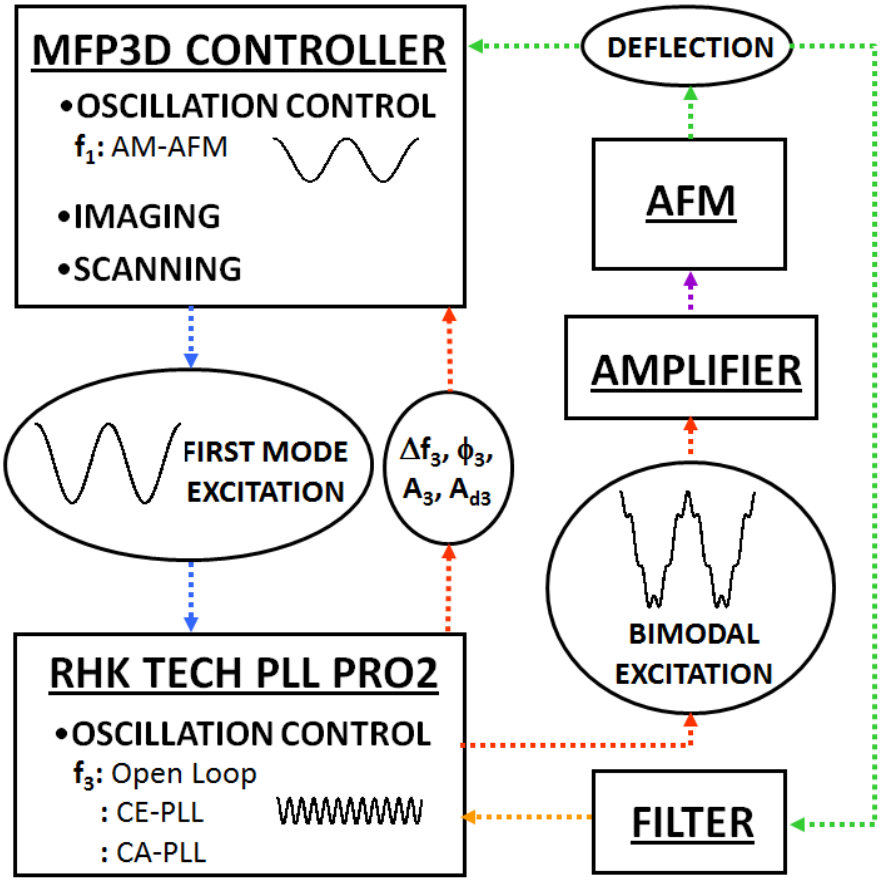

Figure 4-25 *Diagram of MFP3D AFM system used for controlling the fundamental eigenmode in AM-AFM mode, interfaced with the PLL Pro 2 controller used for driving and controlling the higher eigenmode in open-loop, CE-PLL and CA-PLL modes.*

loop (or lock-in mode), CE-PLL and CA-PLL control modes. The initial setup steps consisted of (1) tuning the fundamental eigenmode using the MFP3D controller at the target amplitude, (2) independent external tuning of the third eigenmode in open-loop and PLL mode (this was accomplished by sending the cantilever deflection signal with a bandpass filter around the third eigenmode to the PLL Pro 2 controller, which generated an excitation signal based on the feedback received from the incoming deflection signal), (3) adding the excitation signals for the two eigenmodes coming from the MFP3D controller and the PLL Pro 2 and sending the compound excitation

signal to the cantilever shaker. The detailed procedure of tuning the eigenmodes using these two controllers in various control modes and their simultaneous operation in bimodal mode by integrating them is explained in section 4.2.

For all the experiments, there are two output channels from the PLL Pro 2, depending on the control mode that the third eigenmode is operated in, *i.e.*, in (a) open-loop: its instantaneous amplitude and phase shift, (b) CE-PLL mode: its instantaneous amplitude and frequency shift, and (c) CA-PLL mode: the change in drive required to maintain the oscillation at constant amplitude and frequency shift. These outputs were then sent to the MFP3D controller to process the data to create an image or spectroscopy curve. In both of the PLL mode operations, it was ascertained that the phase shift variations from 90 degrees are within the noise level and the operation is always maintained at resonance. The sample used is a blend of Polystyrene (PS) and Polyolefin Elastomer (PE) spun-cast onto a silicon substrate, creating a film with varying material properties [100]. The PS regions of the sample have elastic modulus (E) around 2 GPa and low dissipation, whereas the PE regions have elastic modulus (E) of approximately 0.2 GPa and higher dissipation. The cantilever used is an Olympus AC240TS [101], with the following measured operation parameters for the first and third eigenmodes: resonance frequencies, f_1 = 80.98 kHz and f_3 = 1.319 MHz, Quality factors, Q_1 = 178 and Q_3 = 673, and spring constant, k_1 = 2.38 N/m. Typical scan images are shown in Figure 4-26 on a 5 x 5 μm^2 area, where the third eigenmode is operated in CA-PLL mode and frequency shift and drive amplitude have been superimposed on the topography of the sample. As anticipated, in the PE polymer regions, we observe a drop in the frequency shift

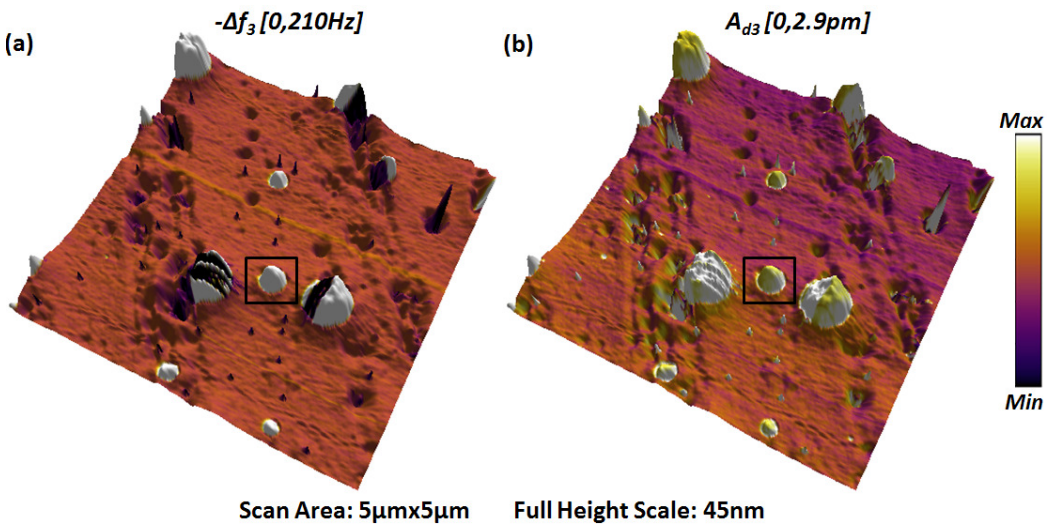

Figure 4-26 *Third eigenmode frequency shift contrast and drive amplitude contrast superimposed on the sample topography for the two-component polymer sample used. The frequency shift and drive amplitude ranges were determined by the difference between minimum and maximum values measured during the scan. Note that the image shows the negative of the frequency shift. The free oscillation amplitudes were approximately 80 nm and 9 nm, respectively, with a setpoint amplitude of 58nm.*

because the tip-sample interaction in this region is weakly repulsive due to the very small elastic modulus, and an increase in the drive amplitude indicates higher dissipation. Similar scan images were also acquired in open-loop and CE-PLL modes with their respective outputs, verifying the variations on PS and PE polymer regions.

A small region containing both polymer components as marked in Figure 4-26 is selected to compare the third eigenmode contrast obtained in the three control modes, as shown in Figure 4-27. The free oscillation amplitudes for the first and third modes are 80 nm and 9 nm, respectively. The cantilever tip is engaged to the sample on the PS region with a first eigenmode setpoint amplitude 72 per cent of its free oscillation amplitude, and its phase shift was monitored to ensure that the tip is in the repulsive regime of tip-sample forces before scan is started. Following this, the area is

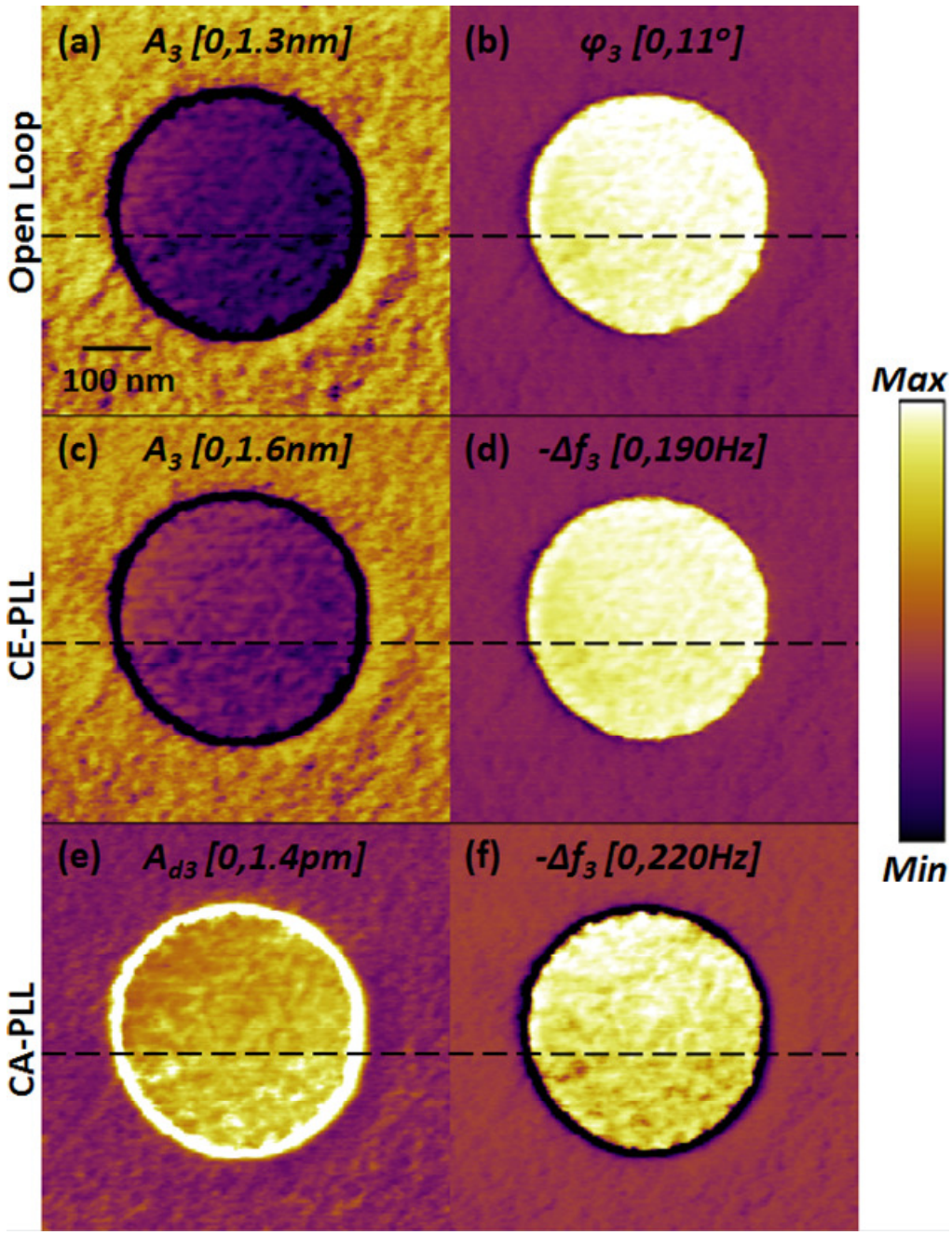

Figure 4-27 *Contrasts obtained on the region marked in previous figure for third eigenmode in open-loop, CE-PLL and CA-PLL modes, respectively, showing (a, b) oscillation amplitude and phase shift contrast, (c, d) oscillation amplitude and negative frequency shift contrast, and (e, f) drive amplitude and negative frequency shift contrast. The operation parameters for imaging were the same as those of figure 4-26. The circular region is the PE polymer with PS polymer surrounding it.*

scanned with third eigenmode in open-loop, CE-PLL and eventually in CA-PLL modes by switching from one mode to another after complete back-and-forth scans of the area in each control mode. To switch, we stopped the scan once the images were obtained in one control mode and retracted the *z*-piezo to its farthest position (without any manual interference), then switched the control mode, engaged the tip on the sample on the PS region and scanned the same area. The imaging was performed at six locations on the sample starting with a large area and zooming in to a small region, with randomized switching among the control modes. This exercise was performed to ensure that the procedure is repeatable and provides same variations at different locations with same materials.

In Figure 4-27, the circular region in the center of each image is the PE polymer and as expected in this region due to very low elastic modulus and much higher dissipation as compared to the surrounding PS region, we observe that: (1) in open-loop mode, the cantilever loses more energy and the oscillation amplitude decreases, whereas the phase shift increases due to the dominant attractive regime, (2) in CE-PLL mode, for the same reasons as the open-loop mode, the oscillation amplitude decreases, and the frequency shift decreases as well (higher attractive forces cause more negative frequency shifts), and (3) in CA-PLL mode, the required drive amplitude increases to compensate for the energy loss and the frequency shift decreases. Furthermore, we recorded the single-point spectroscopy curves (recording output variables in approach-retract curves with respect to the cantilever base position above the sample) in each control mode at same points on both PS and PE polymer regions to understand the influence of first eigenmode amplitude on the mapping of

conservative and dissipative interactions using the third eigenmode. For these measurements, similar to imaging, the higher eigenmode operation was randomly switched among the three control modes. For each case, the cantilever was approached towards the sample until the first eigenmode amplitude reduced to 50 per cent of its free oscillation amplitude and then the *z*-piezo was retracted to the farthest position of the spectroscopy curve distance. In each measurement, the first eigenmode amplitude and phase shift were plotted with the *z*-piezo movement, along with the data from the PLL Pro 2 output channels, which are oscillation amplitude and phase shift for open-loop mode, oscillation amplitude and frequency shift for CE-PLL mode, and drive amplitude and frequency shift for CA-PLL mode. A quantitative comparison of these measurements is shown in the next section. The spectroscopy data was collected at four PE and PS polymer locations on the sample and at each point, in each control mode, 30 curves were recorded while switching randomly between the modes every 10 curves to ensure reproducibility of the data and robustness of the measurement procedure. For example, if the first 10 curves are recorded in CE-PLL mode, the next 10 are in CA-PLL, followed by 10 curves again in CE-PLL and then switching to open-loop and so on. The CE-PLL mode in this example is used as a reference to ensure that the measurements are being taken at the same point. The procedure followed for switching of the control modes is the same as explained above for imaging, *i.e.*, retracting *z*-piezo to its farthest position and changing to a different mode followed by performing a set of spectroscopy measurements. Also, a scan was performed upon complete collection of the data at each point to check for the drift of the tip above the sample.

4.4.2 Quantitative analysis and comparison of higher eigenmode response in open-loop, CE-PLL and CA-PLL control modes

The observed physical variables in the control modes under comparison are different for each mode, as mentioned in the previous section. Therefore, we convert them to virial (V_{ts}) that carries information on conservative tip-sample forces and the average power dissipated (P_{ts}) during tip-sample interaction. The analytical expressions correlating these quantities have been derived and discussed previously and are as follows [77, 78],

$$V_{ts} = \frac{kA}{2}\left[A\left(1 - \frac{f_{exc}^2}{f_o^2}\right) - \frac{A_o \cos\phi}{Q}\right] \tag{4.20a}$$

$$P_{ts} = \frac{\pi f_{exc} kA^2}{Q}\left[\frac{A_o}{A}\sin\phi - \frac{f_{exc}}{f_o}\right] \tag{4.20b}$$

where k is the stiffness, A the instantaneous oscillation amplitude, A_o the free oscillation amplitude, f_{exc} the excitation frequency, f_o the free resonance frequency, φ the phase shift and Q is the quality factor of the higher eigenmode under consideration. The equations are valid for all the three control modes with the appropriate substitutions. For the open-loop mode, f_{exc} is always equal to f_o, whereas the phase is always 90 degrees for CE-PLL and CA-PLL modes, and since the drive amplitude (A_d) is the observed variable in CA-PLL, we replace A_o by QA_d for the calculations. It shall be noted that equations 4.20a and 4.20b are convolutions of tip-sample interactions with tip position and velocity, respectively (as already discussed), and are mathematically independent of each other.

Using these expressions, the virial and dissipated power were calculated for all the single-point spectroscopy curves acquired as discussed in the previous section. For each of the control modes, representative curves are shown in Figure 4-28 and Figure 4-29 on the PS and PE regions, respectively, illustrating the variation of

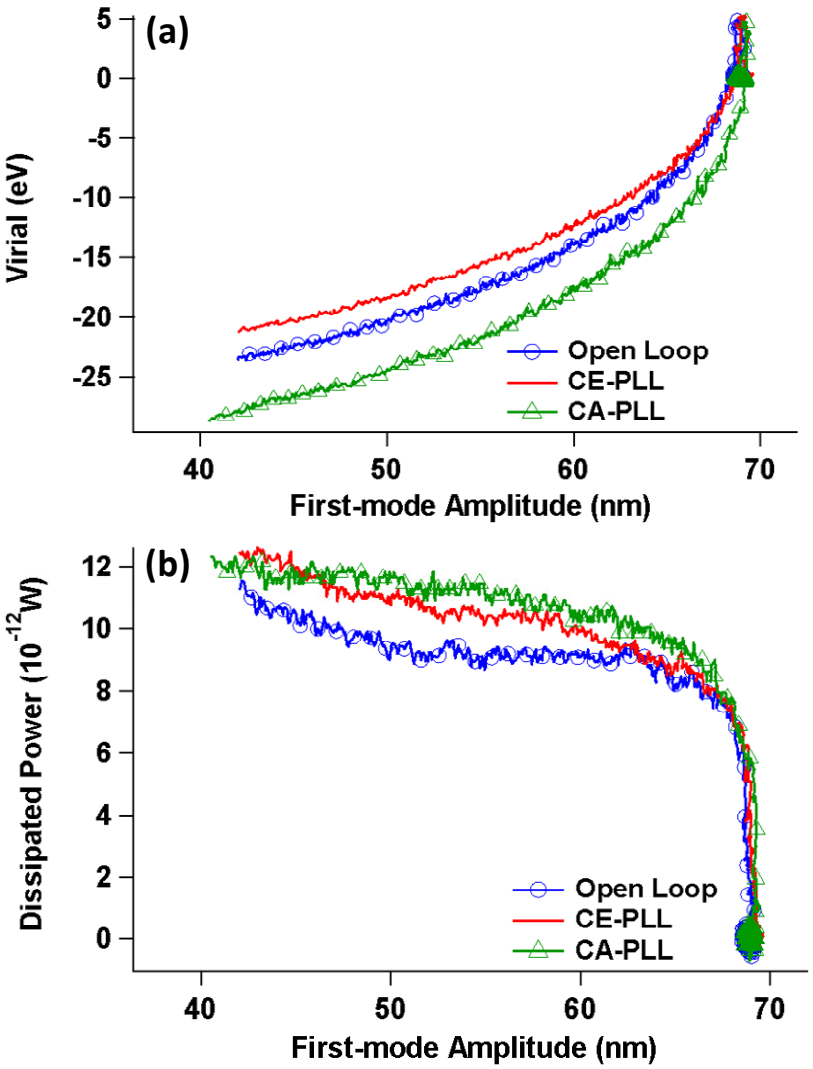

Figure 4-28 *Variation of (a) virials and (b) dissipated powers with fundamental eigenmode amplitude for open-loop, CE-PLL and CA-PLL modes, obtained through single-point spectroscopy curves on the PS polymer region with Young's modulus 2 GPa and low dissipation.*

interaction characteristics with the first eigenmode amplitude. As can be inferred from equation 4.20a, when the dominant tip-sample forces are attractive in nature, the virial is positive because the resulting phase shift is greater than 90 degrees in open-loop mode and the frequency shift is negative in CE-PLL and CA-PLL modes.

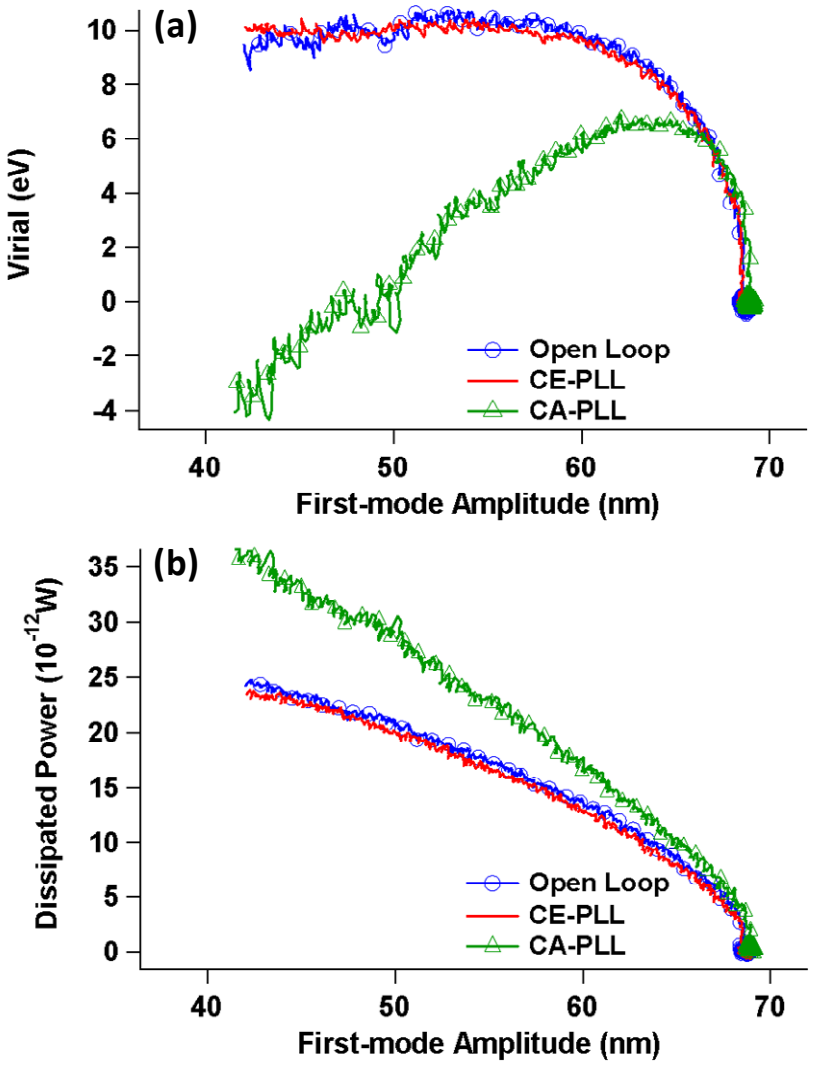

Figure 4-29 *Similar curves as in previous figure obtained on the PE polymer region with Young's modulus 0.2 GPa and high dissipation.*

Conversely, when the tip starts experiencing repulsive forces, the gradient of the virials changes and when the dominant interaction regime is repulsive, the virial becomes negative. In general, the power dissipation is higher on the PE region, as is

known and can be seen in Figure 4-28b and Figure 4-29b. The virials in Figure 4-28a and Figure 4-29a show that in the PS region the attractive tip-sample force regime is characterized by a very small tip displacement, whereas in the PE region, the attractive interaction well extends to a much longer tip-sample interaction distance, which is explained by the order of magnitude difference in the elasticity of two polymers. It shall be noted that the free oscillation amplitude of the fundamental eigenmode for these curves is 80 nm, but when the tip is lowered on the sample, the actual contact between tip and sample is not established until the amplitude reduces to approximately 69 nm. We have ignored the false engage region and the presented results are obtained when the tip is definitely experiencing the short-range tip-sample interactions.

It is observed that for the PS region, the virial for open-loop is nearly equal to that in CE-PLL mode but is more negative for the CA-PLL mode (Figure 4-28a). Power dissipation at the same location, however, is marginally different from one another for all three control modes, for a given fundamental eigenmode amplitude (Figure 4-28b). Also, the change in virial and dissipated power slows down with the decrease in amplitude once the tip transitions to the repulsive region. On the other hand, in the PE region, the tip motion is dominated by attractive tip-sample forces for open-loop and CE-PLL modes and the repulsive region is explored only in the CA-PLL mode, as shown in Figure 4-29a. Furthermore, it can be seen in Figure 4-29b that the power dissipated by the third eigenmode when operated in CA-PLL mode is much higher than for the other two control modes. These trends in the virials and dissipated powers for the higher eigenmode can be attributed primarily to three factors (1) the

operation is at a constant drive amplitude in open-loop and CE-PLL modes and the response variables are free to vary when the tip starts interacting with the sample, exhibiting similar responsiveness to the conservative and dissipative interactions for these control modes, (2) in CA-PLL mode, on the other hand, the response amplitude is forced to be constant by varying the drive, resulting in relatively higher tip penetration into the sample and therefore, higher repulsive forces, (3) however, if the sample is hard (PS region in this case), the fact that the tip penetration into the sample and consequently the peak tip-sample forces do not change significantly after the transition to the repulsive regime, it results in smaller variations in response past the transition.

In order to verify the validity of above observations during actual imaging of the sample, shown in Figure 4-30b and Figure 4-30c are the virial and dissipated power variations for the three control modes along a section of the images shown in Figure 4-27 (along the dashed line). Figure 4-30a shows the height trace along the selected section. The lower height trace on the ends represents the PS region with the PE region in the center. It is observed that for both the PS and PE polymers, the variation of the virial along the section for open-loop and CE-PLL control modes is nearly the same, whereas CA-PLL demonstrates a higher influence of repulsive interactions (or smaller attractive forces). Power dissipation, on the other hand, is the same for all control modes on the PS region, but is higher for CA-PLL mode in the PE region, as inferred from the spectroscopy results. Therefore, the variation of virials and dissipated power obtained during the sample imaging is in agreement with the observations of the single-point spectroscopy results.

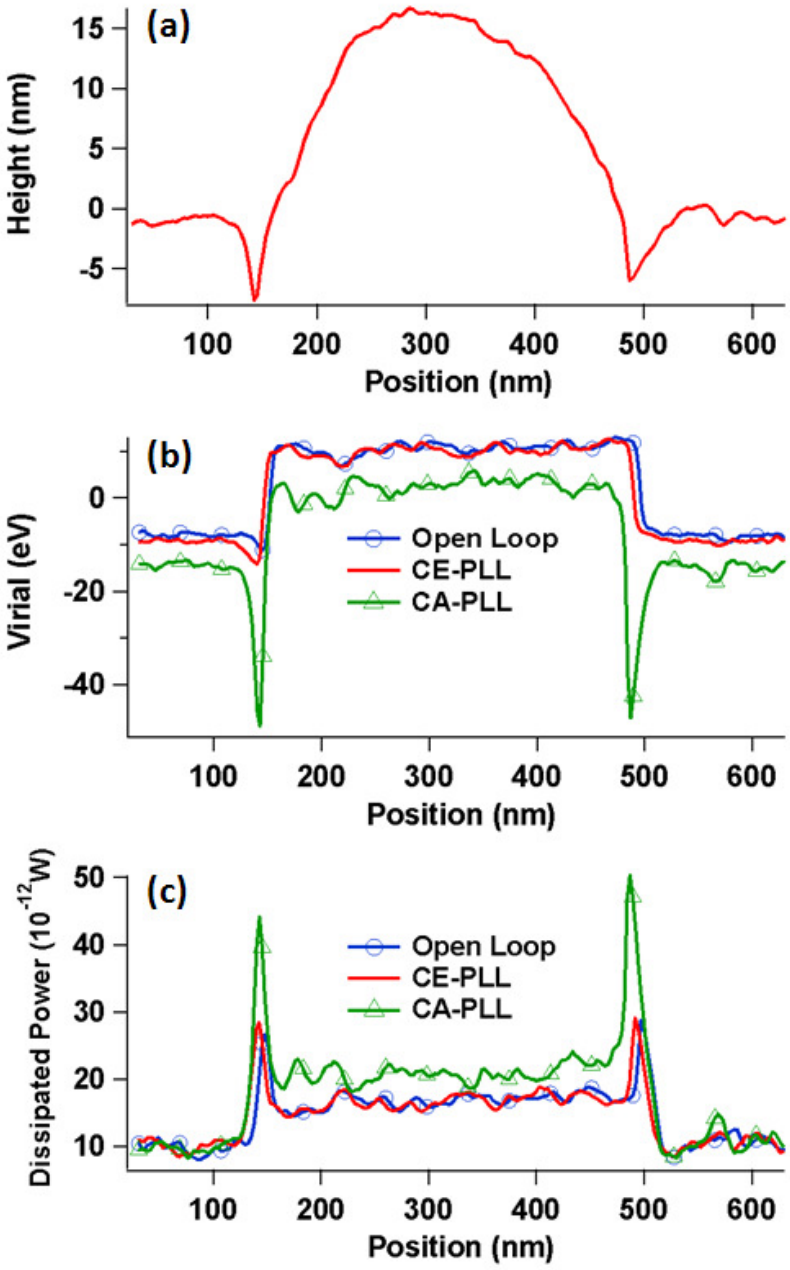

Figure 4-30 *Variation of (b) virials and (c) dissipated powers for open-loop, CE-PLL and CA-PLL modes along the marked section in figure 4-27. Figure (a) shows the height trace along the section with PE polymer in the higher region.*

4.4.3 Applications of open-loop, CE- and CA-PLL modes

From the analytical expressions for virial and dissipated power shown above in the equation set 4.20, it can be deduced that for open-loop and CE-PLL modes, the conservative and dissipative interactions are coupled and influence both response variables, *i.e.*, amplitude and phase, and amplitude and frequency shift, respectively. For the CA-PLL mode, however, with response amplitude being constant, the frequency shift directly maps the conservative interactions and even though change in drive and frequency shift terms both appear in the dissipative component, if the frequency shift is considerably smaller than the free resonance frequency, the change in drive can be directly used to map dissipation. This means that although the information obtained in any of the three control modes can be separated into conservative and dissipative channels, operating a higher eigenmode in CA-PLL mode provides direct output channels to map the tip-sample interaction contrast while the fundamental eigenmode captures the topographical information. Another important point to consider during imaging is that since the tip typically penetrates into higher repulsive force regions when operated in CA-PLL mode, open-loop or CE-PLL mode controls may be more suitable where soft mechanical contact between the tip and the sample is desired.

4.4.4 Summary

In summary, we have explored open-loop, CE-PLL and CA-PLL modes for the higher eigenmode control in bimodal AFM and their applications in mapping the tip-sample interactions [99]. A quantitative comparison of virial of interactions and

dissipated power for the three control modes has been presented. The results establish that the open-loop and CE-PLL modes provide the same quantitative information about the conservative and dissipative interactions, and the CA-PLL mode scans a broader range of interactions. The quantitative difference in the CA-PLL mode response from the other two control modes becomes pronounced for softer samples.

As mentioned before, such implementation of a higher eigenmode in frequency-modulated control has not been explored before for bimodal AFM operation in air, therefore, this study provides guidelines for their use in the future. This undertaking was inspired from a new trimodal imaging technique that we experimentally developed by driving three eigenmodes of a cantilever, whereby topography, phase shift and frequency shift were simultaneously acquired. The trimodal operation will be discussed in detail in the next section and this work was an effort towards its quantitative understanding.

5. Experimental development of trimodal AFM characterization method

As discussed in chapter 2, the bimodal AFM imaging operation has been incorporated under two control methods, 1) in intermittent-contact mode in air by driving fundamental eigenmode and a higher eigenmode with a fixed drive amplitude at their free resonance frequencies, 2) by simultaneously controlling two eigenmodes in frequency-modulation controls using parallel phase-locked-loop (PLL) circuits, thereby maintaining the drive frequency at its effective resonance. In this section, a trimodal AFM characterization technique is presented, where three eigenmodes of a cantilever are excited and controlled, combining the knowledge of the two bimodal operations and extending the PLL control of a higher eigenmode to imaging in ambient air [102]. The trimodal operation provides channels for simultaneous acquisition of topography using the fundamental eigenmode response, and phase and frequency shift contrast from the higher eigenmode responses with a single surface scan. The first cantilever eigenmode is controlled using standard amplitude-modulation (AM) AFM to acquire the sample topography and a phase contrast. A second eigenmode is excited with a smaller amplitude at constant frequency and drive, using its phase as an additional contrast signal, similar to tapping-mode bimodal operation. Finally, a third eigenmode, also excited with a relatively small amplitude, is controlled in the PLL mode, using its frequency shift relative to the free resonance frequency as the contrast signal. One of the important potential applications and motivations of obtaining these contrasts is quantitative

measurements of the conservative and dissipative tip-sample interaction forces [99, 103].

The new aspects of this method are, (1) the utilization of PLL mode for a secondary motion that explores a large tip-sample interaction force range, including highly attractive, highly repulsive and local dissipation forces, as dictated by the relatively large (tens of nanometers) oscillation amplitude of the first eigenmode (as opposed to the typical PLL mode operation in noncontact vacuum mode, where the vertical distance sampled by the cantilever tip in is on the order of a few nm and generally it remains in the region of attractive tip-sample forces), and (2) the simultaneous excitation of three cantilever eigenmodes, which allows the side-by-side comparison of the frequency shift contrast with the phase contrast, in addition to other secondary signals such as the amplitude error of the fundamental eigenmode and the amplitudes of the higher eigenmode signals. In this section, the general dependence of phase shift and frequency shift on tip-sample interactions is explained theoretically and through simulations, followed by the experimental development of the technique with the imaging results.

5.1 Computational and theoretical framework

To explore the behavior of the frequency shift and phase of the higher eigenmodes through simulations, we constructed a 3-eigenmode model of a rectangular cantilever using the well-known Euler-Bernouilli beam equation [81],

$$\rho A\ddot{u}(x,t) + D\dot{u}(x,t) + (EIu''(x,t))'' = -F_{ts}(Z_c - u(L,t))\delta(x-L) \tag{5.1}$$

where ρ, A and L are, respectively, the mass density, cross-section and length of the beam, EI is its flexural rigidity, Z_c is its rest position above the sample, F_{ts} is the tip-sample interaction force acting at the tip and x is the position along the length of the beam, with $x = 0$ being located at the base. $u(x,t)$ is the total time-dependent deflection and satisfies the boundary conditions

$$u(0,t) = y_1 \cos(2\pi\nu_1 t) + y_2 \cos(2\pi\nu_2 t) + y_3 \cos(2\pi\nu_3 t) \tag{5.2a}$$

$$u'(0,t) = u''(L,t) = u'''(L,t) = 0 \tag{5.2b}$$

where y_1, y_2 and y_3 are the spatial base excitation amplitudes applied to each eigenmode, respectively, which can be adjusted to achieve the desired free response amplitudes, and ν_1, ν_2 and ν_3 are the excitation frequencies applied to each of the eigenmodes. The value ν_1 is kept fixed at the fundamental free resonance frequency in all cases, as required in the AM-AFM mode operation. The mathematical details of the solution of the fourth-order differential beam equation 5.1 have been discussed in section 4.1. The beam has been modeled with the properties similar to those of an Olympus AC240TS cantilever [101] (dimensions 240 μm x 30 μm x 2.7 μm; force constant k = 1.6 N/m; eigenfrequencies ν_1 = 60.8 kHz, ν_2 = 380.8 kHz and ν_3 = 1.07 MHz; fundamental quality factor Q = 150), in order to allow direct comparison with experiments. We modeled the conservative portion of the tip-sample interaction forces using the Hamaker equation for the long-range attractive forces, and the Derjaguin-Müller-Toporov (DMT) model for the contact forces [2, 104],

$$F_{ts}(z) = -\frac{HR}{z^2}, \qquad z \geq a_o \tag{5.3a}$$

$$F_{ts}(z) = -\frac{HR}{a_o^2} + \frac{4}{3}E^*\sqrt{R}(a_o - z)^{3/2}, \qquad z < a_o \tag{5.3b}$$

where a_o = 0.2 nm, is the minimum tip-surface approach distance in the attractive regime, H = 2 x 10^{-19} J, is the Hamaker constant, R = 10 nm, is the probe radius of curvature (as specified for AC240TS), E^* is the effective elastic modulus calculated from tip and sample elastic moduli and z is the instantaneous tip-sample distance. In order to simulate the dissipative effects, local tip-sample dissipation was incorporated through the viscoelastic model introduced by Gotsmann and coworkers [11], in which the dissipative force, F_{diss}, is proportional to the tip velocity, with an exponentially decaying proportionality constant,

$$F_{diss} = \gamma_o e^{-(z_{tip}/z_o)} \frac{dz_{tip}}{dt} \tag{5.4}$$

with dissipation coefficient γ_o = 1.25 x 10^{-7} Kg/s and z_o = 0.75 nm. By integrating numerically the three coupled cantilever eigenmode equations with the above parameters for different cantilever heights above the sample, as well as varying excitation amplitudes for the three eigenmodes, we explored the change in the contrast of the phase signal of the first eigenmode controlled with AM-AFM, the phase of the higher eigenmode excited in open loop, and the frequency shift of the higher eigenmode controlled in the PLL mode.

The behavior of the phase and frequency shift is first explored for bimodal operation using the tip-sample force curves similar to that shown in Figure 5-1, which illustrates the conservative and local dissipative interactions, with the arrows indicating the force-distance trajectory followed by the tip. For ease of interpretation, the dissipative forces shown on this graph were calculated without excitation of the

higher eigenmodes. The total force curve clearly shows hysteresis, indicating that local tip-sample dissipation removes energy from the oscillating cantilever.

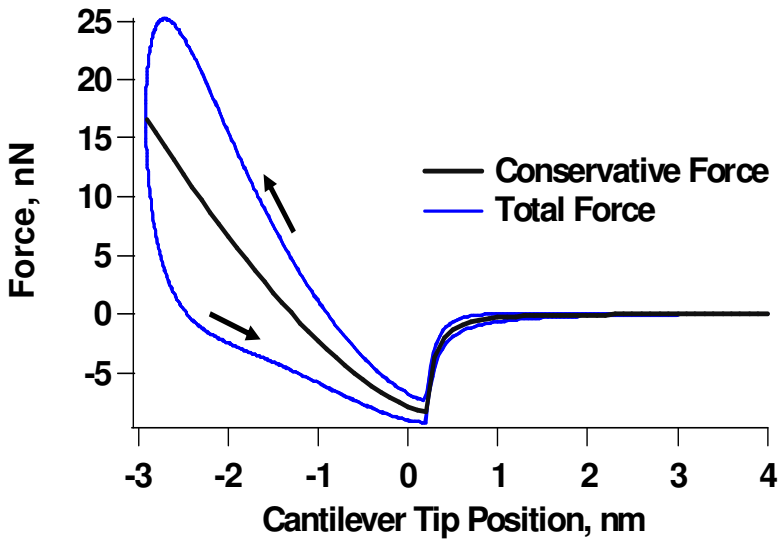

Figure 5-1 *Simulated conservative and total (conservative plus dissipative) tip-sample interaction force curve for a cantilever tapping on a viscoelastic sample in standard AM-AFM with a free amplitude and amplitude setpoint of 100 and 70 nm, respectively. Reprinted with permission from Santiago D. Solares and Gaurav Chawla, J. Appl. Phys., 108, 054901, (2010). Copyright 2010, American Institute of Physics.*

Figure 5-2a illustrates the typical dissipation-free behavior computed for the fundamental phase and that of the second eigenmode, when excited at constant drive and frequency during the cantilever approach towards the sample, and compares it to the behavior of the negative of the frequency shift of the same (second) eigenmode when its phase is locked to 90 degrees. As the chart shows, the trends are very similar, suggesting that the phase and frequency shift should vary proportionally in opposite directions when two eigenmodes are excited. Figure 5-2b compares the phase and frequency shift curves of the second eigenmode to the results obtained by introducing a dissipative force behaving as illustrated in Figure 5-1. In all cases,

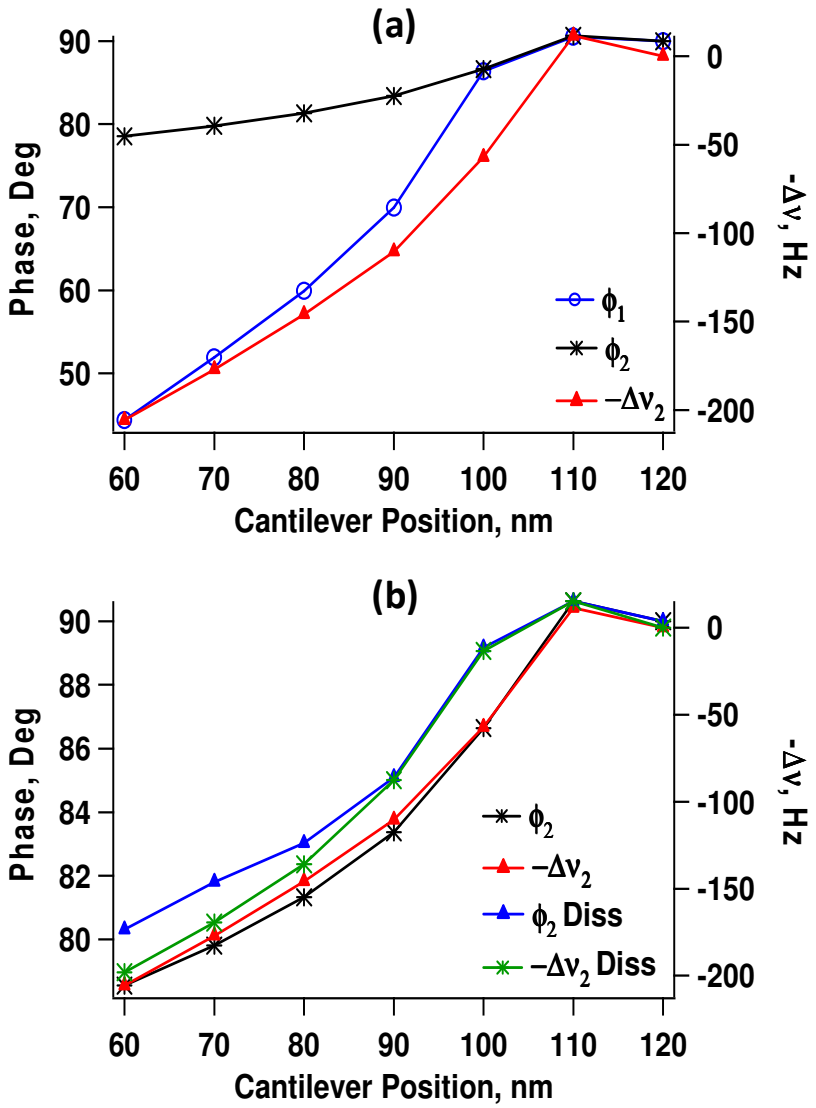

Figure 5-2 *(a) comparison of the behavior of the fundamental eigenmode phase (φ_1) to the second eigenmode phase (φ_2) and the* negative *of the second eigenmode frequency shift ($-\Delta\nu_2$) for bimodal operation, as a function of cantilever equilibrium position, in the absence of dissipation; (b) comparison of the behavior of the second eigenmode phase and frequency shift in dual-frequency operation with and without local tip-sample dissipation. The data was acquired by simulating the cantilever response with the first eigenmode controlled in AM-AFM mode, and the second eigenmode either in open-loop or PLL mode. The fundamental and second eigenmode free oscillation amplitudes were 100 and 6.5 nm, respectively. The sample modulus of elasticity was 1 GPa and coefficient of dissipation, γ_o=7.5x10^{-8} kg/s. Reprinted with permission from Santiago D. Solares and Gaurav Chawla, J. Appl. Phys., 108, 054901, (2010). Copyright 2010, American Institute of Physics.*

the phase and frequency shift responses are very similar. While the result of Figure 5-2b is not intended to define a universal trend on the effect of dissipation on the phase or frequency shift, it suggests that the relationship between them is in general preserved, although deviations are observed for the lowest cantilever positions. This is remarkable considering that the dissipation forces can significantly alter the dynamics of the system: they change the level of tip penetration into the sample, which reduces the oscillation amplitude of the fundamental eigenmode, which in turn changes the force gradient trajectory (and its time average) experienced by the higher eigenmode in a non-trivial manner.

The relationship between the phase and the frequency shift observed through the simulations can be easily explained for a single eigenmode using a harmonic oscillator model, whose frequency dependent response follows a Lorentzian curve (Figure 5-3a) with maximum amplitude at the resonance frequency. It is well known that the phase of the oscillator's response, φ, is described by the equation,

$$tan\varphi = \frac{\omega\omega_r/Q}{\omega_r^2 - \omega^2} \tag{5.5}$$

where ω and ω_r are the excitation and resonance angular frequencies, respectively. Furthermore, as mentioned in chapter 2, the angular resonance frequency is related to the *effective* force gradient experienced by the oscillator through the relationship,

$$\omega_r = \sqrt{\frac{k - \langle \nabla F_e \rangle}{m}} \tag{5.6}$$

where k is the oscillator force constant, F_e the external force (tip-sample force in this case) and m its effective mass. Substituting equation (5.6) into equation (5.5) and

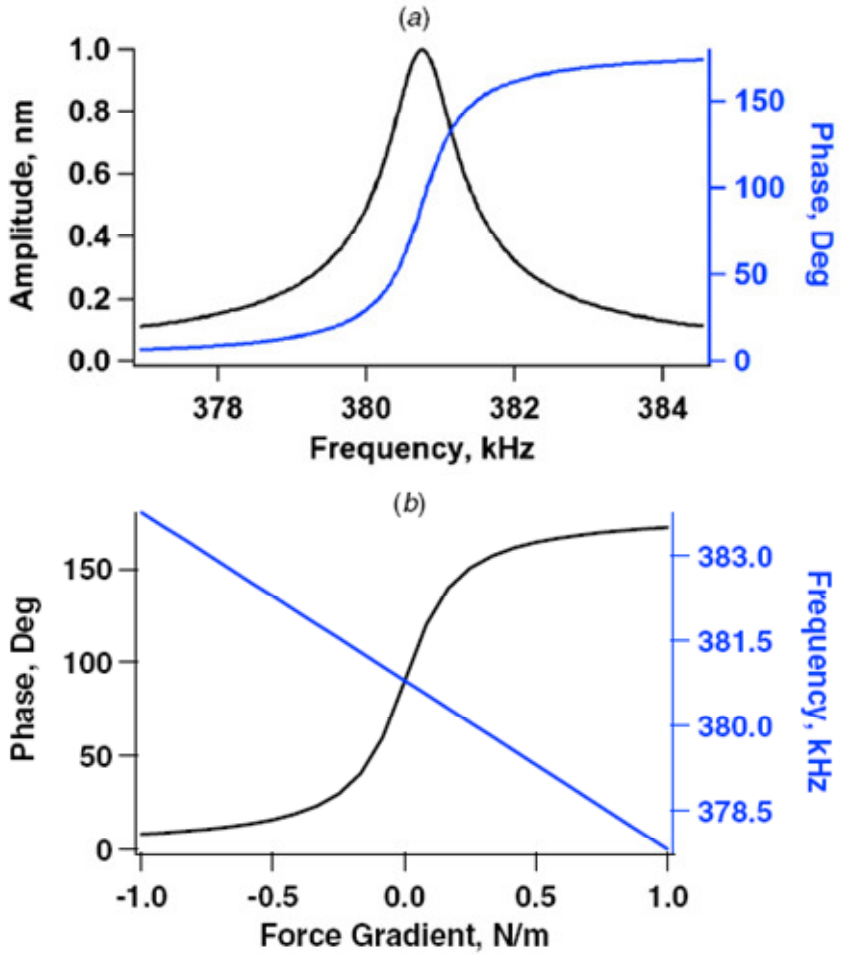

Figure 5-3 *Ideal response for the second eigenmode of the cantilever used in the simulations: (a) amplitude and phase versus excitation frequency, and (b) phase and frequency shift versus effective force gradient. The phase curve in (b) corresponds to excitation at the free resonance frequency.*

setting the excitation frequency to be equal to the resonance frequency, a relationship between the response phase and the effective force gradient is obtained, which is plotted in Figure 5-3b together with the effective resonance frequency, as a function of the force gradient for the second cantilever eigenmode [2]. The result indicates that the phase and frequency shift vary in opposite directions with respect to the average force gradient experienced by the oscillator.

The behavior of the phase and frequency shift is more complex when all three eigenmodes are active, since each oscillation influences the effective force gradient that each eigenmode experiences and not all eigenmodes experience the same effective force gradient (this is because the force gradient of each eigenmode is given by dF_e/dz_i, where z_i is the instantaneous displacement with respect to equilibrium of that particular eigenmode, which oscillates differently than the cantilever tip position and the displacement coordinates of the other eigenmodes). Depending on the oscillation amplitudes, the changes observed in each eigenmode's response due to changes in the imaging parameters or sample properties can be different from one another, even ranging from nearly parallel to nearly antiparallel in some cases, although regions can often be found where they follow similar trends. This is illustrated in Figure 5-4, which shows the phase response behavior of the first three eigenmodes as a function of cantilever position: in the absence of local dissipation, when the second and third eigenmode amplitudes are 5 nm (Figure 5-4a) and 1 nm (Figure 5-4b), and in the presence of dissipation when the amplitude are 5 nm (Figure 5-4c).

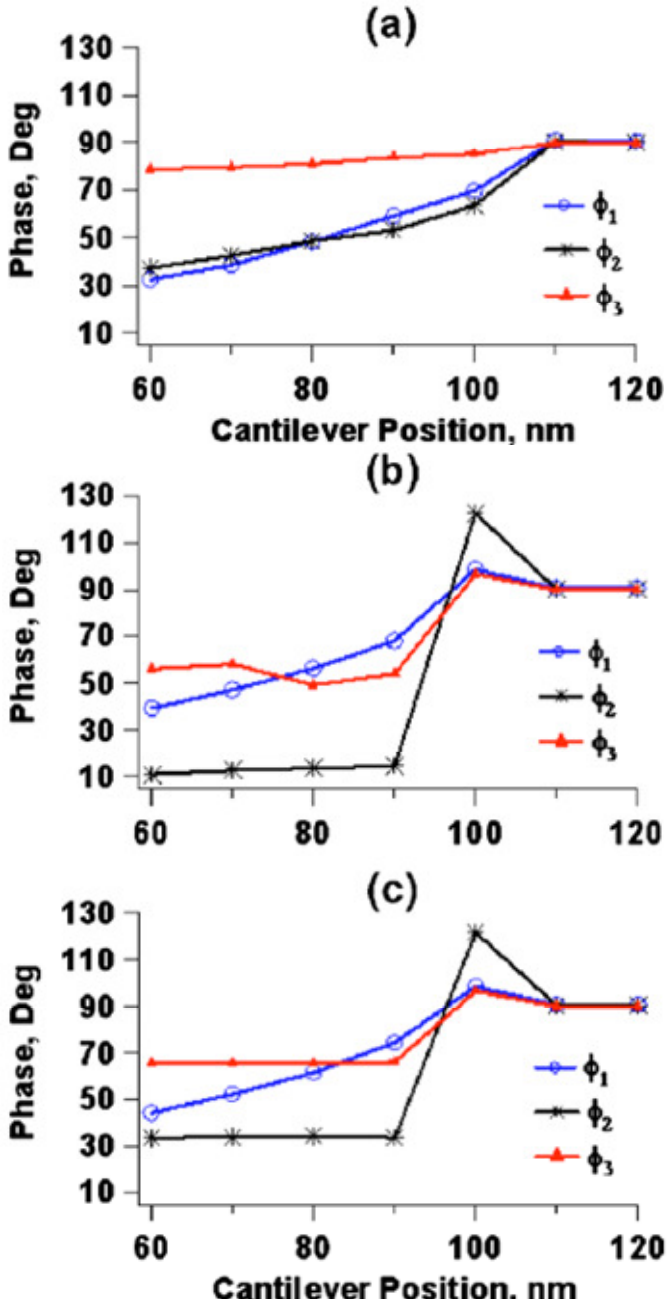

Figure 5-4 *Simulated phase response of the first three cantilever eigenmodes as a function of the cantilever position in the absence of local dissipation using a free oscillation amplitude of 100 nm for the first eigenmode and 5 nm (a) and 1 nm (b) for the second and third eigenmodes; (c) similar results for second and third eigenmode oscillation amplitudes of 5 nm in the presence of dissipation. The sample modulus of elasticity was 1 GPa and coefficient of dissipation,* $\gamma_o = 7.5 \times 10^{-8}$ *kg/s. Reprinted with permission from Santiago D. Solares and Gaurav Chawla, J. Appl. Phys., 108, 054901, (2010). Copyright 2010, American Institute of Physics.*

5.2 Experimental trimodal AFM: implementation, results and discussion

The experimental trimodal operation is schematically illustrated in Figure 5-5. The experiments were conducted on the MFP3D AFM, by utilizing its capability to perform bimodal tapping-mode characterization (we operated either the first and

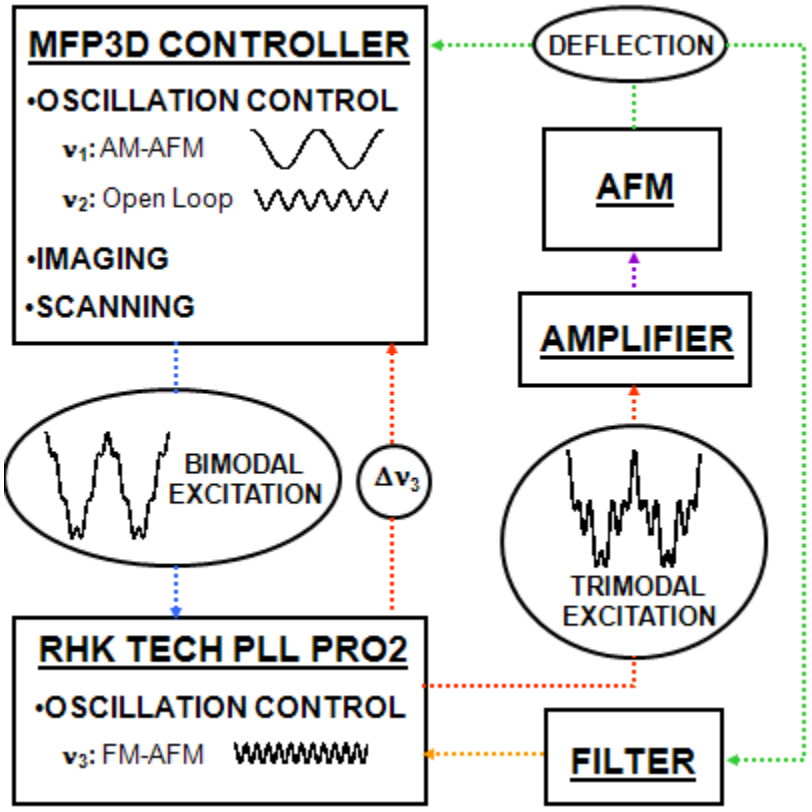

Figure 5-5 *Controls schematic. Phase and frequency shift contrast were acquired interchangeably using the second and third eigenmodes.*

second, or the first and the third eigenmodes using this mode), and interfacing it with the PLL Pro 2 controller that controls an additional eigenmode in open-loop mode or PLL mode. The start-up operation consisted of (1) tuning two cantilever eigenmodes

to operate at their free resonance frequencies and at the desired amplitude in the MFP3D controller bimodal AFM mode, (2) independent external tuning of a higher eigenmode to operate in open-loop and PLL modes (this was accomplished by sending the cantilever deflection signal through an output port on the MFP3D controller to the PLL Pro 2 controller via a bandpass filter around the higher eigenmode frequency, and receiving the excitation signal generated by the PLL Pro 2 controller through an input port on the MFP3D controller, which was connected to the cantilever shaker), (3) connecting the bimodal excitation signals through an output port of the MFP3D controller to the PLL Pro 2 controller, in order to be added as a bias to the PLL excitation signal, and (4) input the combined triple frequency excitation signal back into the MFP3D controller to be transmitted to the cantilever shaker, as described for step 2 above. The details of each of these operation modes, along with the connections among the instruments, are provided in section 4.2. Imaging was stably performed at normal AM-AFM scan rates upon completion of these steps. Throughout the experiments the PLL phase shift was also monitored to ensure that the oscillation phase remained locked for the frequency-modulated control, that is, the fluctuations of the phase are within the noise level to maintain the resonance operation. The bimodal tapping mode response signals were processed internally by the lock-in amplifiers in the MFP3D controller to obtain their oscillation amplitudes and phase shifts, and the frequency shift signal was received from the PLL Pro 2 controller through an additional input port for plotting. We conducted a variety of experiments using the first three eigenmodes, varying the amplitudes of the three excitation signals, as well as alternating the PLL-controlled oscillation between the

second and the third cantilever eigenmodes. We also conducted bimodal experiments using only one higher eigenmode in addition to the fundamental vibration, either PLL-controlled or in open-loop. The possibility of controlling the higher eigenmodes in PLL and open-loop modes inspired us to perform a quantitative comparison of these control schemes to understand their individual merits, as has been discussed in section 4.4 with respect to the bimodal operation.

The cantilever used for the experiments is an Olympus AC240TS [101] on a phase calibration standard sample (Asylum Research, SEBS KRATONTM G-1652 thermoplastic rubber triblock copolymer with polystyrene end blocks and poly(ethylene-butylene) mid block). Figure 5-6 shows the variations of phase and frequency shift with the cantilever base position above the sample at a fixed horizontal position. As seen in the previous section through simulations, experimental curves also exhibit parallel behavior between the three eigenmodes, as well as partially parallel and anti-parallel behavior, depending on the imaging parameters and the sample properties. Figure 5-6a shows a case in which the phases of the first three eigenmodes vary in the same direction. With the third eigenmode in PLL mode, Figure 5-6b shows that the phase of the first two eigenmodes and the frequency shift of the third eigenmode are parallel in one region and anti-parallel in another (note that the negative of the frequency shift has been plotted). Finally, Figure 5-6c shows a case in which the responses of the first and third eigenmodes are antiparallel, while the response of the second eigenmode does not exhibit significant variation. Such rich behavior is not surprising if one considers the complexity of the tip interaction with the sample as a result of superposition of the responses of three eigenmodes.

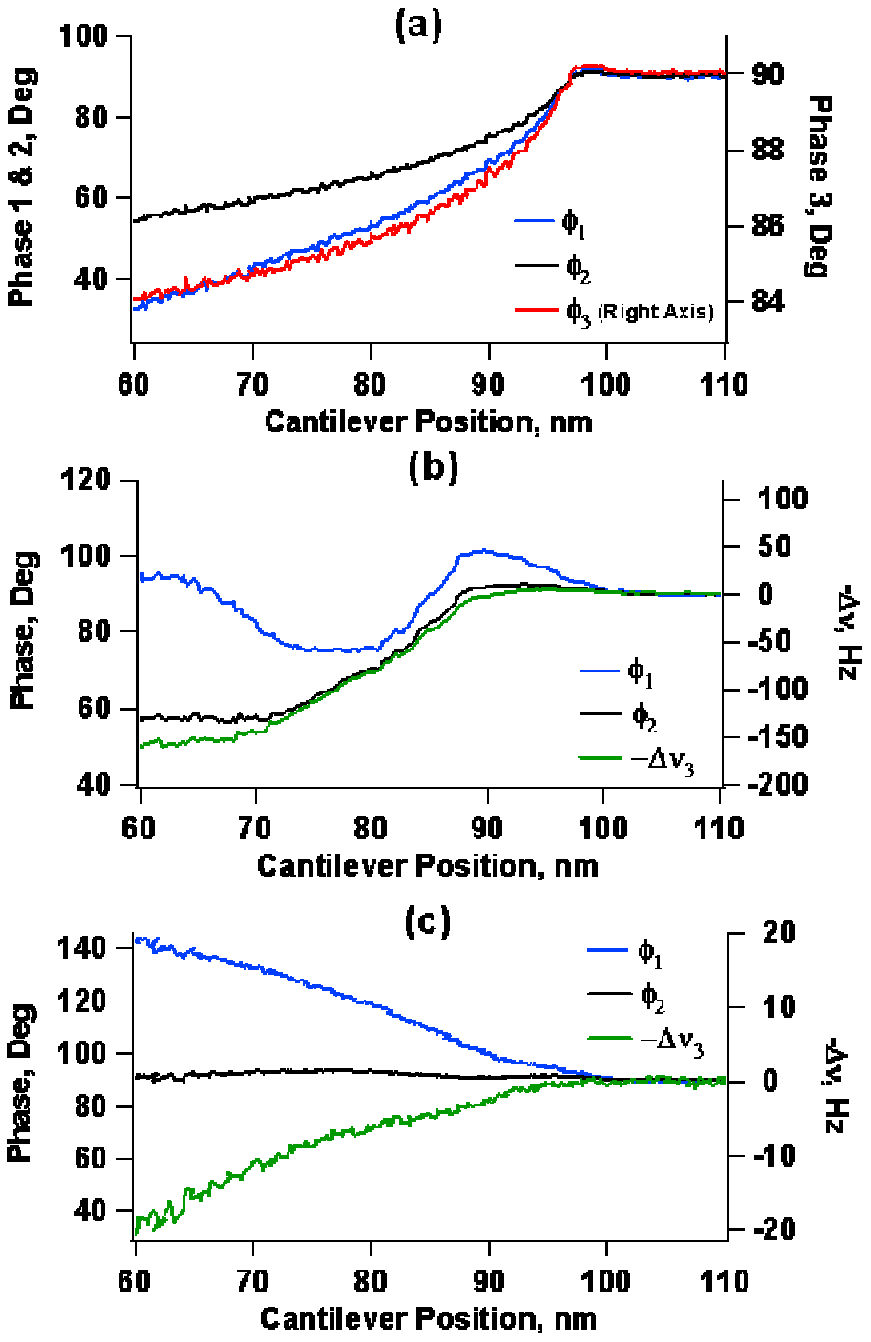

Figure 5-6 *Examples of experimental frequency and phase curves acquired on SEBS KRATON^{TM} G-1652 thermoplastic rubber triblock copolymer with polystyrene end blocks and poly(ethylene-butylene) mid block sample using an AC240 cantilever with $A_{1\text{-}o}$ = 100 nm, $A_{2\text{-}o}$ ~ 10 nm, and $A_{3\text{-}o}$ ~ 10 nm.*

The trends observed in the higher eigenmode responses can be explained by considering the effects of operation and surface parameters, such as oscillation amplitudes, elastic and inelastic properties of the surface. Typically, smaller oscillation amplitudes exhibit higher sensitivity to the tip-sample interactions, which can be explained by the dimensionless equation of motion of a damped harmonic oscillator under the influence of external (tip-sample) forces. In doing this, the external forces are normalized by the product of the force constant and the amplitude (kA). This indicates that for a given force constant, the oscillator becomes less sensitive to external forces as its oscillation amplitude increases, or if the amplitude is the same, as the eigenmode order increases, it will experience lower effective force gradients due to its higher force constant. In our experiments, however, we observed that the trimodal motion becomes unstable if the amplitude of higher modes is decreased significantly (less than ~5 nm). This can be due to the fact that the small amplitudes increase the contact time of the tip with the sample and also result in reduced restoring force. Therefore, even though imaging with low amplitude values is favored for high sensitivity, it may not be suitable with regard to the stability. Figure 5-7 shows an image where the trimodal motion has been achieved by open-loop control of the third eigenmode using the PLL Pro 2, combined with the tapping-mode bimodal operation of first and second modes in the AFM. The phase shifts obtained for three modes have been superimposed on the topography for comparison. Here, we were able to achieve similarly sharp contrasts even with fairly large higher mode amplitudes (~15 nm), which is also favored for the stability. These behaviors may also contain the influence of other competing surface effects, as will be discussed.

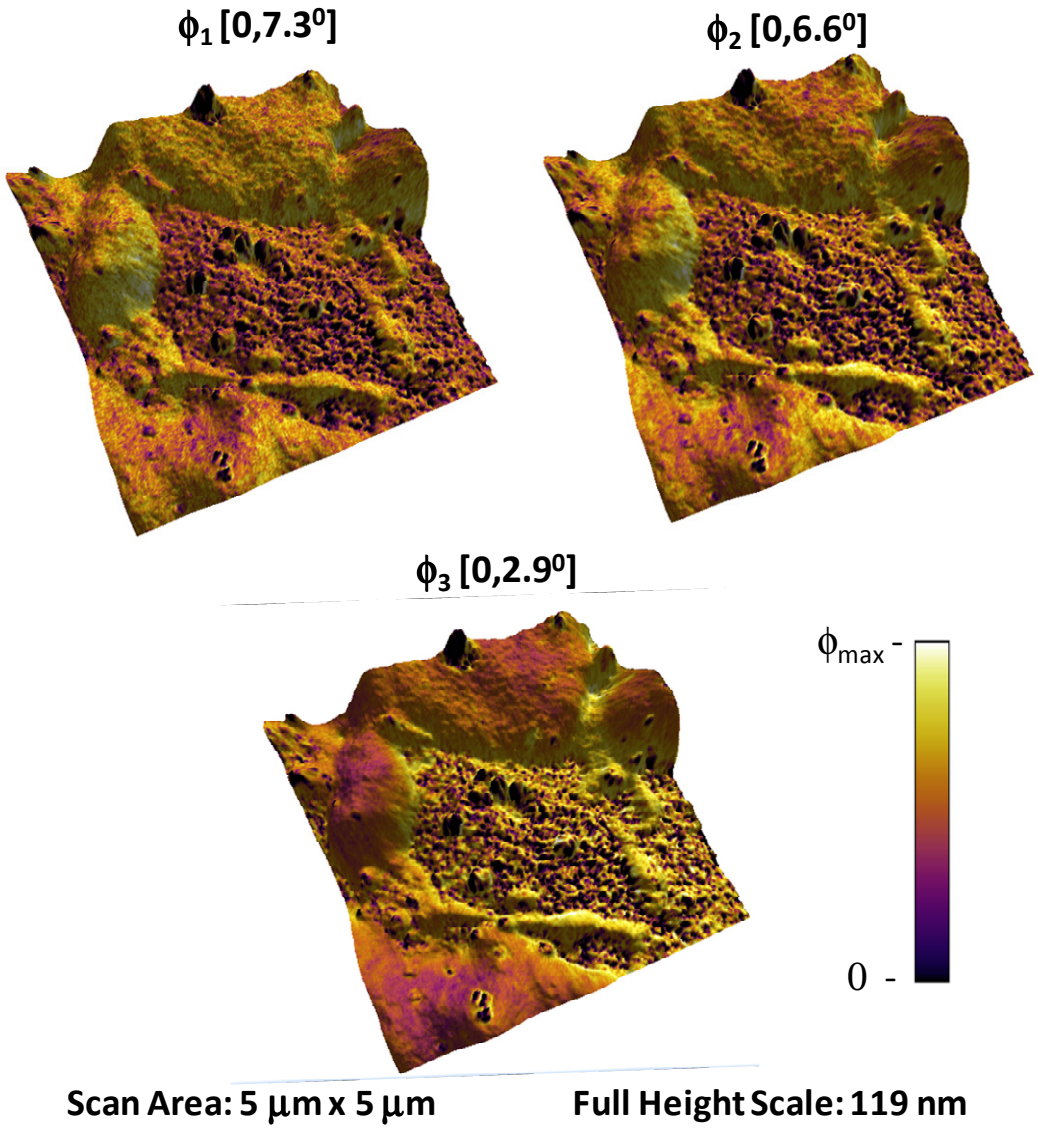

Figure 5-7 *Simultaneous first, second and third eigenmode phase contrast (color scale) superimposed on the topography. The phase scale ranges were determined by the maximum and minimum values measured during the scan, with zero corresponding to the lowest value measured. The first three cantilever eigenfrequencies were 73.5 kHz, 436.3 kHz and 1.184 MHz, respectively, and the fundamental force constant ~1.9 N/m. The eigenmode free oscillation amplitudes were approximately 100, 15 and 15 nm, respectively, with an amplitude setpoint of 63 nm. The scan velocity was 5 µm/s. Reprinted with permission from Santiago D. Solares and Gaurav Chawla, J. Appl. Phys., 108, 054901, (2010). Copyright 2010, American Institute of Physics.*

When one of the higher eigenmodes is operated in PLL mode in order to obtain the frequency shift contrast during imaging, in general the experimental images agreed with the expected behavior in that the frequency shift and phase contrast are inversely related, as illustrated in Figure 5-8 (note that in order to allow a direct comparison with the phase contrast, the experimental images display the *negative* of the frequency shift). However, in many cases differences were observed, as anticipated from the trends seen in Figure 5-6. For example, it can be seen in Figure

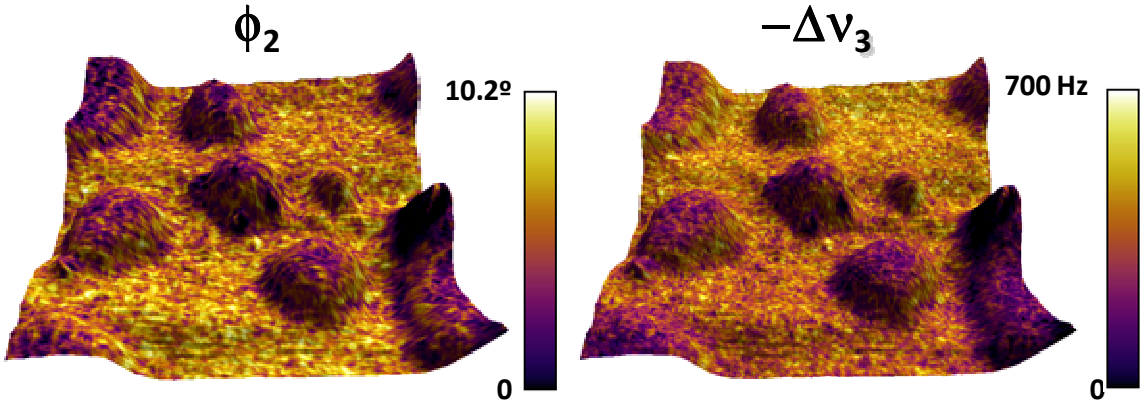

Figure 5-8 *Second eigenmode phase contrast and third eigenmode frequency shift contrast (color scale) superimposed on the sample topography (these images were taken at a different location than the images of previous figure). Note that the graphs show the negative of the frequency shift. The imaging parameters were* $A_{1\text{-}o}$ *= 100 nm,* $A_{1\text{-}setpoint}$ *= 70 nm,* $A_{2\text{-}o}$ *~ 8.5 nm,* $A_{3\text{-}o}$ *~ 5.5 nm, scan speed = 5µm/s.*

5-9 that the variations in the phase throughout the sample are not as sharply segregated as those displayed by the frequency shift. These images have been obtained at different locations on the same sample as Figure 5-7 using the same cantilever, but with different operation parameters. One of the possible reasons for these differences is again the different oscillation amplitudes for the two cases resulting in variations in sensitivity.

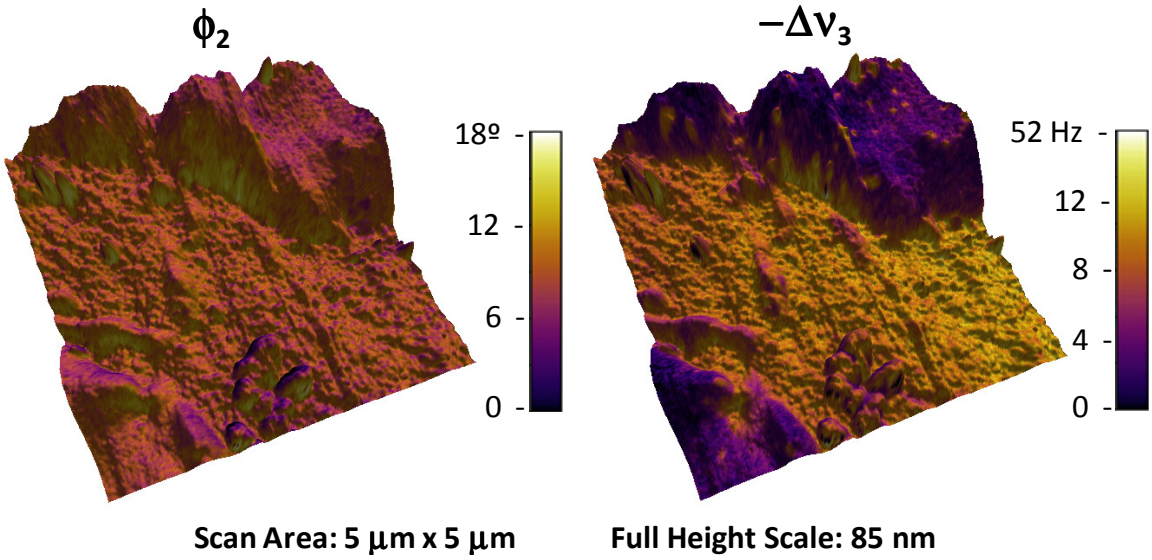

Figure 5-9 *Similar images as the previous figure taken at a different location on the sample. The three eigenmode free oscillation amplitudes were approximately 100, 10 and 10 nm, respectively, and the amplitude setpoint was 70 nm. The scan velocity was 5 µm/s. Reprinted with permission from Santiago D. Solares and Gaurav Chawla, J. Appl. Phys., 108, 054901, (2010). Copyright 2010, American Institute of Physics.*

In our trimodal experiments, the drive amplitude for the higher eigenmodes was fixed for both open-loop and PLL mode operations, which means that the oscillation amplitude is allowed to change as a result of interactions and consequently, the phase and frequency shift curves in Figure 5-6 and the contrasts seen in the Figures 5-8 and 5-9 are a result of coupled conservative and dissipative interactions. To first understand the effects of only the conservative interactions, we assume a sample with constant dissipation. For this case, the elastic properties of the surface will govern the nature of the dominant forces on the tip motion. A very soft sample will result in attractive region extending over a large range of tip motion causing the response to be effectively influenced by the attractive forces. On the other hand, a hard sample will cause very strong mechanical impact between the tip and the sample, resulting in

large repulsive forces. Considering the complexity of the tip motion resulting from the superposition of three eigenmodes, highly repulsive interactions and can cause strong perturbations in the motion and can easily induce severe instabilities in the motion. This is due to the fact that each eigenmode has a different mode shape (curvature) and their frequency-ratios are non-integral, which means that the tip-sample interaction force trajectory is expected to be different for every tip-sample impact, causing the motion to never truly reach a steady state. In addition to this, superimposing higher eigenmode amplitudes on the fundamental motion for imaging causes the tip to penetrate deeper into the sample, which can lead to stronger coupling of the eigenmodes through the non-linear forces.

Furthermore, another effect of tip penetration into the highly repulsive regions (due to large amplitudes, small setpoint amplitude or very hard sample) can be that the resulting frequency shifts of the higher modes are so large that the excitation at the free resonance (as is the case for open-loop control, where the drive frequency is fixed) corresponds to a region of the response curve where the slope of the phase response is nearly flat (as can be seen in Figure 5-3a). This will result in no observable phase variation in the images, as may be the possibility in Figure 5-9, where only the frequency shift contrast shows sharp variations.

Dissipative interactions, at the same time, also have significant impact on the tip motion and their effect becomes more prominent when the motion is composed of multiple eigenmodes. For example, in case of the trimodal operation, the overall tip speed is a superposition of three eigenmodes, which is significantly higher than the single-mode or bimodal operations due to very high frequencies involved. Combined

with the large stiffness values of the higher modes, the resulting velocity-dependent losses (as described by equation 5.4) are much higher. Driving the modes at large oscillation amplitudes also results in higher velocities, in turn causing increased dissipation. However, when the amplitudes are increased, the corresponding losses are proportionately smaller as compared to the extra input energy, meaning that a stable operation is still possible. Another effect of dissipation is that it changes the effective quality factor of the cantilever, which changes the slope of the phase curve. For the eigenmode that is being controlled in the PLL mode, the gains of the controller have been tuned for the characteristics of phase curve of the free response. The change in quality factor causes the gains to be not optimized for the adjustments in amplitude and frequency, leading to possible errors in the feedback response.

Furthermore, in addition to directly affecting the tip motion, dissipation also impacts the overall conservative forces experienced by the tip. This coupling of interactions can be attributed to the loss in kinetic energy of the cantilever due to dissipative processes, which decreases the oscillation amplitude, causing reduced penetration of the tip into the conservative tip-sample interaction potential and consequently, reducing their effect on the tip motion and on observed variables.

In addition to the effect of the higher eigenmode amplitudes and surface properties on the contrast, it is also imperative to understand the influence of the fundamental eigenmode amplitude that is controlled in the AM-AFM mode and governs the primary motion of the tip by operating at a setpoint value during imaging. A low oscillation amplitude may favor attractive imaging conditions due to smaller restoring forces and small tip-sample contact time, causing the tip to not penetrate in

the repulsive regions. On the other hand, if it operates at high oscillation amplitude and the setpoint is chosen such that the tapping on sample is very hard (meaning increased repulsive and dissipative forces), it may cause the fundamental eigenmode resonance frequency to shift significantly. Given the fixed excitation frequency AM-AFM operation, the resulting off-resonance operation will have a smaller amplitude that can result in unstable motion and imaging artifacts.

Another interesting set of results was obtained by changing the imaging conditions that caused the inversion of contrast for one of the higher eigenmodes, as shown in Figure 5-10. Here, the phase shifts of first and second modes and negative of third mode frequency shift have been superimposed on the topography of an *orange peel* sample imaged with an AC240 cantilever. Such behavior was also seen in the single-point curves in Figure 5-6 when the imaging parameters were varied. The observed response is different from the previously shown behaviors with both modes exhibiting similar variations or the loss of contrast for one of the modes, and can be explained in the light of various factors that have been discussed in this section. When a soft sample with high dissipation is imaged in the trimodal operation, it is possible that one of the higher eigenmodes has sufficient oscillation energy to overcome the dissipative resistance and operate in the repulsive region, whereas the other higher eigenmode remains in the attractive regime. This will result in the two modes exhibiting opposite contrasts corresponding to the two interaction regimes.

Due to the complex nature of interactions and coupling of the modes, topographical artifacts are also potential outcomes of trimodal operation. As discussed earlier, depending on the oscillation amplitudes of higher eigenmodes and

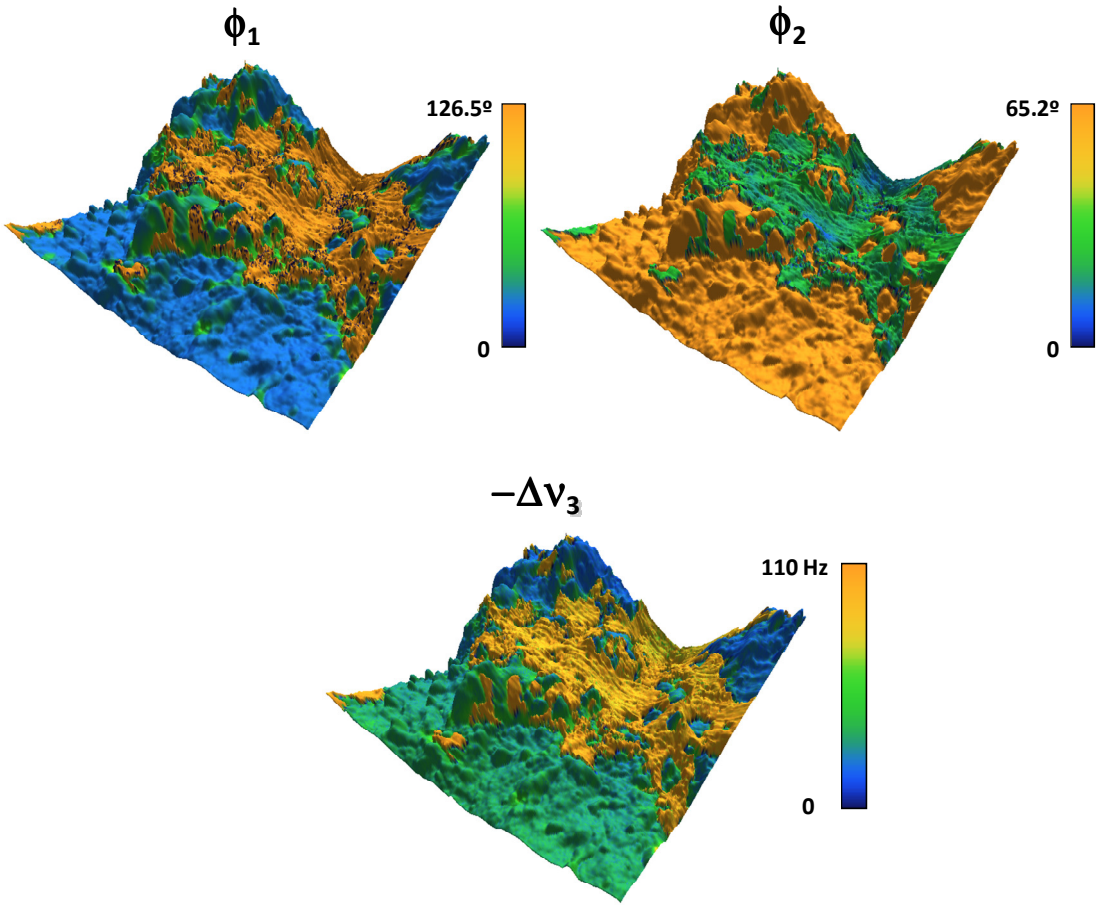

Figure 5-10 *Trimodal AFM images of orange peel sample: (left) fundamental eigenmode phase superimposed on topography, (center) second eigenmode phase superimposed on topography, showing inverted contrast, and (right) third eigenmode frequency shift superimposed on topography (note that the graph shows the negative of the frequency shift). The imaging parameters were* $A_{1\text{-}o}$ *= 100 nm,* $A_{1\text{-}setpoint}$ *= 25 nm,* $A_{2\text{-}o}$ *~ 8.5 nm,* $A_{3\text{-}o}$ *~ 11.5 nm, scan speed = 5µm/s.*

the properties of the sample, the tip penetration into the sample will vary, which will cause each eigenmode to lose different amount of energy and experience different force gradients. As a result, the fundamental eigenmode, which is controlled to operate at a setpoint amplitude, may respond to these changes falsely by interpreting them as the height variations on the surface.

With the deviations from the expected behavior seen in the images as a result of the cumulative effect of various factors, the quantitative interpretation of the results is relatively difficult in the trimodal operation. This requires further understanding of the dependence of the higher eigenmode motion on various surface and operation parameters, along with their operation in various controls methods and the effect of conservative and dissipative interactions. In an effort towards explaining some of these behaviors and determining recommended range of operation parameters, we have performed a detailed computational analysis to study the effects of elastic properties, dissipation and oscillation amplitudes [105]. Also, in section 4.4, a quantitative comparison of various control schemes for higher eigenmodes, and the methods to separate the conservative and dissipative interactions from the response have been presented [99]. In addition to the open-loop and constant-excitation PLL controls for higher eigenmodes that have been used in the trimodal images shown above, a third control scheme, constant-amplitude PLL mode is also possible and has been discussed in section 4.4. In this, the drive amplitude is adjusted to compensate for the loss in tip energy due to dissipation on the surface, and the output channels have been shown to directly map conservative and dissipative variations on the surface.

5.3 Trimodal AFM: summary

In summary, a new multifrequency AFM imaging technique has been presented by excitation of three eigenmodes in order to simultaneously obtain topography, phase and frequency shift contrasts [102]. In addition to the experimental implementation and imaging, influence of various surface and operation parameters on the response has been discussed and explained through computational analysis [105]. Also, efforts have been made towards quantitative understanding of the conservative and dissipative interactions through the control of higher eigenmodes [99, 103]. Overall, the trimodal AFM imaging is a new method and we believe that it is promising, relatively simple to implement and is complementary to existing methods by increasing available channels to characterize the surface composition. As with other new AFM procedures, whose subtleties require extensive investigation in order to be understood, there is room to explore the applications of this method as well.

6. Conclusions

This section will present the intellectual contributions and anticipated benefits to the research community and industry resulting from the advances reported as part of this dissertation.

6.1 Intellectual contributions

This dissertation yields various contributions to the existing metrology techniques at the nanometer scale, and more precisely, to the current AFM capabilities in measuring the tip-sample interaction forces and mapping the surface properties. The four most important and potentially useful contributions are: (1) providing guidelines for multi-scale methodology for real-time simulation of dynamic AFM to numerically illustrate the concepts, (2) computational development of a dual-frequency-excitation atomic force spectroscopy method enabling simultaneous acquisition of topography and tip-sample interaction forces, (3) experimental implementation of a multifrequency AFM imaging technique in air by driving and controlling three cantilever eigenmodes to obtain additional channels for surface characterization, and (4) development of AFM imaging methods with frequency-modulation control of the higher eigenmodes in order to quantitatively map conservative and dissipative tip-sample interactions.

6.1.1 Multi-scale methodology for real-time AFM simulations

As a part of the computational analysis of the dynamic AFM methods discussed, a multi-scale simulation approach combining atomistic and continuum simulations has been applied in its most basic form to study the influence of tip-sample interactions on the oscillating cantilever in single- and multifrequency imaging and force spectroscopy operations. The step-by-step approach to simulating the AFM system in the context of a given physical problem has been explained, along with the appropriate control schemes. This includes the calculation of tip-sample forces using atomistic models in molecular dynamics, developing equations of motion for physical system used and applying the control *rules* corresponding to the imaging operation. This simulation methodology provides useful guidelines to study many problems involving nanoscale samples and is especially useful in the simulation of AFM images of structures containing several thousands of atoms, where the user is not necessarily concerned with the atomic resolution.

6.1.2 Dual-frequency-excitation atomic force spectroscopy method

A novel dynamic atomic force spectroscopy method based on excitation and control of two cantilever eigenmodes has been presented and evaluated through extensive numerical simulations to verify its feasibility in extracting the tip-sample interaction forces and topography for the entire surface with a single surface scan. The method principle relies on measuring the frequency shifts due to the tip-sample interactions with respect to the vertical positions in the range of tip motion, which are

related to force gradients with a first order approximation. It is shown that such measurements can be performed at any horizontal location on the surface while the tip is scanning the surface to map the topography, allowing representation of the tip-sample forces as a function of the *x, y* and *z* coordinates in the 3-dimensional volume above the sample.

The computational results have been presented for a wide range of operation parameters and for possible sensor designs in order to demonstrate the feasibility of the method and to provide guidelines for experimental implementation. Furthermore, the advantages of the method have been discussed and can be summarized as, (1) collection of quantitative information about mechanical properties of the sample is rapid as compared to the most existing spectroscopy methods, (2) the information about the force curves is useful in mitigating the imaging artifacts by monitoring the level of tip penetration into the sample in real time, and (3) in addition to recording the conservative force curves, such measurement capability has applications in measuring the dissipative surface effects.

6.1.3 Trimodal AFM imaging method

A trimodal imaging scheme for ambient air operation has been developed with the excitation and control of three eigenmodes of a cantilever with which it is possible to simultaneously acquire topographical, phase and frequency shift contrast images. Due to the dependence of these variables on the material properties, quantitative information about the surface can be obtained using the extra characterization channels. Computational and experimental results have been presented to illustrate

the concept and dependence of operation on the imaging and surface parameters, such as oscillation amplitudes of eigenmodes, conservative and dissipative tip-sample interactions. Furthermore, a detailed description of the experimental system that was built for this implementation has been included for reference. In addition to driving three eigenmodes, another novel aspect of this method is frequency-modulated control of a higher eigenmode for ambient air operation. The method is step forward in multifrequency AFM applications, is relatively easy to implement, and can prove very useful in studying surface composition.

6.1.4 Measurement of conservative and dissipative tip-sample interactions

Applications of bimodal AFM operation in the separation of conservative and dissipative contributions of the tip-sample interactions have been presented. Within this, three possible control methods to operate the higher eigenmode have been studied for their respective usefulness in performing such measurements. This also includes comparison of newly incorporated frequency-modulation control of higher eigenmode for multifrequency intermittent-contact operation in ambient air with the commonly used open-loop control in such imaging operations. The quantitative comparison has been performed through spectroscopy and imaging measurements on samples with varying properties in each control mode and by analyzing the data in terms of conservative and dissipative interaction components. This is first such study for the imaging operation in air and provides guidelines for the future use of these excitation approaches.

6.2 Anticipated benefits

The development of new multifrequency AFM nanomechanical characterization techniques with capabilities beyond the state of the art is a significant step forward, especially for a method that has been available since the 1980s. Dual-frequency AFM spectroscopy, both as imaging and as nanomechanical characterization technique, is especially relevant for the numerous soft biological samples which cannot yet be characterized with AFM, and is a direct contribution to all scientific fields in which such samples are important. If one considers the diversity of biological systems, it is not hard to imagine that the number and type of samples that are still beyond the capabilities of AFM is greater than the number and type of samples that have already been characterized with it. Similarly, the trimodal imaging technique, with its capabilities to map the contrast arising from various surface effects, can be extremely useful in separating the sources of variation in the surface composition without prior knowledge of it. These techniques will also be of great help in the standardization of nanomechanical metrology and in gathering benchmark data. As nanotechnology continues to advance, standardization becomes more and more significant, especially within large-scale initiatives that combine multiple scientific fields, where exchange of information is required.

Besides the fundamental scientific aspects, this dissertation provides guidelines for developments in multi-scale simulation methods, primarily concerning the prediction of *macroscopic* properties that are dependent on fundamental *nanoscale* properties and the simulation of molecular machinery systems. AFM is thought by many to be a precursor of nanomanipulation and nanomanufacturing devices, so,

experimentally validated simulation methodologies that reproduce AFM behavior in a variety of environments will also be instrumental in modeling the behavior and assessing the feasibility of nanomanufacturing systems.

6.3 Future directions

This dissertation has focused on the developments of new imaging and force measurement methods in AFM using the multifrequency excitation approach. The potential applications and benefits of these techniques have been shown. The reported advances have opened several new research directions, some of which are discussed in this section.

6.3.1 Development of a high-speed measurement system

In this dissertation, the computational development of dual-frequency force spectroscopy method has been reported, along with the required steps and challenges in its experimental commissioning. One of the basic requirements of the implementation is the frequency-modulated control of the higher eigenmode, which has been successfully demonstrated. However, successful force curve acquisition experimentally was restricted by the lack of instrumentation that can record with high precision the changes in the frequencies of the oscillations at very high frequencies. Such precise frequency measurements are necessary in order to obtain an accurate representation of the tip-sample force curves. In the light of these requirements, it becomes necessary to either achieve this goal through innovations in the

instrumentation or by developing a methodology that can extract accurate information by collecting and averaging over the data for many response cycles.

6.3.2 Exploring applications of very high speed AFM sensors for dual-frequency force spectroscopy method

Another possible approach for the experimental realization of the dual-frequency force spectroscopy method could be the use of AFM sensors with frequencies in the range of gigahertz [98]. Use of such a sensor will provide frequency ratios between the high- and the low-frequency oscillations of the desired dual-frequency motion in the order of a few thousands. This can in turn allow tracking the changes in the frequency with routinely used measurement systems that operate on the principle of averaging the data over a number of oscillations for calculations. The standard AFM systems, however, are not equipped with sufficiently fast actuation and detection systems, and electronics that can process frequencies of this order. Therefore, advanced AFM setups with fast actuation, sensing and signal processing capabilities could be used to explore this approach.

6.3.3 Development of trimodal AFM imaging applications for quantitative measurement of surface properties

The applications of multifrequency AFM imaging have been discussed in the mapping of conservative and dissipative variations on the surface. The dissipative interactions arise as a result of various surface phenomena, such as viscoelasticity, adhesion, capillary forces, etc. However, relationship between the acquired

quantitative information and these individual effects is still not well understood and is a significant challenge. The advantage of trimodal imaging is that it provides multiple channels that contain information on the influence of all these surface processes. With an improved understanding of the coupled trimodal operation and potential development of analytical relationships amongst the various channels or explaining the dependence of various channels on specific processes could be useful to separate out the surface effects in terms of physical variables.

References

[1] Binnig, G., Quate, C. F., and Gerber, C., 1986, "Atomic Force Microscope," Physical Review Letters, **56**, pp. 930-933.

[2] Garcia, R., and Perez, R., 2002, "Dynamic atomic force microscopy methods," Surface Science Reports, **47**, pp. 197-301.

[3] Albrecht, T. R., Grutter, P., Horne, D., and Rugar, D., 1991, "Frequency-modulation detection using high-Q cantilevers for enhanced force microscope sensitivity," Journal of Applied Physics, **69**, pp. 668-673.

[4] Rodriguez, T., and Garcia, R., 2004, "Compositional mapping of surfaces in atomic force microscopy by excitation of the second normal mode of the microcantilever," Applied Physics Letters, **84**, pp. 449-451.

[5] Seo, Y., and Jhe, W., 2008, "Atomic force microscopy and spectroscopy," Reports on Progress in Physics, **71**, No. 016101.

[6] Bachmann, D., and Hierold, C., 2007, "Determination of pull-off forces of textured silicon surfaces by AFM force curve analysis," Journal of Micromechanics & Microengineering, **17**, pp. 1326-1333.

[7] Cross, S. E., Jin, Y. S., Rao, J. Y., and Gimzewski, J. K., 2007, "Nanomechanical analysis of cells from cancer patients," Nature Nanotechnology, **2**, pp. 780-783.

[8] Lu, M. Z., Gao, S., Qihai, J., Cui, J. J., Du, H., and Gao, H. T., 2007, "An atomic force microscope head designed for nanometrology," Measurement Science & Technology, **18**, pp. 1735-1739.

[9] Giessibl, F. J., 2001, "A direct method to calculate tip-sample forces from frequency shifts in frequency-modulation atomic force microscopy," Applied Physics Letters, **78**, pp. 123-125.

[10] Gotsmann, B., Anczykowski, B., Seidel, C., and Fuchs, H., 1999, "Determination of tip-sample interaction forces from measured dynamic force spectroscopy curves," Applied Surface Science, **140**, pp. 314-319.

[11] Gotsmann, B., Seidel, C., Anczykowski, B., and Fuchs, H., 1999, "Conservative and dissipative tip-sample interaction forces probed with dynamic AFM," Physical Review B, **60**, pp. 11051-11061.

[12] Hölscher, H., Allers, W., Schwarz, U. D., Schwarz, A., and Wiesendanger, R., 1999, "Determination of tip-sample interaction potentials by dynamic force spectroscopy," Physical Review Letters, **83**, pp. 4780-4783.

[13] Jarvis, S. P., Yamada, H., Yamamoto, S. I., Tokumoto, H., and Pethica, J. B., 1996, "Direct mechanical measurement of interatomic potentials," Nature, **384**, pp. 247-249.

[14] Sahin, O., Magonov, S., Su, C., Quate, C., and Solgaard, O., 2007, "An atomic force microscope tip designed to measure time-varying nanomechanical forces," Nature Nanotechnology, **2**, pp. 507-514.

[15] Cleveland, J., Anczykowski, B., Schmid, A., and Elings, V., 1998, "Energy dissipation in tapping-mode atomic force microscopy," Applied Physics Letters, 72, pp. 2613-2615.

[16] Garcia, R., Tamayo, J., and San Paulo, A., 1999, "Phase contrast and surface energy hysteresis in tapping mode scanning force microsopy," Surface and Interface Analysis, **27**, pp. 312-316.

[17] Proksch, R., and Kalinin, S., 2010, "Energy dissipation measurements in frequency-modulated scanning probe microscopy," Nanotechnology, **21**, No. 455705.

[18] Martinez, N. F., and Garcia, R., 2006, "Measuring phase shifts and energy dissipation with amplitude modulation atomic force microscopy," Nanotechnology, **17**, pp. S167-S172.

[19] Garcia, R., Gomez, C. J., Martinez, N. F., Patil, S., Dietz, C., and Magerle, R., 2006, "Identification of nanoscale dissipation processes by dynamic atomic force microscopy," Physical Review Letters, **97**, No. 016103.

[20] Gomez, C. J., and Garcia, R., 2010, "Determination and simulation of nanoscale energy dissipation processes in amplitude modulation AFM," Ultramicroscopy, **110**, pp. 626-633.

[21] Sasaki, N., and Tsukada, M., 2000, "Effect of microscopic nonconservative process on noncontact atomic force microscopy," Japanese Journal of Applied Physics, **39**, pp. L1334-L1337.

[22] Kantorovich, L. N., and Trevethan, T., 2004, "General theory of microscopic dynamical response in surface probe microscopy: From imaging to dissipation," Physical Review Letters, **93**, No. 236102.

[23] Tamayo, J., and Garcia, R., 1997, "Effects of elastic and inelastic interactions on phase contrast images in tapping-mode scanning force microscopy," Applied Physics Letters, **71**, pp. 2394-2396.

[24] Hölscher, H., Gotsmann, B., Allers, W., Schwarz, U. D., Fuchs, H., and Wiesendanger, R., 2001, "Measurement of conservative and dissipative tip-sample interaction forces with a dynamic force microscope using the frequency modulation technique," Physical Review B, **64**, No. 075402.

[25] Schirmeisen, A., Hölscher, H., Anczykowski, B., Weiner, D., Schafer, M. M., and Fuchs, H., 2005, "Dynamic force spectroscopy using the constant-excitation and constant-amplitude modes," Nanotechnology, **16**, pp. S13-S17.

[26] Hölscher, H., Gotsmann, B., and Schirmeisen, A., 2003, "Dynamic force spectroscopy using the frequency modulation technique with constant excitation," Physical Review B, **68**, No. 153401.

[27] Martinez, N. F., Patil, S., Lozano, J. R., and Garcia, R., 2006, "Enhanced compositional sensitivity in atomic force microscopy by the excitation of the first two flexural modes," Applied Physics Letters, **89**, No. 153115.

[28] Proksch, R., 2006, "Multifrequency, repulsive-mode amplitude-modulated atomic force microscopy," Applied Physics Letters, **89**, No. 113121.

[29] Martinez, N., Lozano, J., Herruzo, E., Garcia, F., Richter, C., Sulzbach, T., and Garcia, R., 2008, "Bimodal atomic force microscopy imaging of isolated antibodies in air and liquids," Nanotechnology, **19**, No. 384011.

[30] Naitoh, Y., Ma, Z. M., Li, Y. J., Kageshima, M., and Sugawara, Y., 2010, "Simultaneous observation of surface topography and elasticity at atomic

scale by multifrequency frequency modulation atomic force microscopy," Journal of Vacuum Science & Technology B, **28**, pp. 1210-1214.

[31] Kawai, S., Glatzel, T., Koch, S., Such, B., Baratoff, A., and Meyer, E., 2009, "Systematic Achievement of Improved Atomic-Scale Contrast via Bimodal Dynamic Force Microscopy," Physical Review Letters, **103**, No. 220801.

[32] Binnig, G., and Rohrer, H., 2000, "Scanning tunneling microscopy (Reprinted from IBM Journal of Research and development, vol 30, 1986)," Ibm Journal of Research and Development, **44**, pp. 279-293.

[33] Binnig, G., Rohrer, H., Gerber, C., and Weibel, E., 1983, "7X7 reconstruction on Si(111) resolved in real space," Physical Review Letters, **50**, pp. 120-123.

[34] Ohnesorge, F., and Binnig, G., 1993, "True atomic resolution by atomic force microscopy through repulsive and attractive forces," Science, **260**, pp. 1451-1456.

[35] Schimmel, T., Koch, T., Kuppers, J., and Lux-Steiner, M., 1999, "True atomic resolution under ambient conditions obtained by atomic force microscopy in the contact mode," Applied Physics a-Materials Science & Processing, **68**, pp. 399-402.

[36] Anselmetti, D., Luthi, R., Meyer, E., Richmond, T., Dreier, M., Frommer, J. E., and Guntherodt, H. J., 1994, "Attractive-mode imaging of biological materials with dynamic force microscopy," Nanotechnology, **5**, pp. 87-94.

[37] Bustamante, C., and Keller, D., 1995, "Scanning force microscopy in biology," Physics Today, **48**, pp. 32-38.

[38] Moller, C., Allen, M., Elings, V., Engel, A., and Muller, D. J., 1999, "Tapping-mode atomic force microscopy produces faithful high-resolution images of protein surfaces," Biophysical Journal, **77**, pp. 1150-1158.

[39] San Paulo, A., and Garcia, R., 2000, "High-resolution imaging of antibodies by tapping-mode atomic force microscopy: Attractive and repulsive tip-sample interaction regimes," Biophysical Journal, **78**, pp. 1599-1605.

[40] Giessibl, F. J., 1995, "Atomic-resolution of the silicon (111)-(7X7) surface by atomic force microscopy," Science, **267**, pp. 68-71.

[41] Sugawara, Y., Ohta, M., Ueyama, H., and Morita, S., 1995, "Defect motion on an InP(110) surface observed with noncontact atomic force microscopy," Science, **270**, pp. 1646-1648.

[42] Kitamura, S., and Iwatsuki, M., 1995, "Observation of 7X7 reconstructed structure on the silicon (111) surface using ultrahigh-vacuum noncontact atomic force microscopy," Japanese Journal of Applied Physics Part 2-Letters, **34**, pp. L145-L148.

[43] Paulo, A. S., and Garcia, R., 2002, "Unifying theory of tapping-mode atomic-force microscopy," Physical Review B, **66**, No. 041406.

[44] Anczykowski, B., Kruger, D., Babcock, K. L., and Fuchs, H., 1996, "Basic properties of dynamic force spectroscopy with the scanning force microscope in experiment and simulation," Ultramicroscopy, **66**, pp. 251-259.

[45] Gotsmann, B., and Fuchs, H., 2002, "Dynamic AFM using the FM technique with constant excitation amplitude," Applied Surface Science, **188**, pp. 355-362.

[46] Solares, S. D., 2007, "Frequency and force modulation atomic force microscopy: low-impact tapping-mode imaging without bistability," Measurement Science & Technology, **18**, pp. L9-L14.

[47] Solares, S. D., and Crone, J. C., 2007, "Real-time simulation of isolated biomolecule characterization with frequency and force modulation atomic force microscopy," The Journal of Physical Chemistry C, **111**, pp. 10029-10034; 10029.

[48] Solares, S. D., 2007, "Eliminating bistability and reducing sample damage through frequency and amplitude modulation in tapping-mode atomic force microscopy," Measurement Science & Technology, **18**, pp. 592-600.

[49] Kalinin, S. V., Gruveman, A., 2011, "Scanning probe microscopy of functional materials," Springer, ISBN 978-1-4419-6567-7.

[50] Nony, L., and Baratoff, A., 2006, "Noncontact atomic force microscopy simulator with phase-locked-loop controlled frequency detection and excitation," Physical Review B, **74**, No. 235439.

[51] Giessibl, F. J., and Bielefeldt, H., 2000, "Physical interpretation of frequency-modulation atomic force microscopy," Physical Review B, **61**, pp. 9968-9971.

[52] Ternes, M., Lutz, C. P., Hirjibehedin, C. F., Giessibl, F. J., and Heinrich, A. J., 2008, "The force needed to move an atom on a surface," Science, **319**, pp. 1066-1069.

[53] Stark, R. W., and Heckl, W. M., 2003, "Higher harmonics imaging in tapping-mode atomic-force microscopy," Review of Scientific Instruments, **74**, pp. 5111-5114.

[54] Stark, M., Stark, R. W., Heckl, W. M., and Guckenberger, R., 2000, "Spectroscopy of the anharmonic cantilever oscillations in tapping-mode atomic-force microscopy," Applied Physics Letters, **77**, pp. 3293-3295.

[55] Sahin, O., Yaralioglu, G., Grow, R., Zappe, S. F., Atalar, A., Quate, C., and Solgaard, O., 2004, "High-resolution imaging of elastic properties using harmonic cantilevers," Sensors and Actuators a-Physical, **114**, pp. 183-190.

[56] Sahin, O., Quate, C. F., Solgaard, O., and Atalar, A., 2004, "Resonant harmonic response in tapping-mode atomic force microscopy," Physical Review B, **69**.

[57] Balantekin, M., and Atalar, A., 2005, "Enhanced higher-harmonic imaging in tapping-mode atomic force microscopy," Applied Physics Letters, **87**, No. 243513.

[58] Balantekin, M., and Atalar, A., 2005, "Enhancing higher harmonics of a tapping cantilever by excitation at a submultiple of its resonance frequency," Physical Review B, **71**, No. 125416.

[59] Crittenden, S., Raman, A., and Reifenberger, R., 2005, "Probing attractive forces at the nanoscale using higher-harmonic dynamic force microscopy," Physical Review B, **72**, No. 235422.

[60] Rodriguez, B., Callahan, C., Kalinin, S. V., and Proksch, R., 2007, "Dual-frequency resonance-tracking atomic force microscopy," Nanotechnology, **18**, No. 475504.

[61] Platz, D., Tholen, E., Pesen, D., and Haviland, D., 2008, "Intermodulation atomic force microscopy," Applied Physics Letters, **92**, No. 153106.

[62] Jesse, S., Kalinin, S., Proksch, R., Baddorf, A., and Rodriguez, B., 2007, "The band excitation method in scanning probe microscopy for rapid mapping of energy dissipation on the nanoscale," Nanotechnology, **18**, No. 435503.

[63] Thota, P., MacLaren, S., and Dankowicz, H., 2007, "Controlling bistability in tapping-mode atomic force microscopy using dual-frequency excitation," Applied Physics Letters, **91**, No. 093108.

[64] Dick, A. J., and Solares, S. D., 2011, "Utilizing Off-Resonance and Dual-Frequency Excitation to Distinguish Attractive and Repulsive Surface Forces in Atomic Force Microscopy," Journal of Computational and Nonlinear Dynamics, **6**, No. 031005.

[65] Li, Y. J., Takahashi, K., Kobayashi, N., Naitoh, Y., Kageshima, M., and Sugawara, Y., 2010, "Multifrequency high-speed phase-modulation atomic force microscopy in liquids," Ultramicroscopy, **110**, pp. 582-585.

[66] Lee, M. H., and Jhe, W. H., 2006, "General theory of amplitude-modulation atomic force microscopy," Physical Review Letters, **97**, No. 036104.

[67] Ke, S. H., Uda, T., and Terakura, K., 1999, "Quantity measured in frequency-shift-mode atomic-force microscopy: an analysis with a numerical model," Physical Review B, **59**, pp. 13267-13272.

[68] Stich, I., Tobik, J., Perez, R., Terakura, K., and Ke, S. H., 2000, "Tip-surface interactions in noncontact atomic force microscopy on reactive surfaces," Progress in Surface Science, **64**, pp. 179-191.

[69] Giessibl, F. J., 2003, "Advances in atomic force microscopy," Review of Modern Physics, **75**, pp. 949-983.

[70] Durig, U., 1999, "Relations between interaction force and frequency shift in large-amplitude dynamic force microscopy," Applied Physics Letters, **75**, pp. 433-435.

[71] Giessibl, F. J., 1997, "Forces and frequency shifts in atomic-resolution dynamic-force microscopy," Physical Review B, **56**, pp. 16010-16015.

[72] Albers, B. J., Liebmann, M., Schwendemann, T. C., Baykara, M. Z., Heyde, M., Salmeron, M., Altman, E. I., and Schwarz, U. D., 2008, "Combined low-temperature scanning tunneling/atomic force microscope for atomic resolution imaging and site-specific force spectroscopy," Review of Scientific Instruments, **79**, No. 033704.

[73] Hölscher, H., Langkat, S. M., Schwarz, A., and Wiesendanger, R., 2002, "Measurement of three-dimensional force fields with atomic resolution using dynamic force spectroscopy," Applied Physics Letters, **81**, pp. 4428-4430.

[74] Stark, M., Stark, R., Heckl, W., and Guckenberger, R., 2002, "Inverting dynamic force microscopy: From signals to time-resolved interaction forces," Proceedings of the National Academy of Sciences of the United States of America, pp. 8473-8478.

[75] Martin, P., Marsaudon, S., Aime, J., and Bennetau, B., 2005, "Experimental determination of conservative and dissipative parts in the tapping mode on a grafted layer: comparison with frequency modulation data," Nanotechnology, **16**, pp. 901-907.

[76] Sader, J., and Jarvis, S., 2006, "Coupling of conservative and dissipative forces in frequency-modulation atomic force microscopy," Physical Review B, **74**, No. 195424.

[77] Lozano, J., and Garcia, R., 2009, "Theory of phase spectroscopy in bimodal atomic force microscopy," Physical Review B, **79**, No. 014110.

[78] Lozano, J. R., and Garcia, R., 2008, "Theory of multifrequency atomic force microscopy," Physical Review Letters, **100**, No. 076102.

[79] Chawla, G., and Solares S. D., 2009, "Computational Development of Single- and Dual-Frequency Modulation Atomic Force Spectroscopy for Ambient Air Applications," ASME Conference Proceedings, pp. 707-716.

[80] Checco, A., Gang, O., and Ocko, B. M., 2006, "Liquid nanostripes," Physical Review Letters, **96**, No. 056104.

[81] Chawla, G., and Solares, S. D., 2009, "Single-cantilever dual-frequency-modulation atomic force microscopy," Measurement Science & Technology, **20**, No. 015501.

[82] Solares, S. D., and Chawla, G., 2008, "Dual frequency modulation with two cantilevers in series: a possible means to rapidly acquire tip-sample interaction force curves with dynamic AFM," Measurement Science & Technology, **19**, No. 055502.

[83] Solares, S., and Chawla, G., 2010, "Exploration of AFM Imaging Artifacts Occurring at Sharp Surface Features When Using Short Carbon Nanotube Probes and Possible Mitigation With Real-Time Force Spectroscopy," Journal

of Manufacturing Science and Engineering-Transactions of the Asme, **132**, No. 030904.

[84] Solares, S., and Hölscher, H., 2010, "Numerical analysis of dynamic force spectroscopy using a dual-oscillator sensor," Journal of Vacuum Science & Technology B, **28**, No. C4E1.

[85] Solares, S., and Hölscher, H., 2010, "Numerical analysis of dynamic force spectroscopy using the torsional harmonic cantilever, Nanotechnology, **21**, No. 075702.

[86] Garcia, R., and San Paulo, A., 1999, "Attractive and repulsive tip-sample interaction regimes in tapping-mode atomic force microscopy," Physical Review B, **60**, pp. 4961-4967.

[87] Lee, S. I., Howell, S. W., Raman, A., and Reifenberger, R., 2002, "Nonlinear dynamics of microcantilevers in tapping mode atomic force microscopy: A comparison between theory and experiment," Physical Review B, **66**, No. 115409.

[88] Rutzel, S., Lee, S. I., and Raman, A., 2003, "Nonlinear dynamics of atomic-force-microscope probes driven in Lennard-Jones potentials," Proceedings of the Royal Society A, **459**, pp. 1925-1948.

[89] S. D. Solares, M. J. Esplandiu, W. A. Goddard, and C. P. Collier, 2005, “Mechanisms of single-walled carbon nanotube probe-sample multistability in tapping-mode AFM imaging,” Journal of Physical Chemistry B, **109**, pp. 11493-11500.

[90] S. D. Solares, 2008, “Characterization of deep nanoscale surface trenches with AFM using thin carbon nanotube probes in amplitude-modulation and frequency-force-modulation modes,” Measurement Science and Technology **19**, No. 015503.

[91] R. W. Stark, 2004, “Optical lever detection in higher eigenmode dynamic atomic force microscopy,” Review of Scientific Instruments, **75**, pp. 5053-5055.

[92] K. Yagasaki, 2004, “Nonlinear dynamics of vibrating microcantilevers in tapping-mode atomic force microscopy,” Physical Review B, **70**, No. 245419.

[93] "Asylum Research” (www.asylumresearch.com), 6310 Hollister Ave., Santa Barbara, CA 93117 USA.

[94] "RHK Technologies” (www.rhk-tech.com), 1050 East Maple Road, Troy, MI 48083 USA.

[95] "Krohn-Hite Corporation” (www.krohn-hite.com), 15 Jonathan Drive, Unit 4, Brockton, MA 02301 USA.

[96] "Agilent Technologies” (www.agilent.com), 5301 Stevens Creek Blvd, Santa Clara CA 95051 USA.

[97] "http://www.nanoworld.com/pointprobe-zeiss-veritekt-reflex-coated-afm-tip-zeilr."

[98] Morita, S., Giessibl, F. J., and Wiesendanger, R., 2002, "Noncontact Atomic Force Microscopy," Springer, ISBN 978-3-540-43117-6.

[99] Chawla, G., and Solares, S. D., 2011, "Mapping of conservative and dissipative interactions in bimodal atomic force microscopy using open-loop and phase-locked-loop control of the higher eigenmode," *Submitted*.

[100] "http://www.brukerafmprobes.com/p-3725-ps-ldpe-gs.aspx."

[101] "http://www.asylumresearch.com/Probe/AC240TS,Olympus."

[102] Solares, S., and Chawla, G., 2010, "Triple-frequency intermittent contact atomic force microscopy characterization: Simultaneous topographical, phase, and frequency shift contrast in ambient air," Journal of Applied Physics, **108**, No. 054901.

[103] Chawla, G., and Solares, S. D., 2011, "Trimodal tapping-mode atomic force microscopy: a possible method for simultaneous measurement of conservative and dissipative interactions," ASME Conference Proceedings, *Accepted*.

[104] Derjaguin, B., Muller, V., and Toporov, Y., 1975, "Effect of contact deformations on adhesion of particles," Journal of Colloid and Interface Science, **53**, pp. 314-326.

[105] Solares, S., and Chawla, G., 2010, "Frequency response of higher cantilever eigenmodes in bimodal and trimodal tapping mode atomic force microscopy," Measurement Science & Technology, **21**, No. 125502.